Supplementary Information

Enhanced electronic coupling in tetraaryl molecular junctions with osmium(IV) centers

Luana Zagami,[a] Mukund Sharma,[a] Andrew Fraire,[a] Cynthia Avedian,[a] Clarissa Olivar,[a] Thomas M. Czyszczon-Burton,[a] Jazmine Prana,[a] Sandugash Yergeshbayeva,[a] María Camarasa-Gómez,[b] Daniel Hernangómez-Pérez,[c,*] and Michael S. Inkpen[a,*]

[a] *Department of Chemistry, University of Southern California, Los Angeles, CA 90089, USA*

[b] *Centro de Física de Materiales (CFM-MPC) CSIC-UPV/EHU, 20018 Donostia-San Sebastián, Spain*

[c] *CIC nanoGUNE BRTA, Tolosa Hiribidea, 76, 20018 Donostia-San Sebastián, Spain*

E-mail: d.hernangomez@nanogune.eu, inkpen@usc.edu

Contents

1. General Information

Synthetic Methods

Manipulations under a nitrogen atmosphere were carried out in oven-dried glassware using standard Schlenk line techniques. No special precautions were taken to exclude air or moisture during workup unless otherwise stated. Tetrahydrofuran (THF) was sparged with nitrogen and dried using a two-column solvent purification system packed with alumina (Pure Process Technologies, Nashua, NH, USA). N,N-Dimethylformamide (DMF) was purified by vacuum distillation, dried over 3Å molecular sieves,[1] and stored under nitrogen. Molecular sieves were activated by heating for ≥3.5 h at 350°C in a muffle furnace (Thermolyne, Thermo Scientific, Asheville, NC, USA), and stored in a desiccator until use. Grignard reagents were commercially available, or prepared according to the general method described in previous literature,[2] and titrated using a salicylaldehyde phenylhydrazone indicator to determine their concentration prior to use.[3] $(Oct_4N)_2[OsBr_6]$,[2] tetrakis(4-bromo-2,5-dimethylphenyl)osmium(IV),[4] tetrakis(2,5-dimethyl-4-(methylthio)phenyl)osmium(IV) (**Os1**),[5] tetrakis(4-bromophenyl)silane,[6] (4'-(methylthio)-[1,1'-biphenyl]-4-yl)(triphenylphosphine)gold(I) (**Au2**),[7] **P4SMe**[8,9] and **MTh**[10] were prepared using established literature procedures. Other reaction solvents (sparged with nitrogen prior to use) and chemical reagents were commercially available and used without further purification. 18.2 MΩ water was generated using an Arium® Mini Plus UV ultrapure water system (Sartorius AG, Goettingen, Germany). Deuterated solvents were purchased from Cambridge Isotope Laboratories, Inc., Cambridge Isotope Laboratories, Tewksbury, MA USA. Flash chromatography was performed using a Pure C-850 FlashPrep chromatography system and FlashPure EcoFlex flash cartridges (silica, irregular 50-75 μm particle size, 50-70 Å pore size; BUCHI Corporation, New Castle, DE, USA). Reaction yields are unoptimized.

^{1}H and $^{13}C\{^{1}H\}$ NMR spectra were recorded at room temperature on Varian VNMRS 600 (600 MHz), VNMRS 500 (500 MHz), VNMRS 400 (400 MHz), or Mercury 400 (400 MHz) NMR spectrometers. ^{1}H NMR data recorded in $CDCl_3$ and CD_2Cl_2 is referenced to residual internal $C\mathit{H}Cl_3$ (δ 7.26) and $C\mathit{H}_2Cl_2$ (δ 5.32) solvent signals.[11] $^{13}C\{^{1}H\}$ NMR data recorded in $CDCl_3$ and CD_2Cl_2 is referenced to internal $\mathit{C}DCl_3$ (δ 77.16) and $\mathit{C}D_2Cl_2$ (δ 53.52).[11] ^{1}H and $^{13}C\{^{1}H\}$ resonances were assigned where possible for new compounds using 2D correlation spectroscopy experiments. UV-vis spectra were obtained with 0.1 mM solutions in a 10 mm/1 mm pathlength quartz cell (Starna Cells, Starna Cells, Inc., Atascadero, CA, USA), using a Cary 60 UV-vis Spectrophotometer (Agilent Technologies, Inc., Santa Clara, CA, USA) or an AvaSpec-ULS2048-EVO UV/vis Spectrometer integrated with an AvaLight UV/vis/NIR Light Source (Pine Research Instrumentation, Durham, NC, USA; Avantes North America, Lafayette, CO, USA). Mass spectrometry analyses were performed on a Waters GCT Premier (EI), JEOL Accu-TOF JMS-T2000GC (EI), Waters Synapt G2-Si (ESI), Bruker Autoflex Speed LRF (MALDI), or Bruker Daltonics UltrafleXtreme (MALDI) at the Mass Spectrometry Lab, University of Illinois Urbana-Champaign.

X-Ray Crystallography

Single-crystal X-ray diffraction measurements were performed on a Rigaku-Oxford Diffraction XtaLAB Synergy-S Diffractometer with PhotonJet-S microfocus sealed Cu ($\lambda = 1.54184$ Å) X-ray source and HyPix-6000HE hybrid photon counting detector. A colorless block single crystal (0.06×0.38×0.12 mm) was suspended in Parabar oil (Hampton Research) and mounted on a cryoloop, which was placed directly into the cold nitrogen stream (OXFORD Cryosystems 800) to flash-cool the sample to 100.0(1) K. The dataset was recorded at ω-scans at 0.5° step width, using the CrysAlis[12] software package for data collection and reduction. Numerical absorption correction was derived from Gaussian integration over a multifaceted crystal model. An empirical absorption correction was applied based on spherical harmonics as implemented in SCALE3 ABSPACK scaling algorithm.[13] Crystal structure solution and refinement were carried out with SHELX[14,15] using the interface provided by Olex2.[16] Thermal parameters were refined anisotropically for all non-hydrogen atoms to convergence. All H atoms were placed on their calculated positions and their coordinates were refined using a riding model. Full details of crystal structure refinement and the final structural parameters were deposited with the Cambridge Crystallographic Data Center (CCDC). A summary of data collection and refinement is provided in **Table S1**.

Scanning Tunneling Microscope-based Break Junction (STM-BJ)

These details are reproduced here from a previous report, with only minor changes, for convenience.[17] STM–BJ measurements were performed using custom-built setups that have been described previously,[18–20] operated in ambient atmosphere at room temperature. Hardware was controlled and analyses were performed using custom software (written using IgorPro, Wavemetrics Inc., OR, USA). Tip–substrate distances were controlled with sub-angstrom precision using a single-axis preloaded piezoelectric actuator (P-840.1, Physik Instrumente, MA, USA). Tunneling currents were measured using a DLPCA-200 variable gain low noise transimpedance current amplifier (FEMTO Messtechnik GmbH, Berlin, Germany). Applying a bias between the tip and substrate, we calculated the conductance as a function of tip–substrate displacement (at 40 kHz acquisition rate) – from independently measured voltage-displacement and current-displacement traces – as the tip was repeatedly pushed into the substrate to reach a conductance of >5 G_0 (where $G_0 = 2e^2/h$) and then retracted 5–10 nm (at 20 nm/s) to break the contact. Our circuit includes a series resistor of 100 kΩ or 1 MΩ that enables current measurements when in tip-substrate contact.

Conductance-distance traces were compiled into 1D conductance histograms (using 100 bins/decade along the conductance axis), or 2D conductance-distance histograms (using 100 bins/decade along the conductance axis and 1000 bins/nm along the displacement axis). Traces in 2D histograms were aligned such that displacement = 0 nm where $G = 0.5\ G_0$. Color scales inset in 2D histograms are in count/1000 traces. Most probable conductance values for molecular junctions studied here were obtained through Gaussian fits to their corresponding conductance peaks in 1D histograms. All histograms were constructed from ≥5,000 traces, unless otherwise stated. Conductance histograms are presented over conductance ranges chosen either to display all observed conductance features or, where appropriate, to highlight the features under discussion.

STM tips were prepared from freshly cut Au wire (Ø = 0.25 mm; 99.998%, Alfa Aesar, MA, USA or 99.999%, Beantown Chemical, NH, USA). Substrates were prepared from evaporation of 100-200 nm Au (99.9985%, Alfa Aesar, or 99.999%, Angstrom Engineering Inc., ON, Canada) at a rate of ~1 Å/s onto mechanically polished AFM/STM steel specimen discs (Ted Pella Inc., CA, USA) with a COVAP Physical Vapor Deposition System (Angstrom Engineering Inc.) used exclusively for metal evaporation. Gold substrates were UV-ozone cleaned (Probe and Surface Decontamination Standard System, Novascan Technologies, Inc., IA, USA) and used for measurements that same day. Directly before starting a solution measurement, ≥1,000 conductance-displacement traces were collected to check the electrode surfaces were free from contamination. Analytes were typically studied as solutions (0.1-1 mM) in 1,2,4-trichlorobenzene (TCB; Millipore-Sigma, ≥99%), tetradecane (TD; Millipore-Sigma, >99%), or propylene carbonate (PC; Millipore-Sigma, anhydrous, ≥99.7%).

STM-BJ measurements in PC utilized a tip coated in Apiezon wax to minimize background capacitive and Faradaic currents. Voltammetry experiments using a coated gold STM tip as working electrode and gold substrate as counter and reference electrode were performed using a EmStat3+ potentiostat (PalmSens BV, Houten, The Netherlands).

Push-pull measurements were performed by measuring conductance-time traces using a non-linear piezo ramp. In these experiments, the junction was first extended by 2 nm from a displacement in which the conductance exceeded 5 G_0 to form the molecular junction (all movements at 20 nm/s). This was followed by a 0.1 s hold period, after which the tip was displaced towards the substrate by 0.6 nm (push), held for 0.1 s, retracted by 0.6 nm (pull), and held for a further 0.1 s prior to retracting the tip by 6 nm to ensure junction rupture (piezo displacement ramp shown in **Figure 12a**). Individual traces were subsequently analyzed to identify those in which the single-molecule junction remained intact during the push-pull cycle. For each trace, the conductance was determined by averaging over a 0.2 nm segment of the trace during the hold period immediately following the push event and immediately preceding the pull event. Traces were selected if both values fell within ±1 order of magnitude of the most probable conductance of the low conductance state, as determined from corresponding 1D histograms obtained using a linear piezo ramp (e.g., **Figure 3a** for **Os2** and **Figure 13b** for **MTh**/**P4SMe**). These selected traces were used to construct 2D conductance-time histograms.

Two-dimensional cross-correlation (covariance) histograms[21,22] were constructed following the methods outlined by Halbritter *et al.*[23] Individual conductance-displacement traces were converted into logarithmically binned conductance histograms using a bin width of 100 bins per decade in conductance. For each trace r, the number of data points falling into conductance bin i is denoted $N_i(r)$. The mean occupancy of each bin was calculated over all traces as

$$\langle N_i(r) \rangle_r = \frac{1}{R} \sum_{r=1}^{R} N_i(r)$$

where R is the total number of traces. This is equivalent to a standard 1D conductance histogram. Deviations from the mean for each conductance bin were then defined on a trace-by-trace basis as

$$\delta N_{i/j}(r) = N_{i/j}(r) - \langle N_{i/j}(r) \rangle_r$$

The covariance between bins *i* and *j* was computed as

$$C_{ij} = \langle \delta N_i(r) \delta N_j(r) \rangle_r = \frac{1}{R} \sum_{r=1}^{R} \delta N_i(r) \delta N_j(r)$$

where the average is taken over all traces, yielding a matrix corresponding to the 2D covariance histogram. To facilitate comparison across datasets, covariance histograms were normalized to provide 2D correlation histograms,

$$\rho_{ij} = \frac{C_{ij}}{\sqrt{\langle \delta N_i(r)^2 \rangle_r \langle \delta N_j(r)^2 \rangle_r}}$$

in which the normalized correlation coefficients, ρ_{ij}, lie between −1 and 1. In these logarithmically binned 2D histograms, positive (negative) values indicate correlated (anticorrelated) fluctuations in bin occupancies across traces.

Standard Electrochemical Methods

Standard electrochemical measurements were performed under an argon atmosphere using a CHI760E bipotentiostat (CH Instruments, Austin, TX, USA) with argon or nitrogen-sparged solutions of 0.1 M tetrabutylammonium hexafluorophosphate (^{n}Bu$_4$NPF$_6$) in CH_2Cl_2. Unless otherwise stated, plotted equilibrium voltammograms were obtained at a scan rate of 0.1 V s^{-1} and are not corrected for iR_s. Studies employed glassy carbon disc working electrodes (Ø = 3 mm, CH Instruments), mechanically polished using an alumina slurry prior to use. Pt wire reference and counter electrodes were cleaned by annealing in an oxyhydrogen flame. Analyte solutions were between 0.1-1 mM. Potentials are reported relative to $[Cp_2Fe]^+/[Cp_2Fe]$, measured against an internal Cp^*_2Fe reference (−0.532 mV vs $[Cp_2Fe]^+/[Cp_2Fe]$).

Computational Details

Tunnel Coupling

Density functional theory (DFT) calculations were performed using the Q-Chem 5.4.2 program, using the molecular editor and visualization package IQMol 2.15.1.[24] Input structures of simplified **Os1**, **Si1**, and **C1** models comprising just two thioether contact groups – **Os1h**, **Si1h**, and **C1h**, respectively – were constructed by addition of those groups to the parent structures determined through single-crystal X-ray diffraction.[2,25,26] The geometries of these input structures were subsequently separately optimized without gold clusters at the PBE[27] or B3LYP level of theory, using in each case a 6-31G** basis for light atoms and LACVP for osmium (and for gold, below).

Isosurface plots for the frontier orbitals of these isolated molecules calculated using the B3LYP functional are provided in **Figure S21**.

Single gold atoms were next added, linked to the sulfur atoms of these structures, which were then subjected to further geometry optimization with both functionals. The difference in energies between the HOMO and LUMO levels of the molecules bound to the Au_1 clusters (= 2t, a measure of the tunnel coupling[28,29]) was used to calculate $4t^2$. Isosurface plots for these frontier orbitals, calculated using the B3LYP functional, are provided for the **Os1h** model bound to Au_1 clusters in **Figure S23**.

Geometry optimizations were considered converged when the gradient, and either the energy or atomic displacement, satisfied the convergence criteria (energy = 10×10^{-8}, gradient = 10×10^{-6}, atomic displacement = 1200×10^{-6}; all values in atomic units [a.u.]). Unless otherwise stated, calculations used the direct inversion in the iterative subspace (DIIS) self-consistent field (SCF) optimization algorithm, using an on-the-fly (automated) superposition of atomic densities (AUTOSAD) initial guess. The SCF cycle was considered converged when the wave function error between consecutive SCF cycles was less than 10^{-8} a.u. When using the PBE functional, the geometries of model compounds bound to Au_1 clusters were optimized using the geometric direct minimization (GDM) self-consistent field optimization algorithm. The SCF cycle was considered converged when the wave function error between consecutive SCF cycles was less than 10^{-4} a.u.

Ab Initio Quantum Transport Calculations Details

Our ab initio transport calculations were performed using the FHI-aims package,[30] which implements a closed-shell formulation of Kohn-Sham density functional theory. We employed the PBE exchange-correlation functional[27] as a non-empirical, generalized gradient approximation to the exchange-correlation energy. Scalar relativistic effects were included through the zeroth-order regular approximation (ZORA) to account for relativistic corrections to the kinetic energy.[31] FHI-aims employs an optimized all-electron numeric atom-centered basis set. For this study, we considered the "light" computational settings, which correspond roughly to double-zeta basis set quality. The ground-state calculations were converged using reliable criteria for the self-consistent field cycle: 10^{-5} electrons/Å^3, for the difference in the particle density between consecutive SCF iterations; 10^{-7} eV, for the difference in the total energy; 10^{-4} eV, for the difference of the sum of Kohn-Sham eigenvalues and 10^{-4} eV/Å, for the difference of the forces.

The geometries of the model molecular junctions were determined using a well-established two-step process. First, the positions of the molecular atoms and the apex of the electrodes were optimized using the trust-radius enhanced variant of the Broyden-Fletcher-Goldfarb-Shanno algorithm[30] implemented in FHI-aims. For this optimization, we employ pyramidal gold clusters consisting of up to 11 gold atoms per pyramid. The molecular junction geometries were considered to be structurally relaxed only when all the components of the residual forces per atom were below the threshold value of 10^{-2} eV/Å. Next, the optimized molecular and tip geometries from previous step were held fixed while additional layers of gold atoms were added to the outer planes of the previously optimized electrode tips. This ensures proper screening of excess charge and accurate level alignment for the subsequent quantum transport calculations.

The energy-dependent electronic transmission functions were computed within the linear response regime using the non-equilibrium Green's function formalism, as implemented in the AITRANSS transport module.[32–34] Each junction electrode was represented by a pyramidal face-centered cluster consisting of 37 atoms, cut from a crystal grown in the (111) direction with closest interatomic distance of 2.88 Å. The electrode self-energies were approximated by an energy-independent (Markovian) local model, given by $\Sigma(\mathbf{r}, \mathbf{r}') = i\eta(\mathbf{r})\delta(\mathbf{r} - \mathbf{r}')$. The local absorption rate, $\eta(\mathbf{r})$, was fine-tuned to ensure that the electronic transmission remained stable under smooth, moderate variations in $\eta(\mathbf{r})$ and was considered to be nonzero only in the subspace corresponding to the outermost layers of the finite cluster.

Geometries and Absolute Energies

Atomic Cartesian coordinates (in .xyz files) and total energies for all optimized geometries are provided as additional supporting information in the file *Additional-Computational-Data.zip*.

2. Synthetic Details

Tetrakis(2,5-dimethyl-4'-(methylthio)-[1,1'-biphenyl]-4-yl)osmium(IV) ***(Os2)***

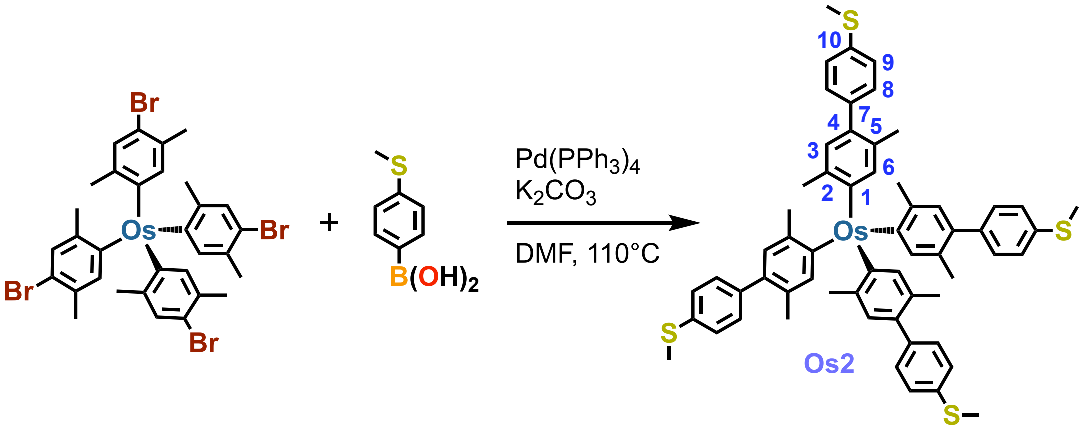

This compound was prepared using an adapted literature method.[35] A mixture of tetrakis(4-bromo-2,5-dimethylphenyl)osmium(IV) (0.166 g, 0.179 mmol), 4-(methylthio)phenylboronic acid (0.196 g, 1.17 mmol), $Pd(PPh_3)_4$ (0.083 g, 0.072 mmol), and K_2CO_3 (0.143 g, 1.03 mmol) in DMF (5 mL) was heated with stirring to 110°C for 3 d. After cooling to room temperature, solvent was removed under vacuum. The crude product was dissolved in CH_2Cl_2, pre-absorbed on Celite, then purified by column chromatography on a hexanes-packed SiO_2 column, eluting with 0:1→1:1 v/v CH_2Cl_2-hexanes. R_f = 0.49 (SiO_2, 1:1 v/v CH_2Cl_2-hexanes). Removal of solvent from selected fractions provided a black solid (0.067 g, 34%). ^{1}H NMR (CD_2Cl_2, 400 MHz): δ (ppm) δ 7.31 (s, 16H, aryl $C_{8/9}$-*H*), 6.83 (s, 4H, aryl C_6-*H*), 6.76 (s, 4H, aryl C_3-*H*), 2.52 (s, 12H, -SC*H*$_3$), 2.44 (s, 12H, C_2-C*H*$_3$), 2.26 (s, 12H, C_5-C*H*$_3$). $^{13}C\{^1H\}$ NMR (CD_2Cl_2, 100 MHz): δ (ppm) 141.39 (aryl, *C*$_4$-aryl), 138.28 (aryl), 138.12 (aryl), 138.06 (aryl), 137.60 (aryl, *C*$_{10}$-SMe), 135.92 (aryl, *C*$_6$-H), 131.28 (aryl, *C*$_5$-Me), 130.49 (aryl, *C*$_{8/9}$-H), 129.28 (aryl, *C*$_3$-H), 126.47 (aryl, *C*$_{8/9}$-H), 25.62 (C_2-*C*H$_3$), 20.55 (C_5-*C*H$_3$), 15.99 (-S*C*H$_3$). HR-MS (MALDI+) *m/z*: 1100.3193 ($[M]^+$ calc. for $C_{60}H_{60}OsS_4$: 1100.3193).

Tetrakis(2,5-dimethyl-4''-(methylthio)-[1,1':4',1''-terphenyl]-4-yl)osmium(IV) ***(Os3)***

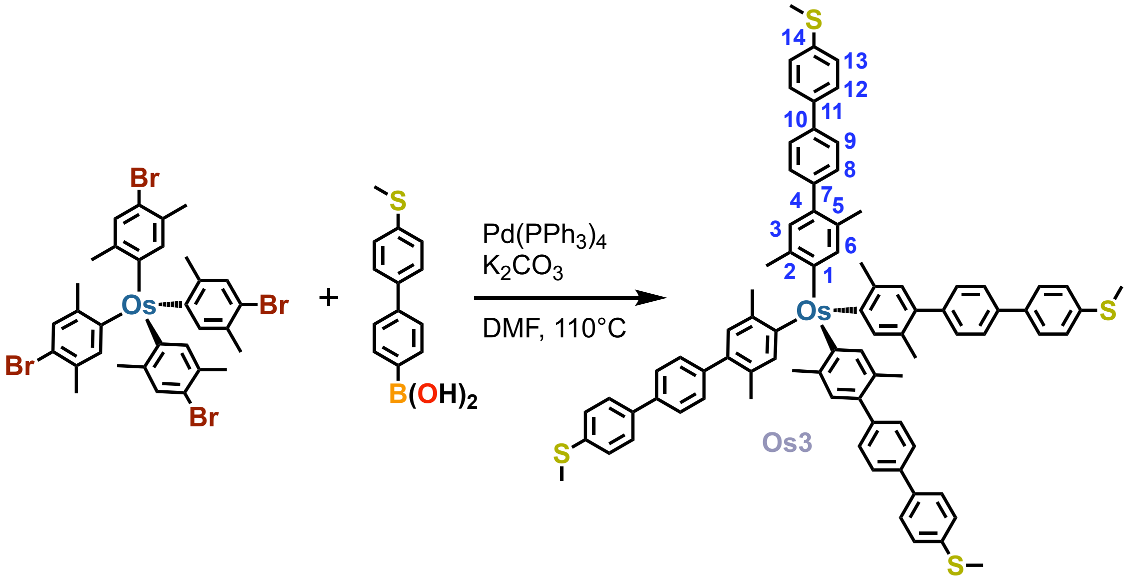

This compound was prepared using an adapted literature method.[35] A mixture of tetrakis(4-bromo-2,5-dimethylphenyl)osmium(IV) (0.097 g, 0.105 mmol), 4-(4-methylthiophenyl)phenylboronic acid (0.165 g, 0.676 mmol), $Pd(PPh_3)_4$ (0.063 g, 0.055 mmol), and K_2CO_3 (0.095 g, 0.687 mmol) in DMF (5 mL) was heated with stirring to 110°C for 3 d. After cooling to room temperature, solvent was removed under vacuum. The crude product was dissolved in CH_2Cl_2, pre-absorbed on Celite, then purified by column chromatography on a hexanes-packed SiO_2 column, eluting with 0:1→1:1 v/v CH_2Cl_2-hexanes. $R_f = 0.45$ (SiO_2, 1:1 v/v CH_2Cl_2-hexanes). Removal of solvent from selected fractions provided a black solid (0.017 g, 12%) that was subsequently stored at −20°C. ^{1}H NMR ($CDCl_3$, 400 MHz): δ (ppm) 7.63 (d, 8H, J = 8.4 Hz, aryl-H), 7.59 (d, 8H, J = 8.4 Hz, aryl-H), 7.46 (d, 8H, J = 8.4 Hz, aryl-H), 7.35 (d, 8H, J = 8.5 Hz, aryl-H), 6.94 (s, 4H, aryl C_6-H), 6.80 (s, 4H, aryl C_3-H), 2.54 (s, 12H, -SCH_3), 2.47 (s, 12H, C_2-CH_3), 2.31 (s, 12H, C_5-CH_3). ^{13}C{^{1}H} NMR ($CDCl_3$, 101 MHz): δ (ppm) 141.08 (aryl, C_4-aryl), 140.39 (aryl, C_7-aryl), 138.95 (aryl), 138.23 (aryl), 138.03 (aryl), 137.79 (aryl), 137.71 (aryl), 136.57 (aryl, C_6-H), 130.84 (aryl, C_5-Me), 130.35 (aryl $C_{8/9}$-H), 129.09 (aryl, C_3-H), 127.53 (aryl C-H), 127.12 (aryl C-H), 126.50 (aryl C-H), 25.69 (C_2-CH$_3$), 20.61 (C_5-CH$_3$), 16.07 (-SCH$_3$). HR-MS (MALDI+) *m/z*: 1404.4428 ([M]$^+$ calc. for $C_{84}H_{76}OsS_4$: 1404.4445).

Tetrakis(4-(methylthio)phenyl)silane ***(Si1)***

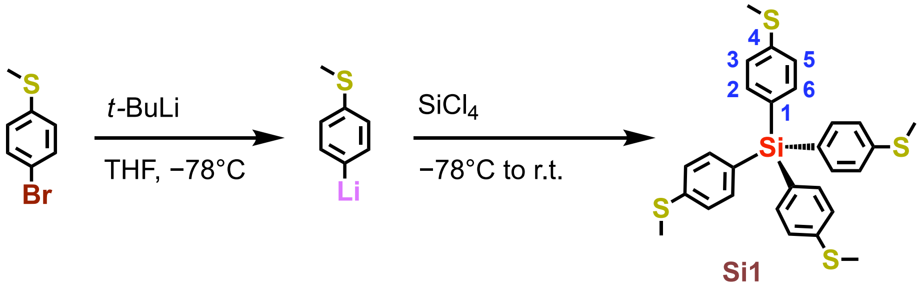

Si1

This compound was prepared using an adapted literature method.[36] A solution of 1.6 M *t*-BuLi in pentane (6.2 mL, 9.9 mmol) was added dropwise at −78°C with stirring to 4-bromothioanisole (1.004 g, 4.943 mmol) in dry THF (7.5 mL). After 2 h, silicon tetrachloride (0.13 mL, 1.1 mmol) was added over a period of ~10 min. The cooling bath was then removed, and the mixture warmed to room temperature overnight. Saturated ammonium chloride solution (2 mL) was added, whereby the mixture was extracted with dichloromethane (3×15 mL). The combined organic layers were then washed with brine (3×15 mL), dried over anhydrous sodium sulfate, and filtered. Solvent was removed by rotary evaporation, whereby the crude product was dissolved in CH_2Cl_2, pre-absorbed on Celite, then purified by column chromatography on a hexanes-packed SiO_2 column, eluting with 0:1→1:1 v/v CH_2Cl_2-hexanes. $R_f = 0.48$ (SiO_2, 1:1 v/v CH_2Cl_2-hexanes). Removal of solvent from selected fractions provided a white solid (0.142 g, 24%). Crystals suitable for single-crystal X-ray diffraction were obtained from slow evaporation of a dichloromethane/hexane solution. ^{1}H NMR ($CDCl_3$, 600 MHz): δ (ppm) 7.42 (d, 8H, *J* = 8.3 Hz, aryl-*H*), 7.23 (d, 8H, *J* = 8.4 Hz, aryl-*H*), 2.48 (-SC*H*3). ^{13}C{^{1}H} NMR ($CDCl_3$, 126 MHz): δ (ppm) 140.95 (aryl, C_4-SMe), 136.65 (aryl, *C*-H), 129.91 (aryl, C_1-Si), 125.47 (aryl, *C*-H), 15.14 (-SCH_3). HR-MS (ESI+) *m/z*: 520.0839 ($[M]^+$ calc. for $C_{28}H_{28}S_4Si$: 520.0843).

Tetrakis(4'-(methylthio)-[1,1'-biphenyl]-4-yl)silane ***(Si2)***

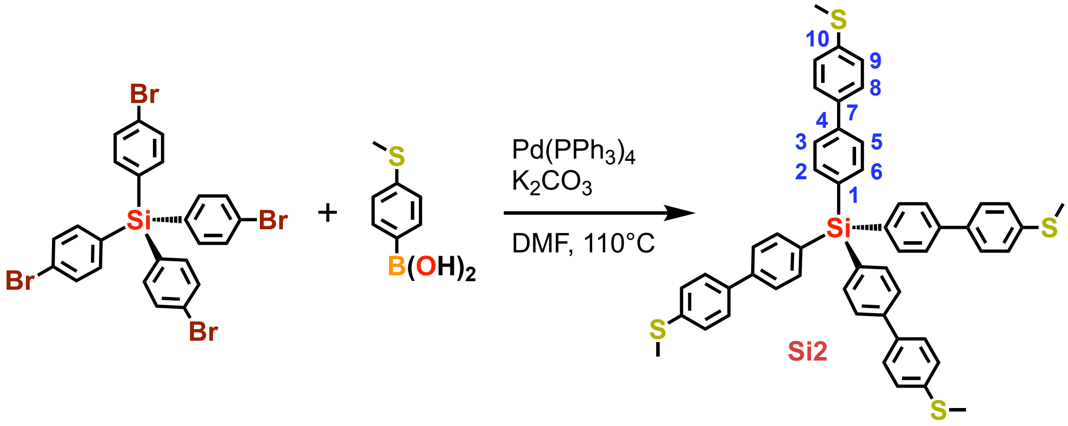

This compound was prepared using an adapted literature method.[35] A mixture of tetrakis(4-bromophenyl)silane (0.109 g, 0.167 mmol), 4-(methylthio)phenylboronic acid (0.158 g, 0.940 mmol), $Pd(PPh_3)_4$ (0.074 g, 0.064 mmol), and K_2CO_3 (0.137 g, 0.991 mmol) in DMF (5 mL) was heated with stirring to 110°C for 3 d. After cooling to room temperature, solvent was removed under vacuum. The crude product was dissolved in CH_2Cl_2, pre-absorbed on Celite, then purified by column chromatography on a hexanes-packed SiO_2 column, eluting with 0:1→1:1 v/v CH_2Cl_2-hexanes. R_f = 0.46 (SiO_2, 1:1 v/v CH_2Cl_2-hexanes). Removal of solvent from selected fractions provided a white solid (0.041 g, 30%). ^{1}H NMR (CD_2Cl_2, 400 MHz): δ (ppm) 7.72 (d, 8H, *J* = 8.3 Hz, aryl-*H*), 7.66 (d, 8H, *J* = 8.5 Hz, aryl-*H*), 7.59 (d, 8H, *J* = 8.7 Hz, aryl-*H*), 7.34 (d, 8H, *J* = 8.7 Hz, aryl-*H*), 2.52 (-SC*H*$_3$). ^{13}C{^{1}H} NMR (CD_2Cl_2, 101 MHz): δ (ppm) 142.05 (aryl, *C*-R), 138.78 (aryl, C_{10}-SMe), 137.64 (aryl, *C*-R), 137.28 (aryl, *C*-H), 133.18 (aryl, *C*-R), 127.79 (aryl, *C*-H), 127.03 (aryl, *C*-H), 126.64 (aryl, *C*-H), 15.84 (-S*C*H$_3$). HR-MS (MALDI+) *m/z*: 824.2084 ([M]$^+$ calc. for $C_{52}H_{44}S_4Si$: 824.2095).

***Si2** (−2PhSMe)*

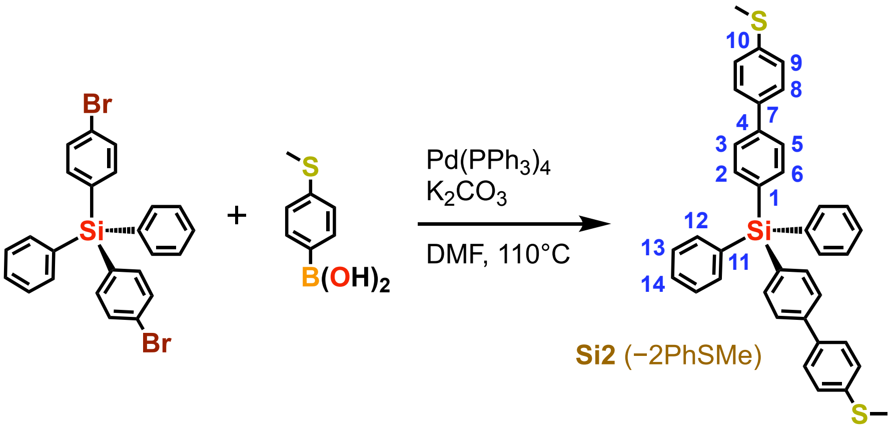

This compound was prepared using an adapted literature method.[35] A mixture of bis(4-bromophenyl)diphenylsilane (0.114 g, 0.231 mmol), 4-(methylthio)phenylboronic acid (0.093 g, 0.55 mmol), Pd(PPh$_3$)$_4$ (0.110 g, 0.095 mmol), and K$_2$CO$_3$ (0.154 g, 1.11 mmol) in DMF (5 mL) was heated with stirring to 110°C for 3 d. After cooling to room temperature, solvent was removed under vacuum. The crude product was dissolved in CH$_2$Cl$_2$, pre-absorbed on Celite, then purified by column chromatography on a hexanes-packed SiO$_2$ column, eluting with 0:1→1:1 v/v CH$_2$Cl$_2$-hexanes. R$_f$ = 0.58 (SiO$_2$, 1:1 v/v CH$_2$Cl$_2$-hexanes). Removal of solvent from selected fractions provided a white solid (0.020 g, 15%). ^{1}H NMR (CDCl$_3$, 500 MHz): δ (ppm) 7.67 (d, 4H, J = 8.2 Hz, aryl-H), 7.64 (d, 4H, J = 6.6 Hz, aryl-H), 7.61 (d, 4H, J = 8.2 Hz, aryl-H), 7.56 (d, 4H, J = 8.5 Hz, aryl-H), 7.47 (m, 2H, J = 7.4 Hz, aryl-H_{14}), 7.42 (m, 4H, J = 6.9 Hz, aryl-H), 7.34 (d, 4H, J = 8.4 Hz, aryl-H), 2.53 (s, 6H, -SCH_3). ^{13}C{^{1}H} NMR (CDCl$_3$, 126 MHz): δ (ppm) 141.71 (aryl, C-R), 138.13 (aryl, C_{10}-R), 137.75 (aryl, C-R), 137.06 (aryl, C-H), 136.54 (aryl, C-H), 134.28 (aryl, C-R), 133.02 (aryl, C-R), 129.83 (aryl, C_{14}-H), 128.10 (aryl, C-H), 127.61 (aryl, C-H), 127.01 (aryl, C-H), 126.39 (aryl, C-H), 15.94 (-SCH$_3$). HR-MS (ESI+) m/z: 580.1731 ([M]$^+$ calc. for C$_{38}$H$_{32}$S$_2$Si: 580.1715).

*Tetrakis(4-(methylthio)phenyl)methane **(C1)***

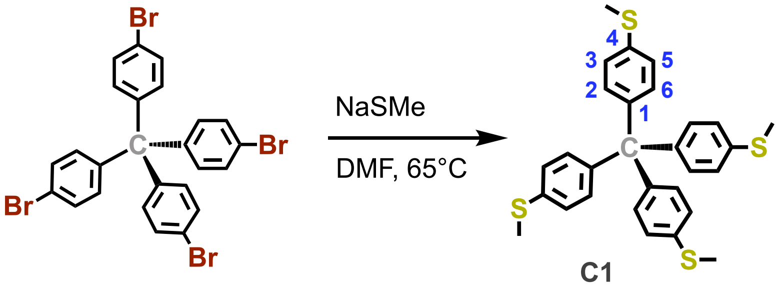

C1

This compound was prepared using an adapted literature method.[37] A solution of tetrakis(4-bromophenyl)methane (0.201 g, 0.316 mmol) in DMF (2 mL) was added to solution of sodium thiomethoxide (0.135 g, 1.93 mmol) in DMF (2 mL). The resulting mixture was heated to 65°C and stirred for 1 d. After cooling, solvent was removed under vacuum. The crude product was dissolved in CH_2Cl_2, pre-absorbed on Celite, then purified by column chromatography on a hexanes-packed SiO_2 column, eluting with 0:1→1:1 v/v CH_2Cl_2-hexanes. $R_f = 0.47$ (SiO_2, 1:1 v/v CH_2Cl_2-hexanes). Removal of solvent from selected fractions provided a white solid (0.027 g, 17%). ^{1}H NMR (CD_2Cl_2, 400 MHz): δ (ppm) 7.12 (s, 16H, aryl-*H*), 2.45 (s, 12H, -SCH_3). ^{13}C{^{1}H} NMR (CD_2Cl_2, 101 MHz): δ (ppm) 143.72 (aryl, C_1-C(*sp*^{3})), 136.68 (aryl, C_4-SMe), 131.59 (aryl, *C*-H), 125.73 (aryl, *C*-H), 15.66 (-S*C*H_3). HR-MS (ESI+) *m/z*: 504.1066 ($[M]^+$ calc. for $C_{29}H_{28}S_4$: 504.1074).

Tetrakis(4'-(methylthio)-[1,1'-biphenyl]-4-yl)methane ***(C2)***

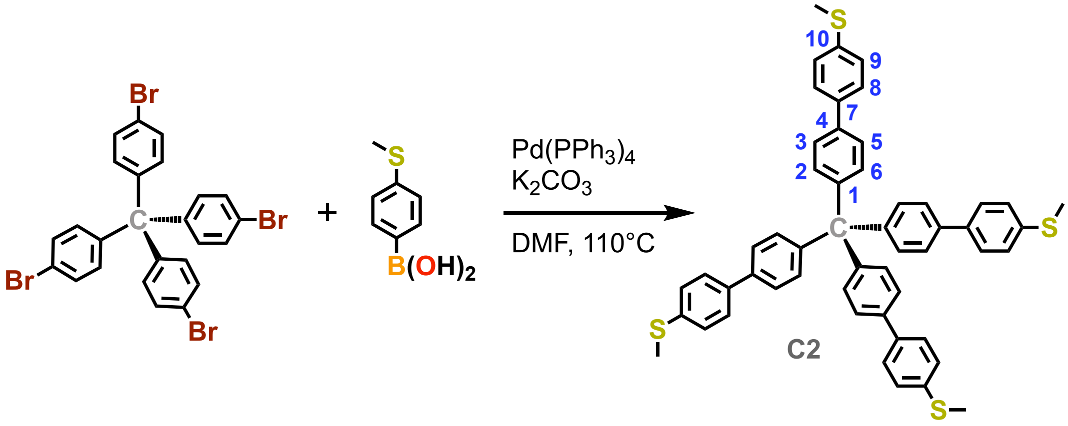

This compound was prepared using an adapted literature method.[35] A mixture of tetrakis(4-bromophenyl)methane (0.111 g, 0.175 mmol), 4-(methylthio)phenylboronic acid (0.180 g, 1.07 mmol), $Pd(PPh_3)_4$ (0.073 g, 0.063 mmol), and K_2CO_3 (0.131 g, 0.948 mmol) in DMF (5 mL) was heated with stirring to 110°C for 3 d. After cooling to room temperature, solvent was removed under vacuum. The crude product was dissolved in CH_2Cl_2, pre-absorbed on Celite, then purified by column chromatography on a hexanes-packed SiO_2 column, eluting with 0:1→1:1 v/v CH_2Cl_2-hexanes. $R_f = 0.45$ (SiO_2, 1:1 v/v CH_2Cl_2-hexanes). Removal of solvent from selected fractions provided a white solid (0.013 g, 9%). ^{1}H NMR ($CDCl_3$, 500 MHz): δ (ppm) 7.53 (m, 16H, aryl-*H*), 7.38 (d, 4H, *J* = 8.5 Hz, aryl-*H*), 7.31 (d, 4H, *J* = 8.5 Hz, aryl-*H*), 2.52 (s, 12H, -SCH_3). ^{13}C{^{1}H} NMR ($CDCl_3$, 126 MHz): δ (ppm) 145.84 (aryl, *C*R_3), 138.14 (aryl, *C*R_3), 137.71 (aryl, *C*R$_3$), 137.48 (aryl, *C*R$_3$), 131.67 (aryl, *C*-H), 127.43 (aryl, *C*-H), 127.06 (aryl, *C*-H), 126.06 (aryl, *C*-H), 16.02 (-SCH$_3$). HR-MS (EI+) *m/z*: 808.2321 ($[M]^+$ calc. for $C_{53}H_{44}S_4$: 808.2326).

3. X-Ray Crystallography

Table 1. Data collection and structure refinement parameters for **Si1** ($SiS_4C_{28}H_{28}$).

Formula	$SiS_4C_{28}H_{28}$
Temperature, K	100.0(3)
CCDC number	2480811
Formula weight	520.83
Space group	$I\bar{4}$
***a*, Å**	13.3502(2)
***b*, Å**	13.3502(2)
***c*, Å**	7.3339(2)
α, deg	90
β, deg	90
γ, deg	90
V, Å^3	1307.11(5)
Z	2
D_{calc}, g cm^{-3}	1.323
μ, mm^{-1}	3.884
λ, Å	1.54184
$2\theta_{max}$, deg	147.27
Total reflections (R_{int})	1310 (0.046)
Unique reflections	1279
Parameters refined	76
Restraints used	0
R_1, wR_2 [$I > 2\sigma(I)$]	0.026, 0.068
R_1, wR_2 (all data)	0.027, 0.069
Goodness of fit	1.054
Diff. peak/hole, e Å^{-3}	0.27/-0.14

The crystal structure determination of the compound **Si1** ($SiS_4C_{28}H_{28}$) revealed that the complex crystallizes in tetragonal cell with space group $I\bar{4}$. The asymmetric unit is composed of only a quarter of the complex. The central Si atom is surrounded by four $C_6H_4SCH_3$ ligands, with a Si−C bond distance of 1.875(2) Å. The S atom on the *para*-substituent ($-SCH_3$) group lies coplanar with the phenyl ring, while the C atom deviates from the phenyl ring plane by 0.302 Å^3. The view along the c-axis shows the formation of columns. The Si-Si interatomic distance inside the columns is 7.334(1) and between the columns is 10.127(1) Å. The intermolecular distance of the aryl ligand

C5−H and C6−H atoms to the centroid on the neighboring phenyl ring are 3.039 and 3.248 Å and hydrogens atom at C2 and C4 atoms display the C−H···S distance 3.155 and 3.079 Å respectively.

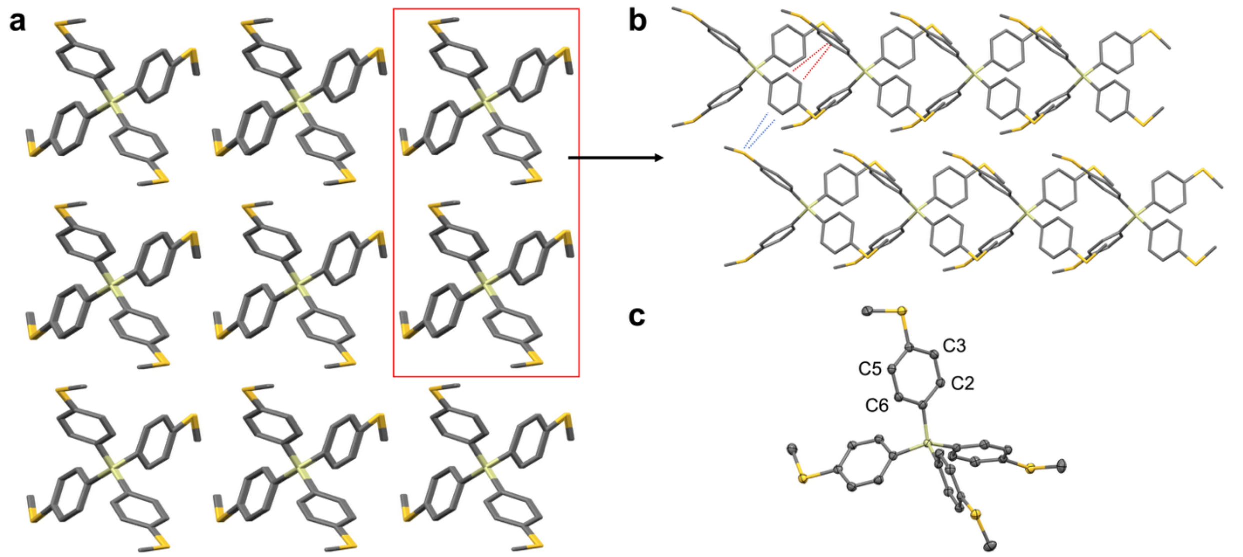

Figure S1. (a) A view of the crystal packing of **Si1** along the c-axis, highlighting columns; **(b)** columnar view of **Si1** showing CH···π (phenyl ring) distances indicated by red lines and CH···S distances indicated by blue lines; **(c)** Crystal structure of **Si1**. Thermal ellipsoids at 50% probability level (color scheme: C = grey, S = yellow, Si = light green). Hydrogens are omitted for clarity.

4. Electrochemistry

Table S2. Electrochemical data for selected Os(aryl)$_4$ complexes.[a]

	redox transition	$E_{1/2}$ (V)	E_{pa} (V)	E_{pc} (V)	ΔE (V)	i_{pa}/i_{pc}	ref.
Os(C_8H_8-SMe)$_4$ (**Os1**)	1−/0	−1.955	−1.920	−1.990	0.070	0.94	[5]
	0/1+	+0.018	+0.056	−0.020	0.076	0.99	
	1+/2+	+0.650	+0.700	+0.600	0.100	0.98	
Os(C_8H_8-C_6H_4-SMe)$_4$ (**Os2**)	1−/0	−1.906	−1.868	−1.944	0.076	1.05	this work
	0/1+	+0.228	+0.271	+0.186	0.085	1.02	
	1+/2+	-	-	-	-	-	
Os(C_8H_8-C_6H_4-C_6H_4-SMe)$_4$ (**Os3**)	1−/0	−1.927	−1.861	−1.994	0.133	1.02	this work
	0/1+	+0.222	+0.273	+0.172	0.101	1.02	
	1+/2+	-	-	-	-	-	
Os(C_8H_9)$_4$	1−/0	−2.008	−1.969	−2.047	0.078	0.98	[2]
	0/1+	+0.244	+0.281	+0.208	0.073	1.00	
	1+/2+	-	-	-	-	-	
Os(C_8H_8-C_6H_4-C_6H_5)$_4$	1−/0	-	-	-	-	-	[38]
	0/1+	+0.21	-	-	-	-	
	1+/2+	+1.05	-	-	-	-	

[a] Scan rate = 0.1 V s^{-1}; Supporting electrolyte = ^{n}Bu$_4$NPF$_6$-CH$_2$Cl$_2$; working electrode: glassy carbon; reference electrode, counter electrode: Pt. All potentials are reported relative to $[Cp_2Fe]^+/Cp_2Fe$, corrected for iR_s.

5. UV-Vis Spectroscopy

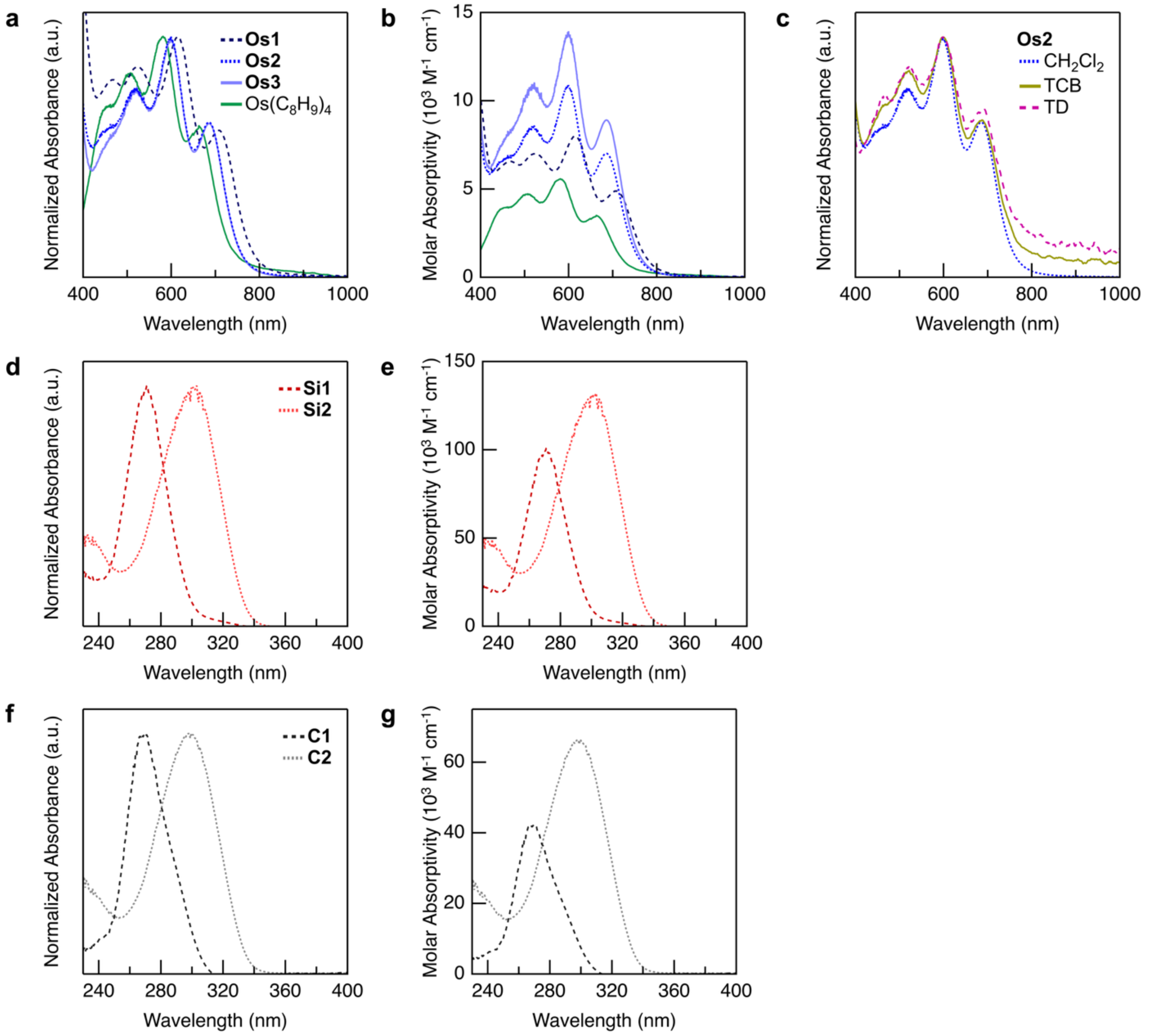

Figure S2. (a-b) Overlaid UV-vis spectra for **Os1**,[5] **Os2**, **Os3**, and Os(xylyl)$_4$[5] (all spectra measured using a 10 mm pathlength cell in CH_2Cl_2, unless stated). In (a), absorbance spectra are normalized to the peak of maximum intensity in the visible region. Data for **Os1-3** are reproduced from **Figure 2c** for convenience. In (b), plots of molar absorptivity against wavelength reveal the extended complexes are more efficient at absorbing visible light. **(c)** Overlaid normalized spectra for **Os2** measured in TCB, TD (1 mm pathlength cell), and CH_2Cl_2 (reproduced from panel (a) and **Figure 2c**). These studies reveal no significant changes to the wavelengths of primary absorption maxima that might indicate bulk protonation/oxidation in the chlorinated solvents. **(d-e)** Plots analogous to those in panels (a) and (b) for **Si1** and **Si2**. **(f-g)** Plots analogous to those in panels (a) and (b) for **C1** and **C2**. Data extracted from these measurements are provided in **Table S3**.

Table S3. Spectroscopic and frontier orbital energy gap data for selected compounds.[a]

	λ_{max} (nm)	ε_{max} (M^{-1} cm^{-1})	E_{opt} (nm)[b]	E_{elec} (V) [c]	ref./comments
$Os(C_8H_8\text{-}SMe)_4$ (**Os1**)	465 525 613 705	6,568 7,004 7,951 4,888	784	1.973	[5]
$Os(C_8H_8\text{-}C_6H_4\text{-}SMe)_4$ (**Os2**)	462 516 598 685	6,707 8,560 10,872 7,020	758	2.134	this work
$Os(C_8H_8\text{-}C_6H_4\text{-}SMe)_4$ (**Os2**) [in TCB]	464 519 598 687	5,521 6,628 7,740 5,056	-	-	this work
$Os(C_8H_8\text{-}C_6H_4\text{-}SMe)_4$ (**Os2**) [in TD]	466 522 600 689	2,622 3,052 3,466 2,414	-	-	this work
$Os(C_8H_8\text{-}C_6H_4\text{-}C_6H_4\text{-}SMe)_4$ (**Os3**)	452sh 519 598 685	7,838 10,890 13,889 8,902	757	2.149	this work
$Os(C_8H_9)_4$	454 503 580 662	3,857 4,710 5,570 3,513	744	2.252	[2], this work
$Si(C_6H_4\text{-}SMe)_4$ (**Si1**)	271	91,780 [d]	300	-	this work
$Si(C_6H_4\text{-}C_6H_4\text{-}SMe)_4$ (**Si2**)	303	132,090 [d]	335	-	this work
$C(C_6H_4\text{-}SMe)_4$ (**C1**)	270	42,277 [d]	304	-	this work
$C(C_6H_4\text{-}C_6H_4\text{-}SMe)_4$ (**C2**)	299	66,442 [d]	333	-	this work

[a] Measured in CH_2Cl_2 unless otherwise stated. [b] Defined here as the longest wavelength at which absorbance reaches ~10% of the peak of maximum intensity in the visible region. [c] Calculated from solution electrochemical studies: $E_{elec} = E_{1/2}(0/1+) - E_{1/2}(1-/0)$. [d] High ε_{max} have been reported for other tetra(oligoaryl)silane and methane complexes. For example, 51,000 M^{-1} cm^{-1} for tetrakis(4-(thiophen-2-yl)phenyl)methane,[39] and up to 1.9×10^6 M^{-1} cm^{-1} for a tetrakis(tetraaryl)silane with ligand arms comprising fluorene groups.[40]

6. Additional Conductance Data

Table S4. Conductance values for selected compounds.[a]

compound/ *peak*	conductance (G_0)			
	TD		TCB	
	low G	*high G*	*low G*	*high G*
Os1	5.3×10^{-5}	6.9×10^{-3}	-	-
Si1	4.1×10^{-5}	6.5×10^{-3}	-	-
C1	3.0×10^{-5}	-[b]	-	-
Os2	1.9×10^{-6}	8.4×10^{-4}	-[c]	8.6×10^{-4}
Os2 (2)	3.2×10^{-6}	7.1×10^{-4}	-[c]	-
Si2	3.5×10^{-7}	9.5×10^{-4}	4.3×10^{-7}	9.7×10^{-4}
Si2 (2)	-	-	3.7×10^{-7}	7.2×10^{-4}
Si2 (−2PhSMe)	2.9×10^{-7}	7.7×10^{-4}	-	-
C2	-[b]	7.6×10^{-4}	6.0×10^{-7}	1.2×10^{-3}
C2 (2)	-	-	6.9×10^{-7}	1.5×10^{-3}
Os3	~2.5×10^{-7}[d]	1.2×10^{-4}	-[c]	1.4×10^{-4}

[a] All values from measurements at V_{bias} = 750 mV from peak fits to histograms (1), unless otherwise stated. Blue shaded entries correspond to repeated measurements. [b] Peak not observed in conductance histograms. [c] Value not reported due to the large apparent conductance variability for this junction geometry when measured in this solvent. [d] This value is only approximate given that the associated conductance feature is not well resolved above our instrument noise floor (**Figure 3a**).

Studies in Tetradecane (TD)

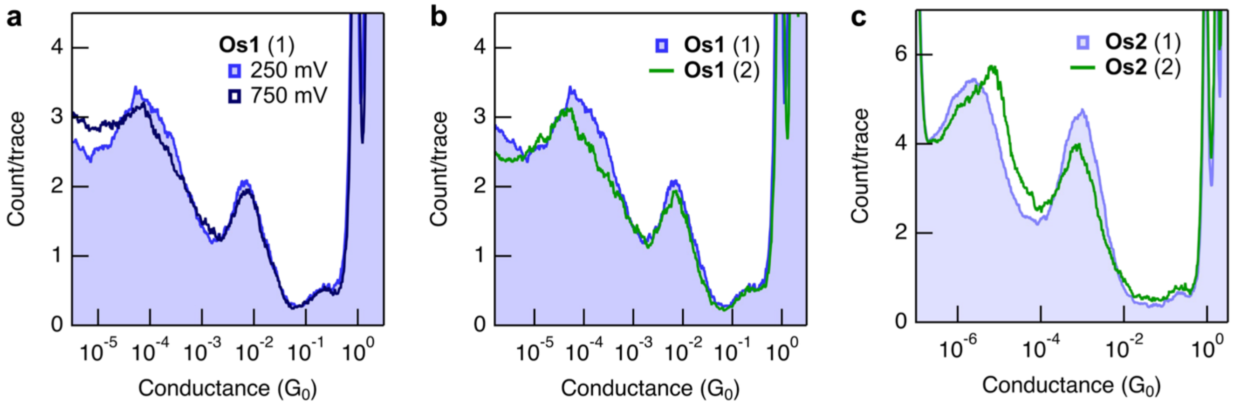

Figure S3. (a) Overlaid 1D histograms for **Os1** measured at different bias voltages show improved peak definition at lower bias, without significant changes in the most probable junction conductance (5.3–6.7×10^{-5} G_0). **(b, c)** Repeated conductance measurements of **Os1** (V_{bias} = 250 mV; 3.7–6.7×10^{-5} G_0) and **Os2** (V_{bias} = 750 mV; 1.9–3.2×10^{-6} G_0; **Table S4**) in TD show greater consistency in the low conductance peak compared to measurements in TCB (factors of 1.8 and 1.7, respectively; see **Figure S7** for TCB measurements of **Os2** and **Os3**).

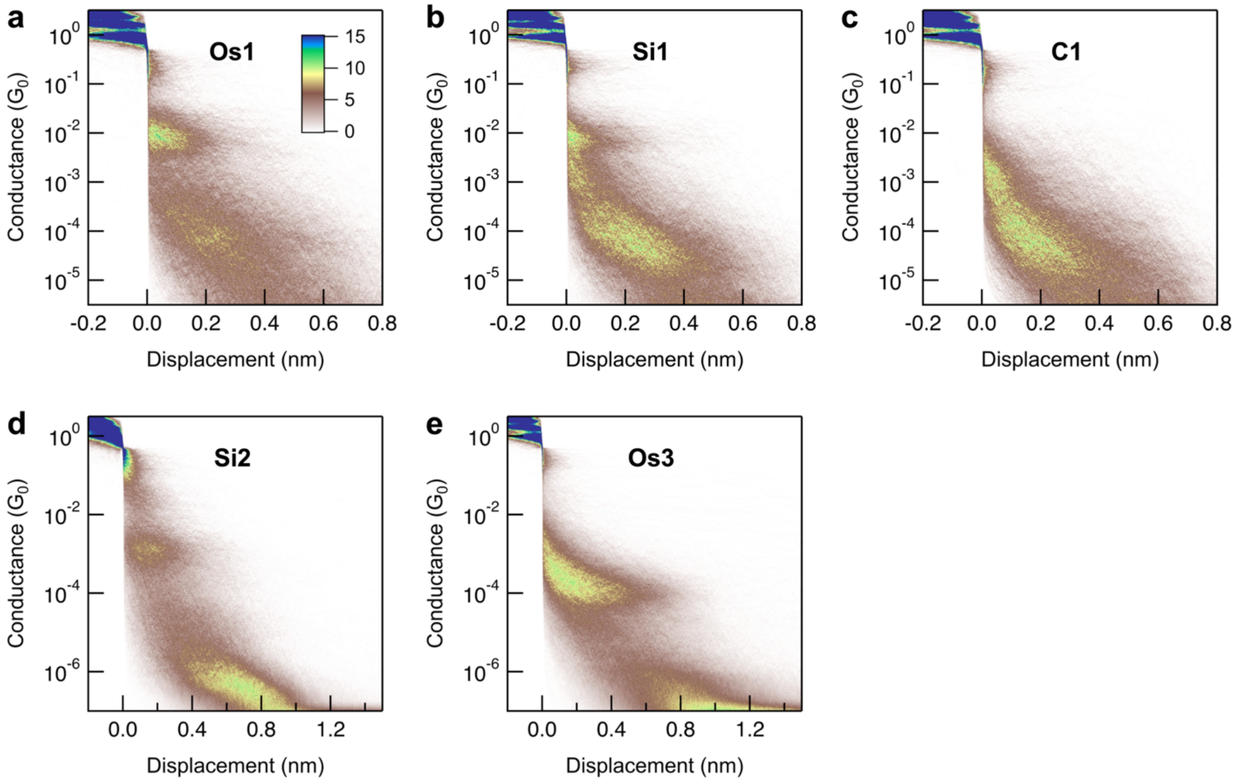

Figure S4. 2D histograms for **(a) Os1**, **(b) Si1**, **(c) C1**, **(d) Si2**, and **(e) Os3**, corresponding to the 1D histograms shown in **Figure 3**.

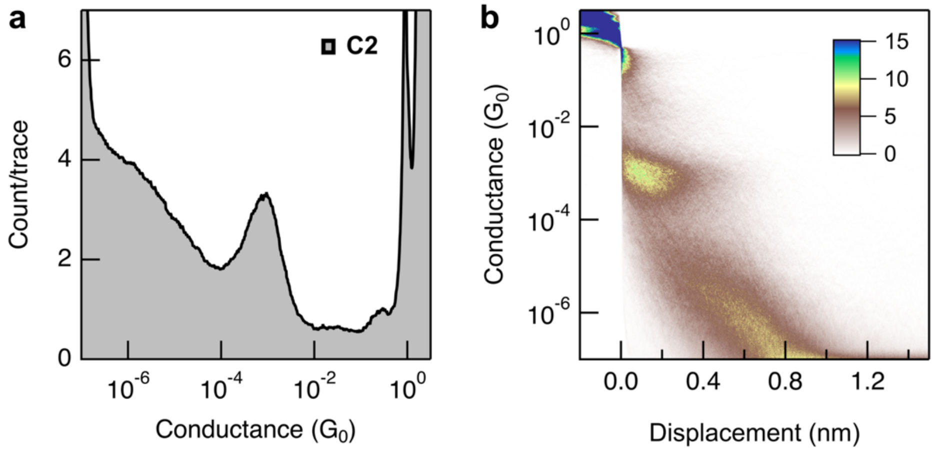

Figure S5. (a) 1D and **(b)** 2D histogram obtained for measurements of a solution of **C2** in TD (V_{bias} = 750 mV). The low conductance feature is absent/poorly resolved.

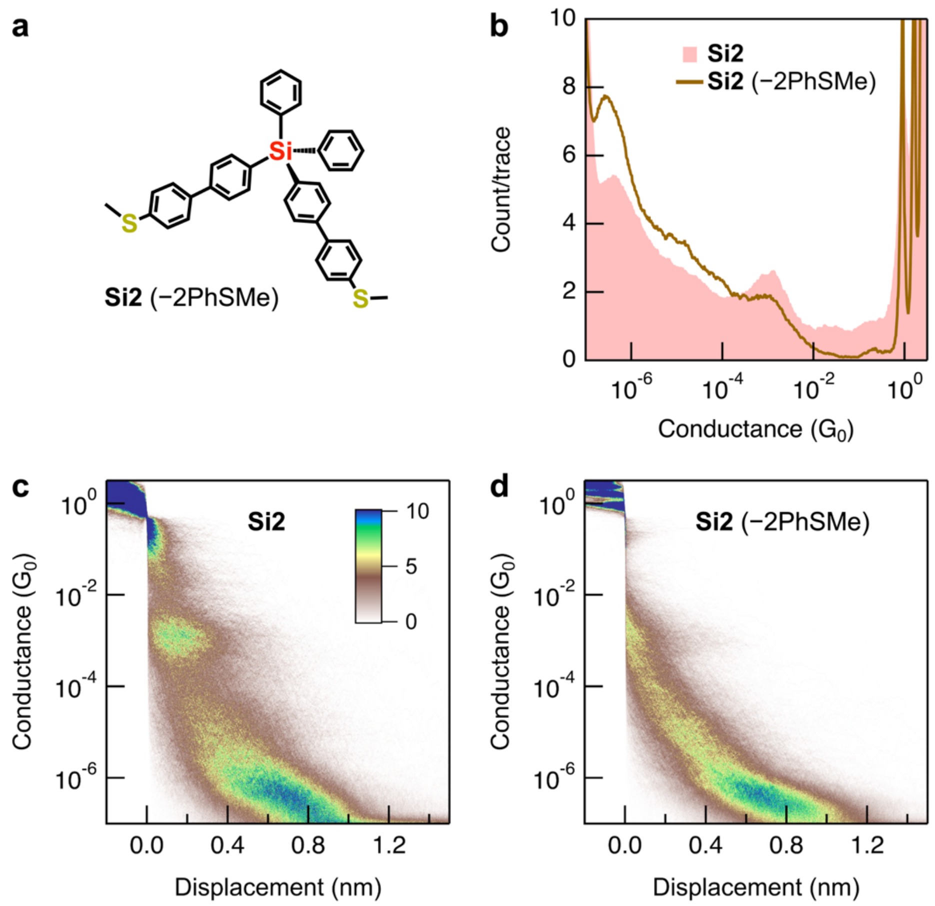

Figure S6. (a) Molecular structure of **Si2** (−2PhSMe), a control compound with only two thioanisole linker groups. **(b)** Overlaid 1D histograms for **Si2** and **Si2 (−2PhSMe)** showing these both exhibit peak features at comparable low conductance (V_{bias} = 750 mV). **(c-d)** 2D histograms corresponding to the 1D histograms shown in panel (b).

Studies in 1,2,4-Trichlorobenzene (TCB)

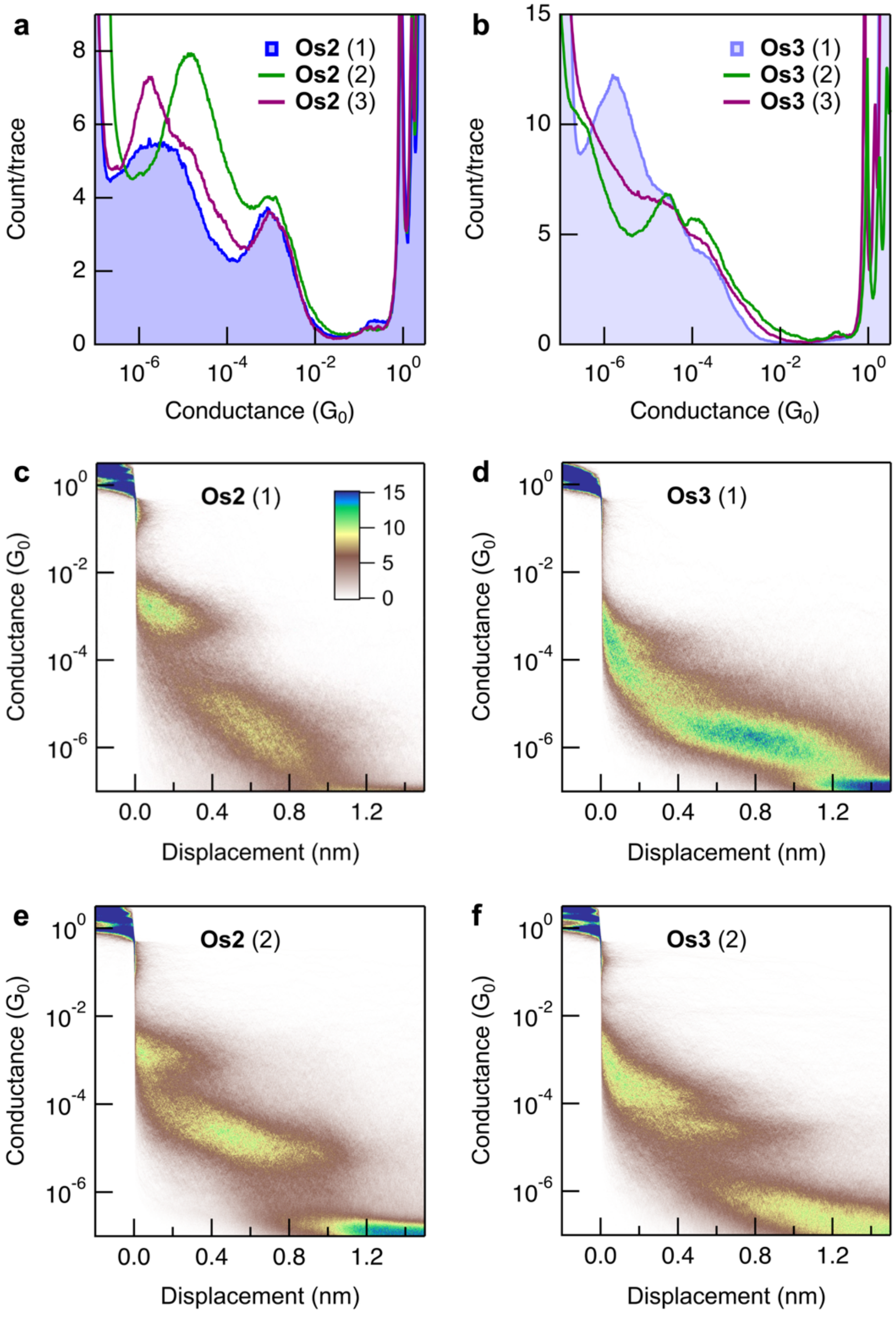

Figure S7. Overlaid 1D histograms for repeated conductance measurements of **(a) Os2** and **(b) Os3** in TCB (V_{bias} = 750 mV). **(c-f)** Example 2D histograms corresponding to selected 1D histograms in (a,b). This data shows that the low conductance features exhibit a large experiment to experiment variability when measured in TCB.

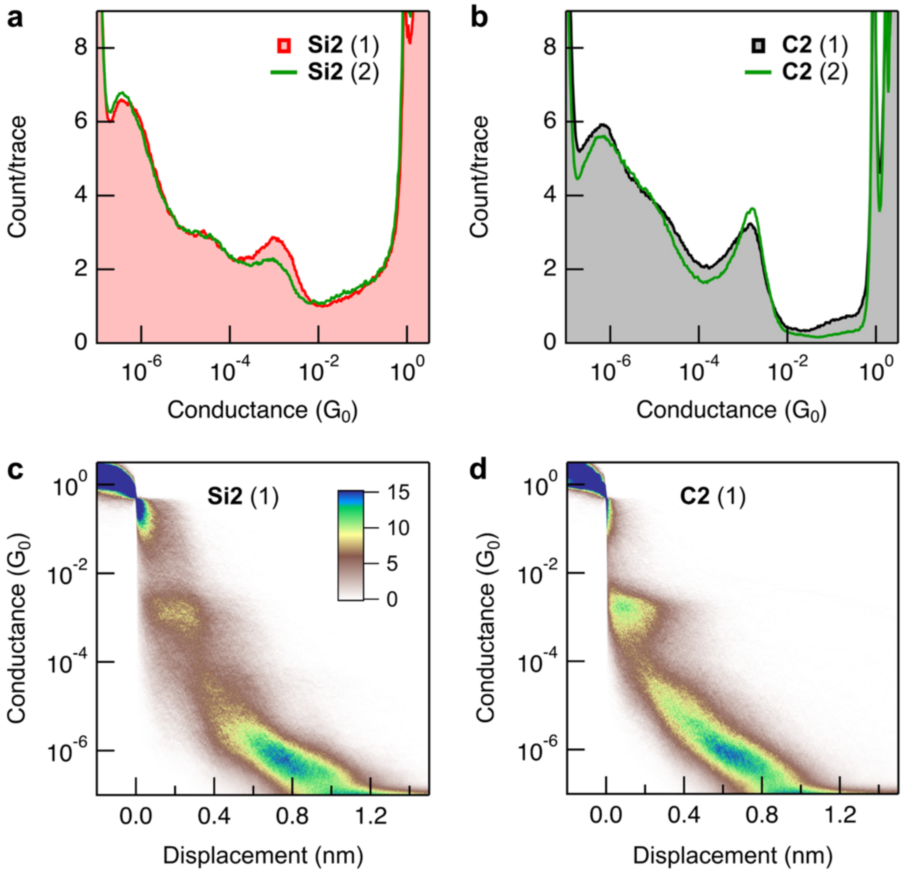

Figure S8. Overlaid 1D histograms for repeated conductance measurements of **(a) Si2** and **(b) C2** in TCB (V_{bias} = 750 mV). **(c-d)** Example 2D histograms corresponding to selected 1D histograms in panels (a) and (b). This data shows that the low conductance features of these organic wires are more reproducible in TCB measurements than those for **Os-*n***. The low conductance peaks for **Si2** and **C2** are both consistent within a factor of 1.2 (**Table S4**).

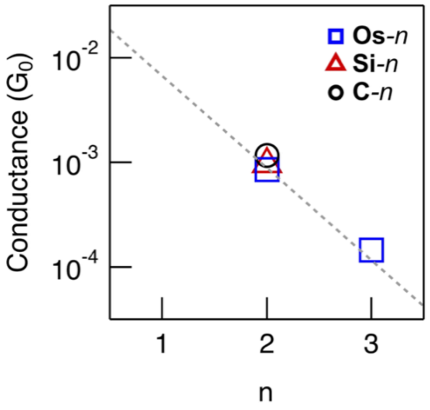

Figure S9. A plot of conductance versus number of aryl groups in each ligand for the high conductance peak feature observed in each series of wires **Os-*n***, **Si-*n***, **C-*n***, measured in TCB. Grey dashed line is the fit of conductance versus *n* for **Os-*n*** measured in TD (**Figure 3e**), included here for comparison.

Analysis of High Conductance Features

The junction geometries associated with the high conductance features observed in measurements of **Os-*n***, **Si-*n***, and **C-*n*** (**Figure 3a-c**) cannot be unambiguously determined from the available data. In the discussion below, we evaluate two plausible scenarios, supported by additional experiments and analyses, while explicitly acknowledging the limitations in uniquely assigning the origin of these features.

Hypothesis 1: Central Atom-Aryl Heterolytic Bond Cleavage

Recent studies have shown that Lewis acidic sites on a gold surface can activate C(sp^3)−S bonds towards heterolytic cleavage, forming junctions comprising chemisorbed Au−S contacts.[41,10,42,43] Such reactions occur under ambient conditions for compounds bearing thioether substituents, −SR, where R is a stable carbocation precursor such as *tert*-butyl, trityl, or cycloheptatrienyl. One proposed mechanism is shown in **Figure S10a** for compounds functionalized with trityl groups, $-CPh_3$, generating the tritylium ion, $[CPh_3]^+$.

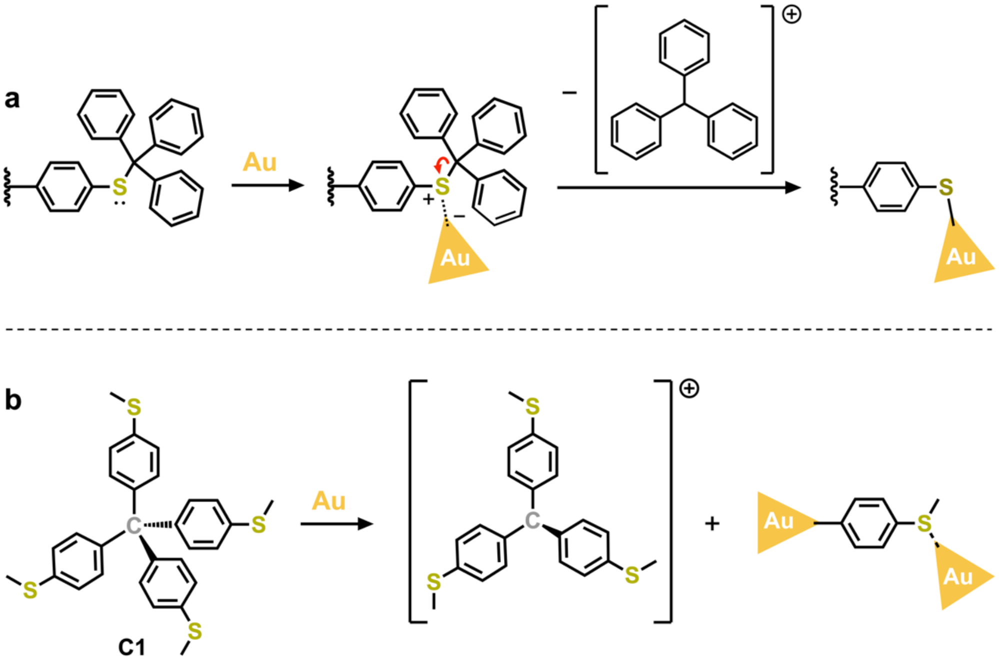

Figure S10. (a) A scheme showing the recently proposed *in situ* reaction of $-S(CPh_3)$ groups at gold electrode surfaces, with loss of the $[CPh_3]^+$ (tritylium) ion and formation of junctions comprising chemisorbed Au−S contacts. **(b)** These systems share structural similarities with the tetraaryl compounds studied in this work. We therefore consider whether analogous central atom−C(sp^2) bond cleavage processes could lead to linker arm dissociation and the formation of junctions with Au−C(sp^2) contacts. This is illustrated here using **C1** as a representative example.

The tetraaryl compounds studied here share structural similarities with trityl groups, comprising a central atom (C, Si, or Os) bound to three aryl substituents. We therefore consider whether such trityl-like motifs could, in principle, undergo *in situ* cleavage of the central atom−C(sp^2) bond at the metal-solution interface, forming junctions comprising Au−C(sp^2) contacts derived from dissociated linker arms. This possibility is illustrated for **C1** in **Figure 10b**. While direct interaction between the gold electrode and the contacted C(sp^2) atom appears sterically hindered, the stability of these tetraaryl compounds in solution, as evidenced by UV-vis (**Figure S2**) and NMR (**Figure S28-S41**), suggests that, if such bond cleavage occurs, it is likely confined to the solution-electrode interface. If formed, such processes would also generate thioether-functionalized trityl-like cations (**Figure 10b**, middle), which could, in principle, also be captured in junction measurements. Related compounds were recently studied by Prindle *et al.*[44] However, these non-chemisorbed species are expected to diffuse into the bulk solution and accordingly may only be present at low concentrations near the interface, reducing the probability that they form junctions. In contrast, the chemisorbed linker fragments would be expected to remain localized at the surface, potentially increasing the probability that they form junctions.[43]

To assess whether these high conductance features could arise from dissociated linker arms, we compared measurements of **Si2** and **C2** with those of **Au2** (structure shown in **Figure 11a**). The **Au2** complex comprises the same biphenyl linker arm as in these tetrahedral compounds, with a pre-installed Au–C(sp^2) bond that enables facile transmetallation to the gold surface. Such complexes have previously been used to probe conductance features observed in measurements of precursors bearing $-SnMe_3$,[45] $-B(OH)_2$,[46] or −I groups,[7] showing these form chemisorbed Au−C(sp^2) contacted junctions. We exclude **Os2** here, as this compound contains a methyl-substituted biphenyl ligand that complicates direct comparison with **Au2**. In **Figure S11b** we overlay 1D conductance histograms obtained from measurements of **Au2**, **C2**, and **Si2** under identical conditions (V_{bias} = 100 mV, 0.5 mM solutions in TCB). These conditions were selected to enable direct comparison with previous studies involving **Au2**.[7] The conductance of junctions formed from **Au2** (2.5×10^{-3} G_0) is similar to, but consistently ~2× higher than, the high conductance features observed for **C2** or **Si2** (1.1 and 1.3×10^{-3} G_0, respectively; **Figure S11a,b**). We also observe a second, well defined, conductance feature in measurements of **Au2** between 10^{-4} and 10^{-5} G_0, which has been attributed to a C(sp^2)−C(sp^2) coupled tetraphenyl dimer.[7]

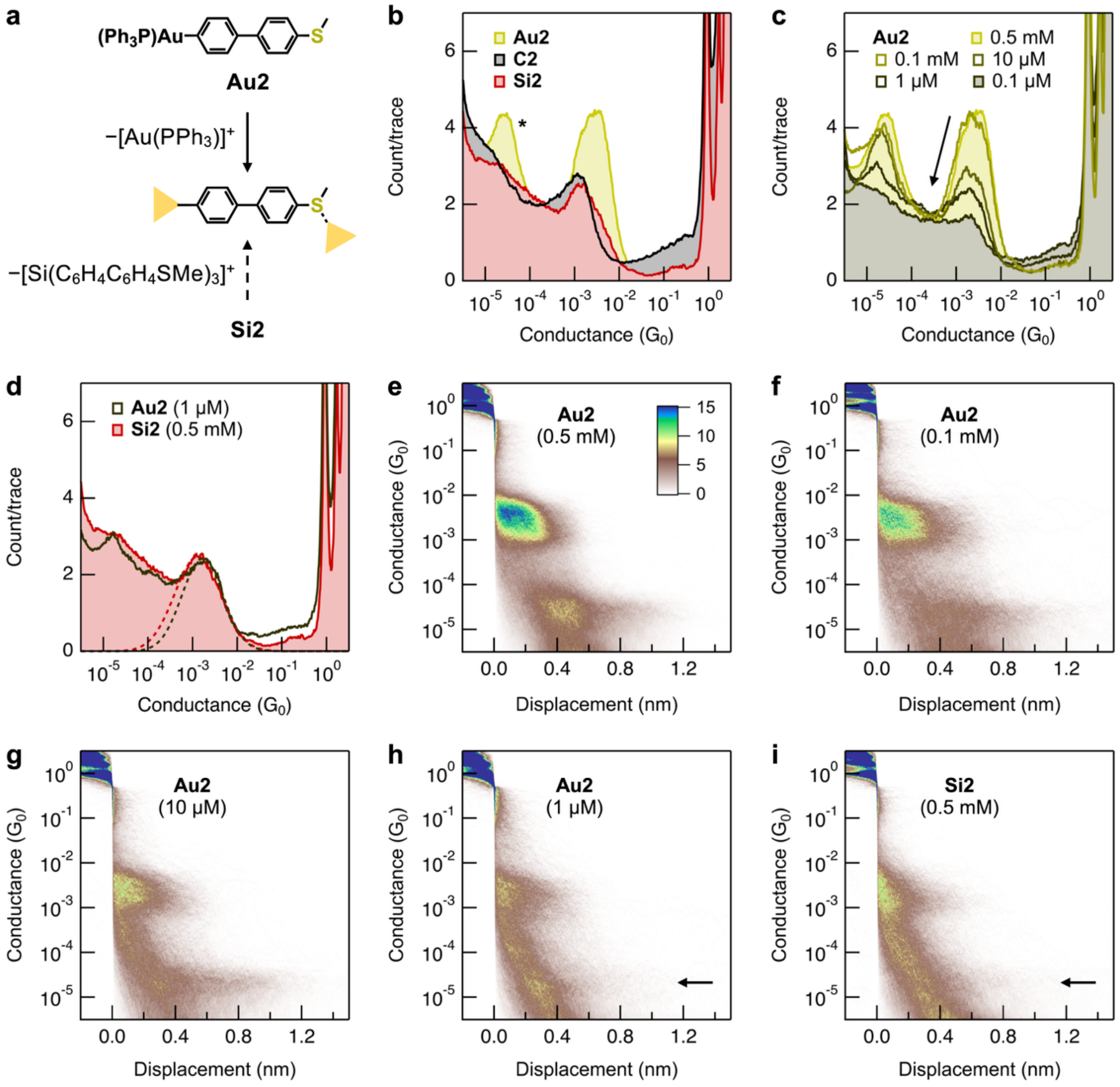

Figure S11. **(a)** Schematic illustrating ligand transmetallation in junction formation from *(top)* **Au2**, a complex containing a preinstalled Au−C(sp^2) bond, and *(bottom)* a possible ligand dissociation pathway for **Si2**. **(b)** Overlaid 1D conductance histograms from measurements of **Au2**, **C2**, and **Si2** (0.5 mM in TCB). The high conductance features observed for **C2** and **Si2** occur at conductance values ~2× lower than that of **Au2**. The starred peak is attributed to the homocoupled dimer.[7] **(c)** Additional measurements of **Au2** show that the feature near 10^{-3} G_0 shifts to lower conductance and decreases in intensity with decreasing solution concentration. **(d)** Direct comparison of histograms for **Au2** (1 μM) and **Si2** (0.5 mM). **(e-i)** Selected 2D histograms corresponding to the 1D histograms in panels (b-d). Arrows in panels (h,i) indicate a faint feature near the conductance associated with the homocoupled dimer. All measurements were performed with $V_{bias} = 100$ mV, and each histogram is constructed from 5,000-10,000 individual traces.

We next considered whether differences in conductance and intensity between these features could reflect differences in the rate at which the precursor species (**C2**, **Si2**, or **Au2**) transfers σ-aryl ligands to the gold surface. While transmetallation is known to occur readily from **Au2**, this process may be less favorable for **C2** and **Si2** (for example, due to steric constraints). Although not systematically studied in this context, the surface coverage of chemisorbed species may be expected to influence the conductance of single-molecule junctions through mechanisms similar to those reported for the solvent-dependence of conductance (e.g., changing electronic level alignment or junction geometry).[17,47–49] Similarly, analyte solution concentration has been shown to influence single-molecule conductance.[47] Accordingly, in **Figure 11c** we present overlaid 1D conductance histograms for **Au2** measured at lower concentrations, which is expected to reduce the availability of reactive species at the interface. As the concentration of **Au2** is decreased, the high conductance feature shifts from 2.5×10^{-3} G_0 to 1.7×10^{-3} G_0, and the intensity of both conductance features decreases. Notably, the intensity of the $\sim10^{-3}$ G_0 feature measured for **Au2** at 1 μM is comparable to that observed for **Si2** at 0.5 mM, and the most probable conductance values agree within a factor of 1.3. While these observations further demonstrate that the chemical environment around a single-molecule junction can influence its conductance, the high conductance features of **Si2** and **C2** remain distinct from those observed for **Au2**. A similar distinction is observed when comparing measurements of **Au2** and **Os2** in propylene carbonate (**Figure S18**). Together, these observations do not support a straightforward assignment of the high conductance features to junctions comprising dissociated linker arms.

The presence of a conductance feature between 10^{-4} and 10^{-5} G_0 in measurements of **C2**, **Si2**, or **Os2**, corresponding to the homocoupled tetraaryl dimer observed in measurements of **Au2** (**Figure 11b**, starred peak), could, in principle, be consistent with ligand dissociation pathways. While the 1D histogram of **Si2** presented in **Figure S11** does not exhibit a clearly resolved feature in this conductance range, a faint feature comparable to that observed for **Au2** at 1 μM can be discerned in the corresponding 2D histogram (arrow, **Figures 11h,i**). Similar low-intensity features in this conductance range are also observed in other measurements of **C2** and **Si2** (**Figure S8**). However, these features are weak and partially obscured by background counts arising from the dominant low-conductance features (see main discussion), limiting confidence in their assignment. For completeness, we note that the absence of a well-defined dimer feature may also be consistent with slower rates of ligand transmetallation from these compounds, as homocoupling of surface-bound σ-aryl species requires sufficiently high surface concentrations to enable C(sp^2)-C(sp^2) bond formation. Previous studies of related systems have shown that well-resolved dimer features are only observed under conditions that promote chemisorption reactions, such as elevated temperatures.[17,46] While high performance liquid chromatography experiments could, in principle, be used to detect products of any proposed *in situ* reactions,[50] they have not been performed here. If such reactions occur, the corresponding products are likely present at low concentrations, which would make their detection challenging.

<u>Hypothesis 2:</u> Alternative Junction Configurations / Aryl-π Contacts

Electrode linkers such as the thioether groups employed here are commonly used to form physical and electrical connections between single-molecules and metal electrodes. However, non-covalent interactions, including aryl-π[51–53] and electrostatic[54] contacts, have also been reported in single-molecule junctions. We therefore consider whether the high conductance features observed for **Os-*n***, **Si-*n***, and **C-*n*** could, in principle, arise from junction configurations involving aryl-π interactions (or other alternative contact motifs), which may be accessible in these systems due to the arrangement of aryl substituents around the tetrahedrally coordinated central atom. If such interactions contribute to junction formation, junctions could interconvert between a higher conductance geometry, for example, comprising one gold−thioether and one gold−aryl-π contact, and a lower conductance geometry comprising two gold−thioether contacts (the 1:1 configuration, see main discussion). This scenario is illustrated in **Figure S12c** for **Os2**. Conceptually similar single-molecule switching behavior has been demonstrated in related systems, for example, using 4,4'-bipyridine (**bipy**).[52] We note that a single high conductance peak is observed for **Si2 (−2PhSMe)** (**Figure S6**), which suggests that this feature is unlikely to arise from junctions involving multiple simultaneous thioether linker-electrode contacts (e.g., 1:2, 2:2, or 1:3 configurations; see main discussion).

In **Figure S12b** we present a 2D conductance-time histogram corresponding to push-pull measurements of **Os2**, compiled from selected individual conductance-time traces obtained using the piezo displacement ramp shown in **Figure S12a** (see *Methods* for details). This histogram shows reversible transitions between the high and low conductance features, corresponding to an on/off ratio of $>10^2$. This behavior is consistent with, but does not uniquely support, a mechanically induced change in junction configuration (**Figure S12c**). We suggest that similar switching behavior may also arise from contacting distinct components in a mixture. Such two-component mechanical conductance switching is illustrated schematically in **Figure S12d** for a possible mixture comprising intact **Os2** and dissociated linker arms concentrated at the surface (as discussed in *Hypothesis 1)*.

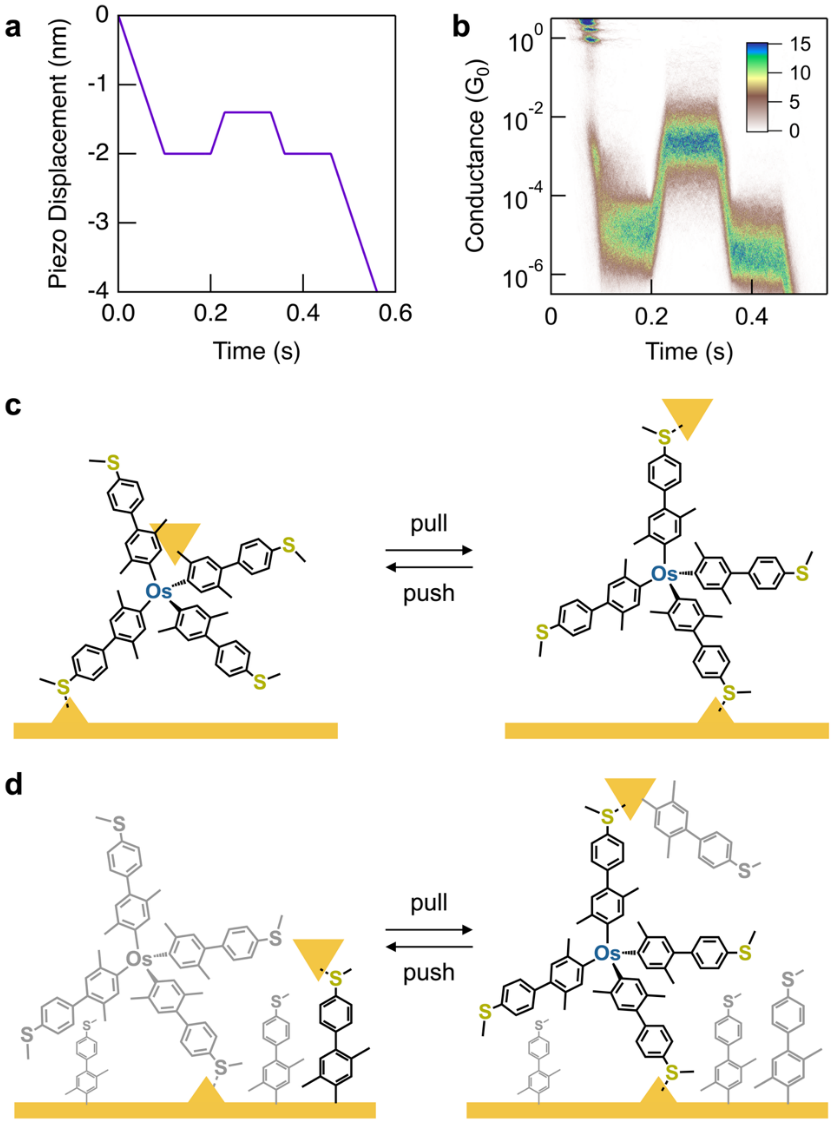

Figure S12. (a) Applied piezo displacement ramp used to obtain individual conductance-time (push-pull) traces. A push-back displacement of 0.6 nm is used, corresponding approximately to the difference in step length between the high and low conductance features of **Os2** (**Figure 3d**). **(b)** 2D conductance-time histogram generated from push-pull measurements of **Os2** in TD at V_{bias} = 750 mV, constructed from 2,663 of 11,500 traces (23%). These data show reversible transitions between low and high conductance states, corresponding to an on/off ratio >10^2. This behavior may arise from either **(c)** changes in junction configuration between high and low conductance states of the intact **Os2** complex, or **(d)** junctions that contact the intact **Os2** complex at larger electrode displacements and dissociated linker arms at shorter displacements.

To assess whether two-component mechanical switching can account for the observed behavior, we performed additional conductance measurements on a mixed solution comprising **P4SMe** (which forms longer, low-conductance junctions) and **MTh** (which forms shorter, high-conductance junctions). Molecular structures for these compounds are provided in **Figure S13a**. These components were selected to generate junctions that mimic the two distinct conductance features observed for **Os2**. We selected **MTh**, which contains a heterocyclic thioether linker with methyl groups oriented above and below the biphenyl plane, as it does not exhibit a significant secondary low-conductance feature attributable to π-stacked dimer junctions,[55] in contrast to analogous wires with less bulky thioether linkers.[10] The presence of such features would complicate interpretation of the push-pull experiments. Mixed-solution experiments were performed in 1-bromonaphthalene, as **P4SMe** is more readily soluble in this solvent than in TCB or TD.

In **Figure S13b** and **c** we present 1D and 2D conductance histograms obtained from measurements of the **P4SMe-MTh** mixture. These histograms show features comparable to those observed for **Os2** and related tetraaryl compounds, exhibiting two distinct conductance features and a transition from the high (**MTh**) to low (**P4SMe**) conductance state with increasing junction displacement. In **Figure S13d**, we present a 2D conductance-time histogram corresponding to push-pull measurements of the mixture, obtained using the same 0.6 nm displacement modulation as for **Os2**. Reversible switching between the high and low conductance features is observed, which in this case corresponds to junctions formed from different molecular components. This control experiment demonstrates that the observation of switching between high and low conductance features upon modulation of tip-substrate displacement does not, on its own, provide unambiguous evidence for the assignment of such features to distinct junction configurations of a single molecular species.

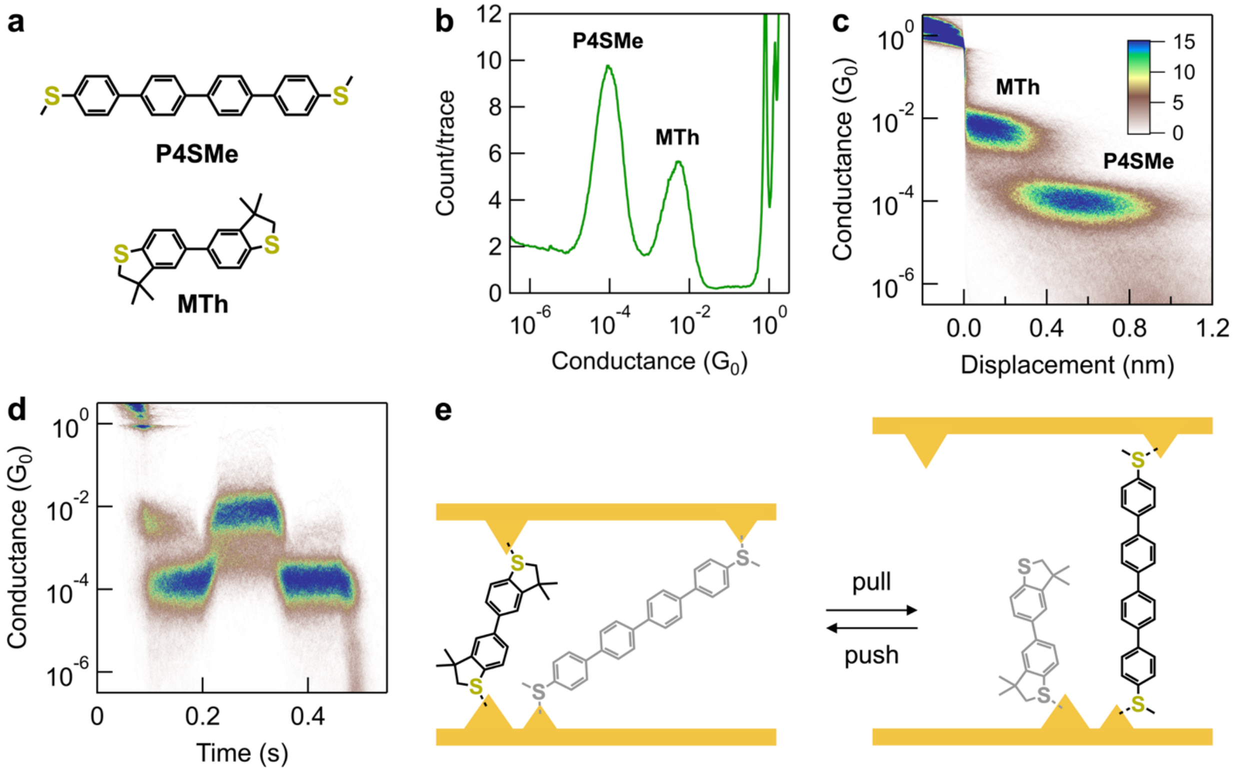

Figure S13. (a) Molecular structures of **P4SMe** and **MTh** control compounds. **(b)** 1D and **(c)** 2D conductance histograms obtained from measurements of a mixed solution comprising 0.1 mM of both **P4SMe** and **MTh** in 1-bromonaphthalene (V_{bias} = 750 mV). Two conductance features are observed, corresponding to higher conductance (**MTh**) and lower conductance (**P4SMe**) junctions, with a transition between these features occurring upon increasing tip-substrate displacement. **(d)** 2D conductance-time histogram constructed from 1,894 of 8,700 traces (22%), generated from push-pull measurements performed under the same conditions as studies of **Os2** using a 0.6 nm displacement modulation (**Figure S12**). This demonstrates reversible switching between the high and low conductance features. **(e)** Schematic illustration of a possible two-component switching mechanism, in which junction conductance is dominated by the shorter **MTh** component at smaller electrode separations and by the longer **P4SMe** component at larger separations. The relative contributions of junctions formed from species pre-absorbed on the electrodes and those assembled from solution across the electrode nanogap are not distinguished.

Mechanically induced transitions between different junction configurations of the same molecular component may be further probed by exploring the extent to which their associated conductance features are correlated. If two or more features are highly correlated (i.e., they occur frequently in the same conductance-displacement trace), this may be considered evidence for transitions between configurations of a single molecular species. To assess possible correlations between the high and low conductance features observed for the tetraaryl compounds studied here, we first examine representative conductance-displacement traces for **Os2** (**Figure S14a**), taken from the same dataset used to construct the histograms in **Figure 3**. Individual traces may exhibit exclusively high (11%) or low (22%) conductance features, but most frequently contain both features (56%). These percentages were estimated by visual inspection of a representative subset of 1,000 traces.

A more comprehensive 2D cross-correlation analysis[23] is presented in **Figure S14c,d** for **Os2** and **P4SMe-MTh** measurements (bottom panels). We focus our discussion on the off-diagonal elements of the cross-correlation map ($i \neq j$), which capture relationships between distinct conductance regions. The key observation from this analysis is that the low conductance region of the high conductance feature is negatively correlated with the high conductance region of the low conductance feature for all systems (white ovals), as previously reported and reproduced here for **bipy** junctions, the prototypical single-molecule mechanical switch (**Figure S14b**).

To verify the origin of these correlations, we construct conditional histograms (**Figure S14b-d**, *top panels*) from subsets of traces identified as containing either a high (green) or low (purple) conductance step feature.[23] Specifically, traces were selected if they contained more than the average number of data points within a conductance interval for each reference peak, defined as $\pm 1\sigma$ from the mean determined by a Gaussian fit. In all cases, the intensity of the unselected peak feature is not significantly suppressed relative to the total histogram (filled, grey), indicating that the observed correlations are associated with variations in the conductance or length of the step features, rather than the presence or absence of each feature within a given trace.

We first recapitulate the origin of the negative correlation between the two conductance features in **bipy** junctions, which provides a framework for understanding the similar correlations observed in **Os2** and **P4SMe-MTh**. In this system, the transition from the high to low conductance step occurs at different displacements across traces. When this transition occurs at shorter (longer) displacements, the high conductance feature is correspondingly shorter (longer) than average, resulting in reduced (enhanced) counts in the corresponding conductance bins. At the same time, the low conductance feature is correspondingly longer (shorter) than average, leading to enhanced (reduced) counts in its corresponding conductance bins. Together, this redistribution of counts between the two features gives rise to the observed anticorrelations.

We also observe additional correlation features for the **bipy** and **P4SMe-MTh** systems. For example, the low conductance regions of the high and low conductance features are positively correlated (red ovals), which may partly reflect the frequent co-occurrence of each step across traces. However, the localization of this correlation at the low conductance regions of each feature indicates that it is associated with correlated variations in the evolution of both features. For example, traces in which the high conductance step terminates at higher (lower) conductance may also tend to exhibit a low conductance step that terminates at higher (lower) conductance. This suggests that a common junction parameter, such as molecule-electrode coupling or contact geometry, influences the evolution of both features within a given trace. For **Os2**, this relationship cannot be resolved, as the end of the low conductance feature coincides with the instrument noise floor (**Figure S14c**).

Furthermore, we observe off-diagonal negative correlations located near the diagonal at the peak positions (gold ovals). These are consistent with the presence of plateau features that occur at different average conductance values from trace to trace, which combine in the 1D histogram to give a single peak, as previously demonstrated using model data.[23] In this case, bins that capture the plateau in individual traces exhibit higher-than-average counts, while neighboring bins outside this region exhibit lower-than-average counts, giving rise to the observed negative correlations in the covariance map. Such features are more prominent for sloped plateau features. For **bipy**, this behavior is partially obscured, as the off-diagonal negative correlations associated with the low conductance peak coincide with positive correlations between the low conductance regions of the two features, resulting in an overall positive correlation. In both **bipy** and **Os2** the off-diagonal negative correlations from the high conductance peak are not well resolved from the broader inter-feature region of negative correlation.

Consistent with the push-pull experiments described above, these results demonstrate that correlation analyses of different conductance features do not, on their own, provide unambiguous evidence that these originate from different conformations of the same molecular component within a single-molecule junction.

Summary

Taken together, these studies highlight different plausible origins for the high conductance features observed in these systems. While each hypothesis can account for certain aspects of the data, no single junction geometry can be uniquely identified based on the available experimental evidence. We therefore refrain from assigning a definitive junction geometry for these features, and instead emphasize their reproducibility and general characteristics, which are discussed in the main text.

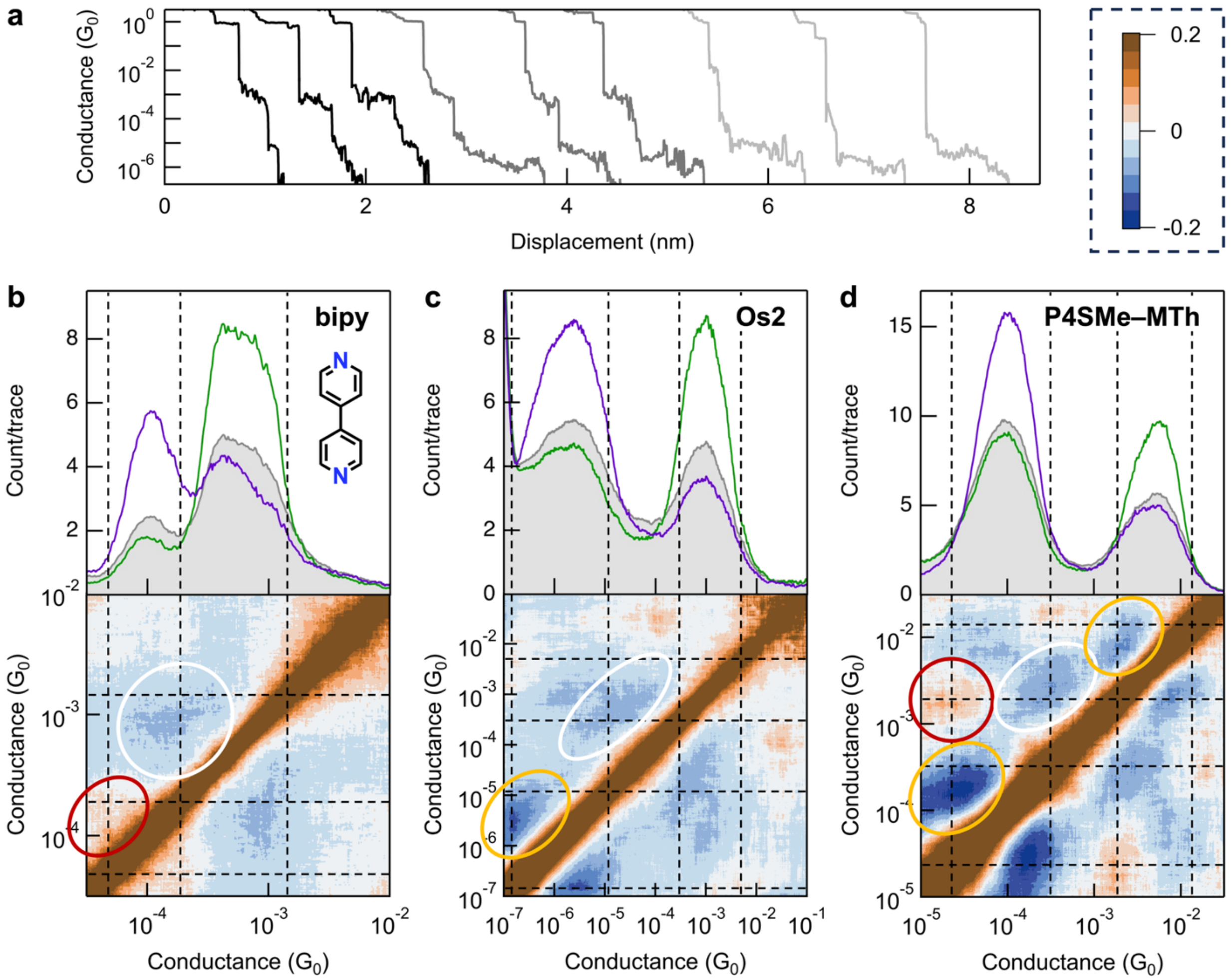

Figure S14. (a) Representative conductance-displacement traces for **Os2** measured in TD, showing (*left*, black) high conductance features without pronounced low conductance plateaus, (*middle*, dark grey) traces exhibiting high and low conductance features, and (*right*, light grey) low conductance features only. Traces are offset along the displacement axis for clarity. **(b-d)** Cross-correlation analysis for measurements of **bipy** (molecular structure inset), **Os2**, and a mixed solution of **P4SMe–MTh**. Top panels show total 1D histograms (filled, grey) overlaid with conditional histograms selected for low (purple) or high (green) conductance peaks. Bottom panels show 2D correlation histograms, overlaid with dotted lines defining distinct conductance regions and ovals highlighting specific correlation features (see associated discussion in the Supporting Information). *Inset (top right):* color scale for the 2D correlation histograms. The 1D and 2D histograms for this **bipy** dataset were previously published in ref [17], and the datasets for **Os2** and **P4SMe–MTh** correspond to those used in **Figure 3a** and **Figure S13b**.

Additional Measurements in Propylene Carbonate

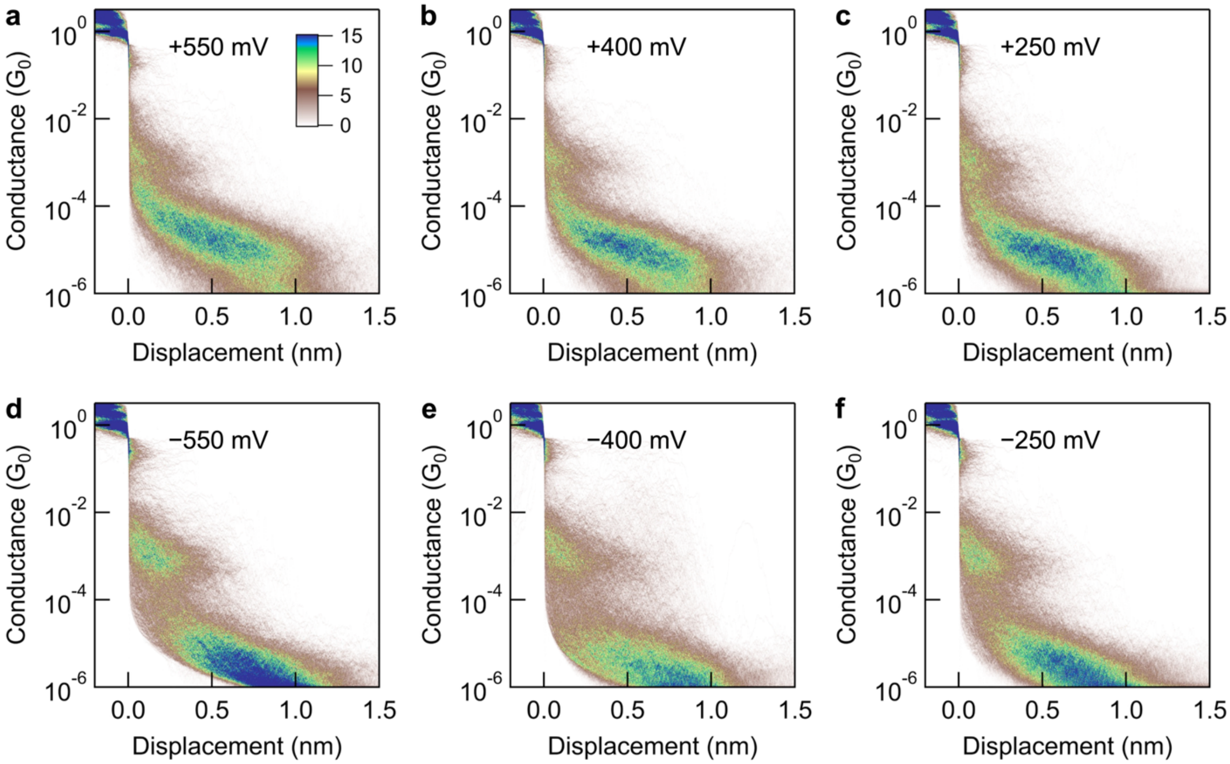

Figure S15. 2D histograms corresponding to the 1D histograms shown in **Figure 4a**.

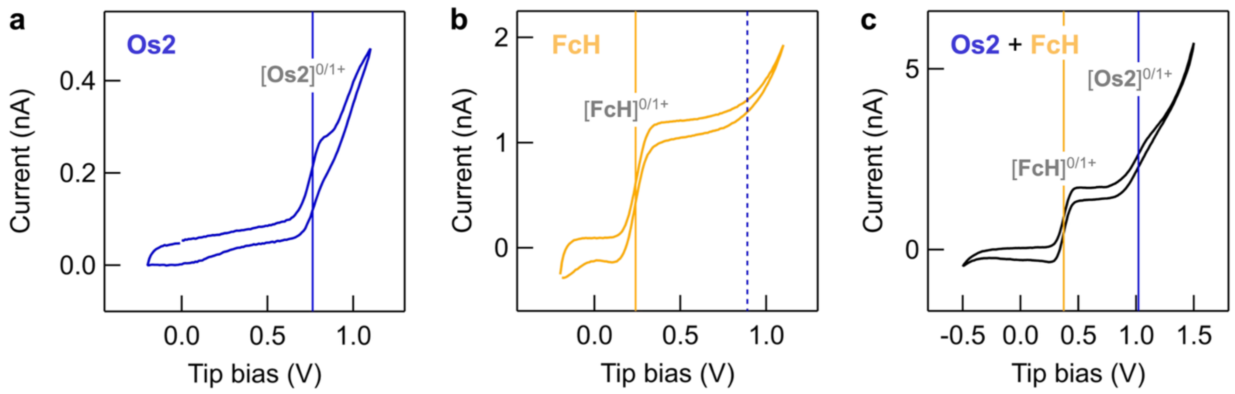

Figure S16. Cyclic voltammograms obtained in PC with no added electrolyte for ~0.5 mM solutions of **(a) Os2** (reproduced from **Figure 4f** for convenience), **(b)** ferrocene (**FcH**), and **(c)** a mixture of **Os2** and **FcH** in a 1:1 molar ratio. Solid vertical lines denote the approximate mid-point potentials ($E_{1/2}$) of the observed redox features.[56] The feature observed near the oxidative solvent limit in solutions containing **Os2** is assigned to the 0/1+ couple characteristic of this complex, at approximately +0.65 V vs. [**FcH**]$^{0/1+}$ under these conditions. This assignment is supported by the absence of this feature in panel (b); the dashed line indicates the corresponding $E_{1/2}$ for **Os2** referenced to [**FcH**]$^{0/1+}$, confirming that it does not arise from an adventitious electroactive contaminant. Voltammograms were obtained with a wax-coated gold STM tip as the working ultramicroelectrode, and a gold-on-steel substrate serving as both counter and quasi-reference electrode (two-electrode configuration), with an external potentiostat. As such, the reported values correspond to the applied tip-substrate bias rather than absolute electrochemical potentials. Comparable redox features (within the uncertainty associated with quasi-reference potential drift) were observed when sweeping the tip-substrate bias using the STM-BJ electronics and monitoring the tip current. Variations in measured current across voltammograms are attributed in part to differences in wax-coated STM tip geometry and effective electrode area.

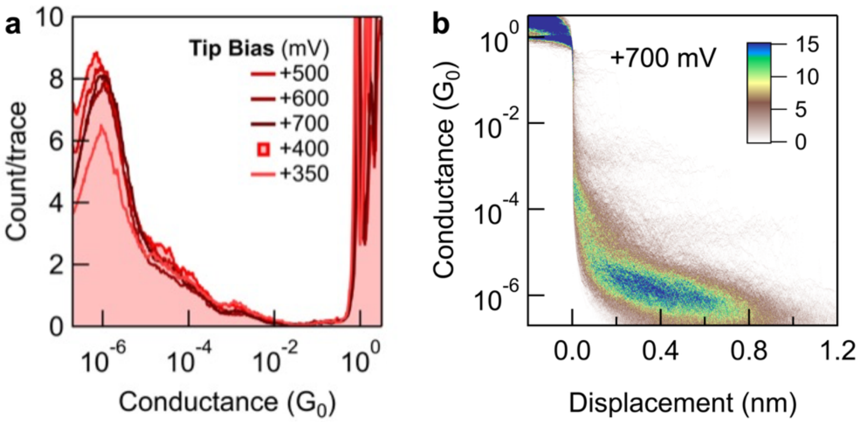

Figure S17. (a) Overlaid 1D histograms for **Si2** measured in propylene carbonate at different V$_{bias}$ (~2,000 traces; biases listed in order of measurement). Much smaller conductance changes are observed compared to analogous measurements for **Os2** (**Figure 4c**). No significant high conductance feature is observed. **(b)** A representative 2D histogram corresponding to the 1D histogram in panel (a) obtained at tip bias = +700 mV.

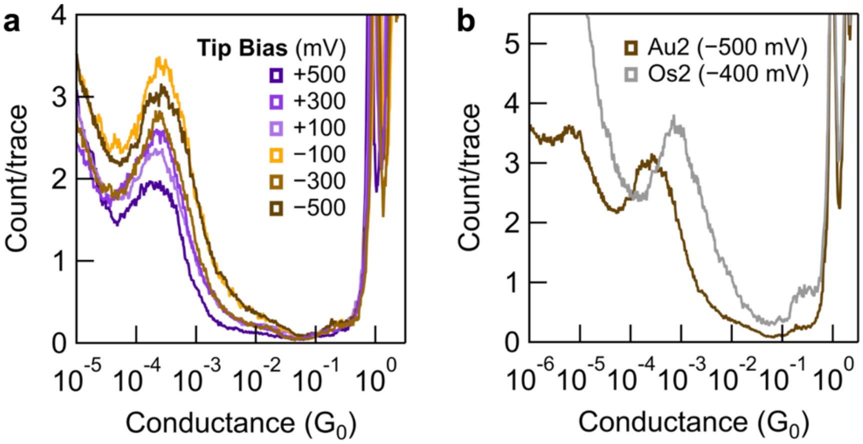

Figure S18. Measurements of **Au2** in PC for comparison with the high conductance features observed for **Os2** (see *Analysis of High Conductance Features*, *Hypothesis 1*). **(a)** Overlaid 1D histograms for **Au2** measured in PC at different tip biases (≥2,000 traces; biases measured non-consecutively). The dominant peak feature is consistent with junctions comprising Au–biphenyl–S(Me)–Au geometries (**Figure S11a**). The conductance of this feature shows minimal dependance on tip bias, while its intensity is lower at positive compared to negative tip biases. Similar trends are observed for the high conductance feature of **Os2** measured in PC (**Figure 4**). **(b)** Overlaid 1D histograms for **Au2** and **Os2** measured in PC at comparable negative tip biases, focused on the high conductance region. Under these conditions, the feature observed for **Os2** (7.2×10^{-4} G$_0$) occurs at a conductance approximately ~3× higher than that of **Au2** (2.4×10^{-4} G$_0$). Data for **Os2** are reproduced here from **Figure 4a**.

7. Additional Computational Data

Geometric Analysis

We note that the aryl groups of oligoaryl wires with tetrahedral osmium(IV), silane, or methane centers exhibit different geometric relationships to one another in the frozen geometries observed in molecular structures obtained from single-crystal X-ray crystallography or computational experiments. The relationship between two aryl substituents can be defined using two dihedral angles (which we label α and β), as shown in **Figure S19**. Note that the specific α or β labels have no associated special meaning and are interchangeable within a given dihedral angle pair.

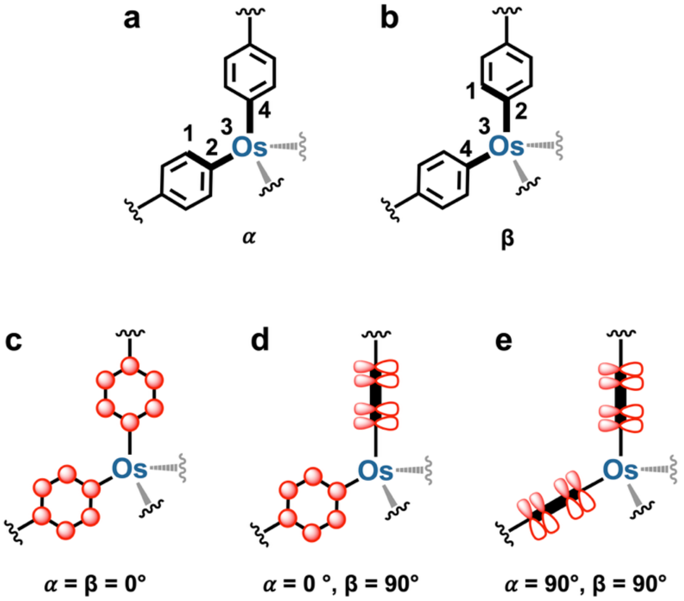

$\alpha = \beta = 0°$

$\alpha = 0°, \beta = 90°$

$\alpha = 90°, \beta = 90°$

Figure S19. (a,b) The relative orientation of adjacent aryl ligands can be defined using two different dihedral angles, α and β. We define these angles using atoms 1-4, connected in each schematic through bonds with bold linewidths. In each case, atom 1 was chosen as the aryl carbon atom closest to the bond defined by atoms 3 and 4. **(c-e)** Illustrations of different aryl-aryl orientations, highlighting how they may influence overlap/coupling between each aryl π-system, at selected values of α and β.

All tetraaryl compounds comprise, by definition, four aryl groups we can label as *i*, *ii*, *iii*, and *iv*. These can be paired in six unique combinations – *i-ii*, *i-iii*, *i-iv*, *ii-iii*, *ii-iv*, and *iii-iv* – as illustrated in **Figure S20**. As such, any given compound has six pairs of dihedral angles (α and β; 12 angles total).

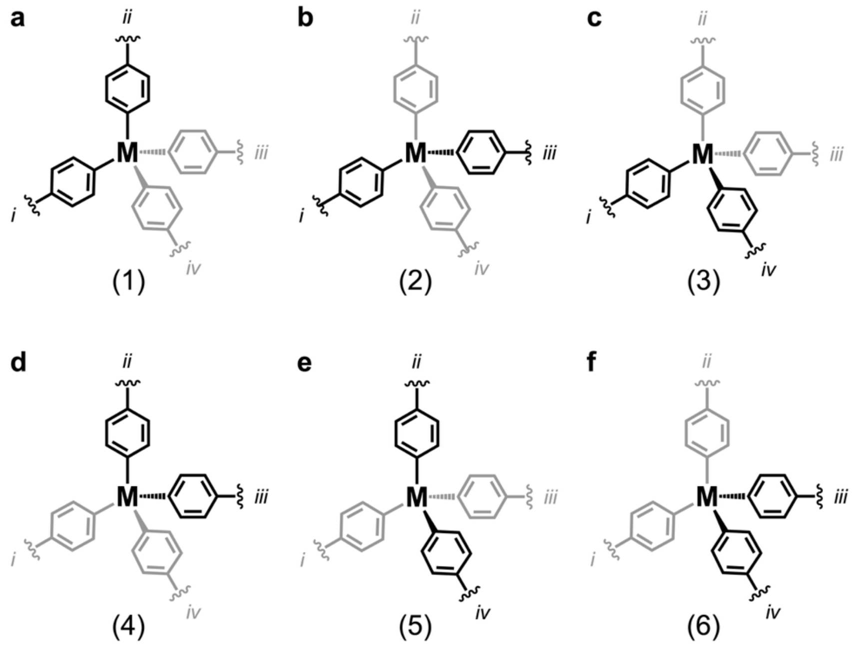

Figure S20. All tetraaryl compounds exhibit six pairs of dihedral angles, α and β (as defined in **Figure S19**). Each pair of angles is associated with one of the six unique combinations of aryl ligands – **(a)** *i-ii*, **(b)** *i-iii*, **(c)** *i-iv*, **(d)** *ii-iii*, **(e)** *ii-iv*, and **(f)** *iii-iv* – illustrated schematically here.

In **Table S5** we present calculated sets of dihedral angle pairs for a self-consistent series of tetra(ferrocenylphenyl) compounds comprising Os(IV) (**Os-Fc**), C (**C-Fc**), or Si (**Si-Fc**) centers, structurally characterized through single-crystal X-ray diffraction.[4] In **Table S6** we also present sets of dihedral angle pairs calculated for parent compounds with the ferrocenyl substituents removed, after optimizing their geometry using computational methods (Q-Chem). For each compound analyzed, we find that two dihedral pairs are *similar* ($\alpha \approx \beta$) and four are *different* ($\alpha \not\approx \beta$); denoted with black or blue text in the tables, respectively. Notably, the geometry where the angles are *different* approximates the one shown in **Figure S19d**, in which one angle is typically larger than |61°| and the other smaller than |28°|. For geometries where the angles are similar, both angles lie between |36°| and |58°|.

Table S5. Dihedral angles defining relative aryl ligand orientation in model tetraaryl compounds.[a]

	dihedral angle pair											
	1		2		3		4		5		6	
Os-Fc	−19.57	76.22	−42.26	−42.26	19.57	−76.22	42.26	42.26	76.22	−19.57	19.57	−76.22
Si-Fc	−64.54	28.21	54.58	54.58	−0.34	85.00	−36.86	−36.86	−0.34	85.00	28.21	−64.54
C-Fc	−0.57	−71.47	66.61	−5.19	−53.94	−48.28	50.45	51.60	72.91	−5.16	−69.71	6.51

[a] All values in degrees, obtained from a self-consistent set of X-ray crystal structures of ferrocene-appended tetraaryl complexes.[4] Blue angles = *different* dihedral angles in the pair, black = *similar* dihedral angles.

Table S6. Dihedral angles defining relative aryl ligand orientation in tetraaryl compounds after geometry optimization (Q-Chem).[a]

	dihedral angle pair											
	1		2		3		4		5		6	
$Os(C_8H_9)_4$	−57.16	−58.43	62.73	2.33	−61.72	−0.74	58.02	57.18	65.22	1.36	−1.31	−64.63
$Si(C_8H_9)_4$[b]	−49.93	−50.40	70.03	−7.62	−70.26	6.94	50.08	51.01	70.03	−6.31	7.22	−69.60
$Si(C_6H_5)_4$	−37.84	−37.84	82.28	−24.51	−82.28	24.51	37.84	37.84	82.28	−24.51	24.51	−82.28
$Si(C_8H_9)_4$[c]	−50.28	−50.28	70.19	−5.79	−70.08	5.73	50.54	50.54	70.19	−5.79	5.73	−70.84
$C(C_6H_5)_4$	64.75	1.52	−64.75	−1.52	−56.67	−56.67	−1.52	−64.75	56.67	56.67	64.75	1.52

[a] All values in degrees, obtained following geometry optimization of parent compounds (unfunctionalized aryl ligands), from starting geometries based on X-ray crystal structures obtained by different groups,[2,25,26] using PBE. Here both $Si(C_6H_5)_4$ and $C(C_6H_5)_4$ were optimized with S_4 symmetry, $Si(C_8H_9)_4$ (from the $Si(C_6H_5)_4$ starting geometry, green shaded entry) was optimized with C_2 symmetry. Ligands: C_6H_5 = phenyl; C_8H_9 = 2,5-xylyl. Blue angles = *different* dihedral angles in the pair, black = *similar* dihedral angles. [b] The optimized geometry of $Si(C_8H_9)_4$ (red shaded entry) was obtained from an input structure based on the optimized geometry of $Os(C_8H_9)_4$, after replacing the osmium atom for a silicon atom and adjusting all Si-aryl bonds to 1.9 Å. To facilitate the clearest comparison, the same aryl groups in $Os(C_8H_9)_4$ and $Si(C_8H_9)_4$ were used to calculate each of the dihedral angle pairs 1-6. [c] The optimized geometry of $Si(C_8H_9)_4$ (green shaded entry) was obtained from an input structure based on the optimized geometry of $Si(C_6H_5)_4$, after replacing selected aryl−H substituents for $-CH_3$. Similar dihedral angle pairs are obtained for $Si(C_8H_9)_4$ structures after geometry optimization from different input structures (shaded entries).

Significant differences in dihedral angle pairs are observed when reoptimizing the geometry of $Si(C_6H_5)_4$ after addition of $-CH_3$ groups to the 2- and 5-positions of the aryl rings to form $Si(C_8H_9)_4$ (**Table S6**, shaded entries). As changes in the equilibrium geometries and dihedral angle pairs of these species are expected to influence junction conductance (see discussion below), we note that in the present study we strictly compare the properties of compounds having Os−2,5-xylyl, Si−phenyl, and C−phenyl central fragments, rather than probing the influence of the tetrahedrally-coordinated central atoms alone.

In the ***Tunnel Coupling*** *(Q-Chem)* section below, we perform model calculations of wires connected to single gold atoms to help evaluate the extent to which these different classes of angle pairs – *similar* or *different* – influence electronic coupling between the π-systems of the associated aryl groups. In the ***Additional Quantum Transport Calculations Data*** *(FHI-aims)* section, we further evaluate how these aryl-aryl dihedral angle pairs modulate the calculated through-molecule transmission in wires connected to extended gold electrodes. These analyses reveal specific challenges associated with applying frozen geometries to calculate conductance trends for these systems.

Tunnel Coupling (Q-Chem)

We explored the properties of two sets of each model complex, **Os1h**, **Si1h**, and **C1h**. One set exhibited a pair of aryl substituents that had *similar* pairs of dihedral angles, and the other set had angles pairs that were *different* (see *Geometric Analysis*, above). The process of constructing each model essentially involved adding two −SMe groups on different aryl substituents of the parent complex. In **Table S7** and **Table S8**, we present selected computational data for these model compounds obtained using the PBE and B3LYP functionals, respectively, both before and after adding Au_1 clusters.

We find that the HOMO-LUMO gap of each molecular complex does not strongly depend on whether the dihedral angle pair chosen is *similar* or *different*. This is rationalized given that this gap is a property of the entire molecule, and that the addition of −SMe substituents to different aryl rings of each molecule simply generates geometric isomers with very similar electronic structures. Here we observe the same trends in HOMO-LUMO gap as found using FHI-aims (**Table S9**). The gaps are always smaller for **Os1h** than for **Si1h**/**C1h**, and the gaps are larger for all models when using the B3LYP functional compared to PBE. Example isosurface plots for the frontier orbitals of each model are presented in **Figure S21,22**.

We use these models, now connected to Au_1 clusters through the sulfur atom of their −SMe substituents, to explore changes in their calculated tunnel couplings, 2t. The square of this quantity has been found to be proportional to the molecular junction conductance.[29,57] In agreement with our experimental conductance measurements for **Os2** and **Si2** in PC, and with the results of quantum transport calculations (below), we find the tunnel coupling for **Os1h**-Au_1 is consistently larger than for **Si1h**-Au_1 or **C1h**-Au_1 (**Table S7, S8**). Notably, this difference is maximized when using the PBE functional, and tunnel couplings calculated using PBE are also more variable between models with *similar* or *different* dihedral angle pairs, relative to those with B3LYP. Representative isosurface plots for the tunnel coupled orbitals of **Os1h**-Au_1 are provided in **Figure S23**. The differences in tunnel coupling observed for non-equivalent geometries in these simple models can be reproduced for **Os1h**, **Si1h**, and **C1h** in transmission calculations using the same molecular structures connected between larger gold electrodes (**Figure S27**).

Table S7. Selected computational data for **Os1h**, **Si1h**, **C1h** models using the PBE functional.[a]

	s/d [b]	α (°) [c]	β (°) [c]	HOMO (eV)	LUMO (eV)	gap (eV) [d]	$4t^2$ (eV^2)
Os1h	s	54.9	57.1	−3.817	−2.222	1.595	-
	d	−64.2	−0.3	−3.813	−2.242	1.571	-
Si1h	s	−38.5	−38.5	−4.867	−1.271	3.596	-
	d	−83.7	25.8	−4.857	−1.276	3.581	-
C1h	s	59.3	59.3	−4.642	−1.144	3.498	-
	d	−72.9	9.4	−4.770	−1.284	3.487	-
Os1h-Au$_1$	s	49.5	50.6	−3.854	−3.741	-	1.3×10^{-2}
	d	−60.8	−4.0	−3.845	−3.728	-	1.4×10^{-2}
Si1h-Au$_1$	s	−47.1	−39.5	−3.971	−3.964	-	4.5×10^{-5}
	d	−80.1	39.4	−3.972	−3.949	-	5.3×10^{-4}
C1h-Au$_1$	s	64.8	64.0	−3.976	−3.903	-	5.4×10^{-3}
	d	−75.9	12.6	−3.943	−3.933	-	9.3×10^{-5}

[a] Calculations performed as described in *Computational Details*. [b] Here, s/d = similar or different dihedral angles for the selected pair of aryls functionalized with −SMe groups. [c] Dihedral angles after geometry optimization. Note the same input geometry for each series (the parent molecule with appended −SMe groups, without Au$_1$ clusters) was used in the calculations here using PBE and those in **Table S8** using B3LYP. [d] Where gap = LUMO – HOMO.

Table S8. Selected computational data for **Os1h**, **Si1h**, **C1h** models using the B3LYP functional.[a]

	s/d [b]	α (°) [c]	β (°) [c]	HOMO (eV)	LUMO (eV)	gap (eV) [d]	$4t^2$ (eV^2)
Os1h	s	56.7	56.2	−4.615	−1.675	2.940	-
	d	−64.8	0.5	−4.617	−1.692	2.925	-
Si1h	s	−38.8	−38.8	−5.641	−0.543	5.098	-
	d	−83.0	24.3	−5.629	−0.546	5.083	-
C1h	s	57.9	57.9	−5.404	−0.407	4.998	-
	d	−71.5	8.2	−5.542	−0.532	5.010	-
Os1h-Au$_1$	s	55.5	57.0	−4.064	−3.776	-	8.3×10^{-2}
	d	−55.5	−10.7	−4.090	−3.756	-	1.1×10^{-1}
Si1h-Au$_1$	s	−36.8	−37.0	−4.123	−3.895	-	5.2×10^{-2}
	d	−80.0	29.2	−4.166	−3.933	-	5.4×10^{-2}
C1h-Au$_1$	s	67.8	70.1	−4.174	−3.882	-	8.5×10^{-2}
	d	−74.7	13.0	−4.141	−3.909	-	5.4×10^{-2}

[a] Calculations performed as described in *Computational Details*. [b] Here, s/d = similar or different dihedral angles for the selected pair of aryls functionalized with −SMe groups. [c] Dihedral angles after geometry optimization. Note the same input geometry for each series (the parent molecule with appended −SMe groups, without Au$_1$ clusters) was used in the calculations here using B3LYP and those in **Table S7** using PBE. [d] Where gap = LUMO – HOMO.

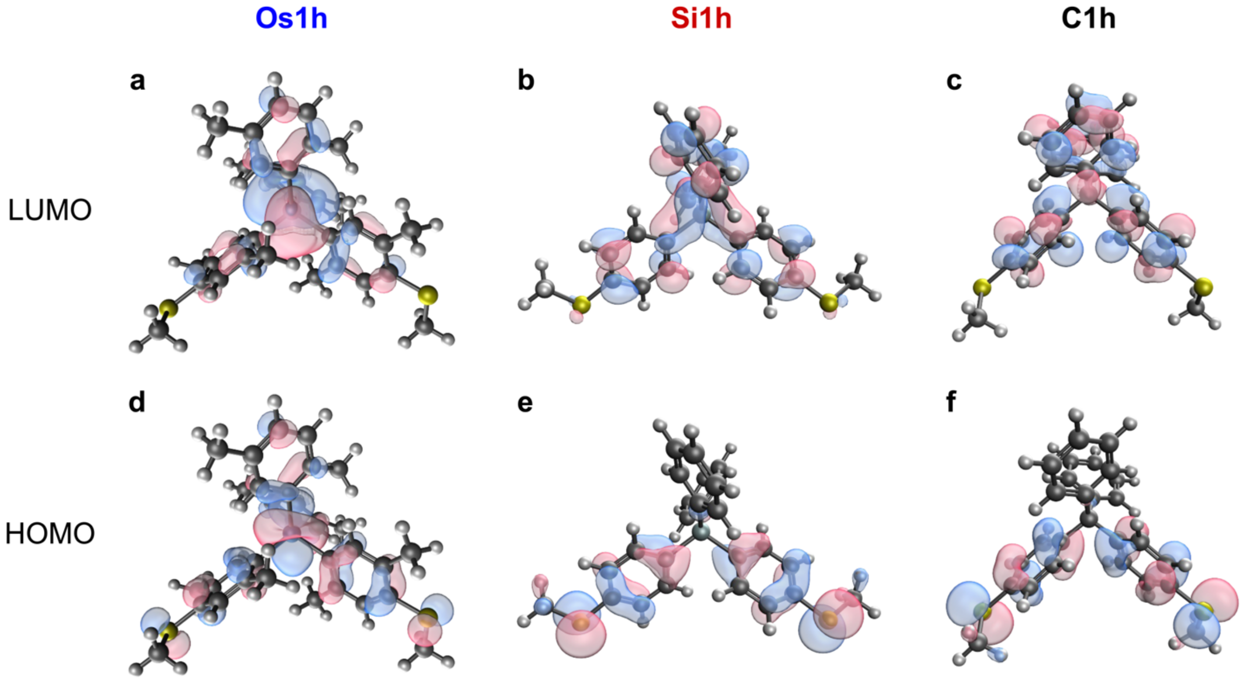

Figure S21. Isosurface plots of the **(a-c)** HOMO and **(d-e)** LUMO obtained from DFT calculations using B3LYP for gas phase **Os1**, **Si1**, and **C1** models (**Os1h**, **Si1h**, **C1h**, respectively; isovalue = 0.08 Å^{-3}; geometries correspond to those having similar dihedral angles for the selected pair of aryls functionalized with −SMe groups). In each case, the HOMOs exhibit significant orbital density on the sulfur linkers, where the LUMOs do not, indicating these compounds should function as HOMO conductors. In **Os1h** there is a greater orbital density on the central atom (in this case, comprising an Os d_{z2} orbital rather than a C or Si sp^3 hybrid orbital). These plots corroborate the trends observed in the calculated transmission functions (**Figure 5b**) and suggest the increased conductance of **Os-*n*** relative to **Si-*n*** or **C-*n*** results from the extended delocalization of the thioanisole linker π-system across the central atom in the HOMO.

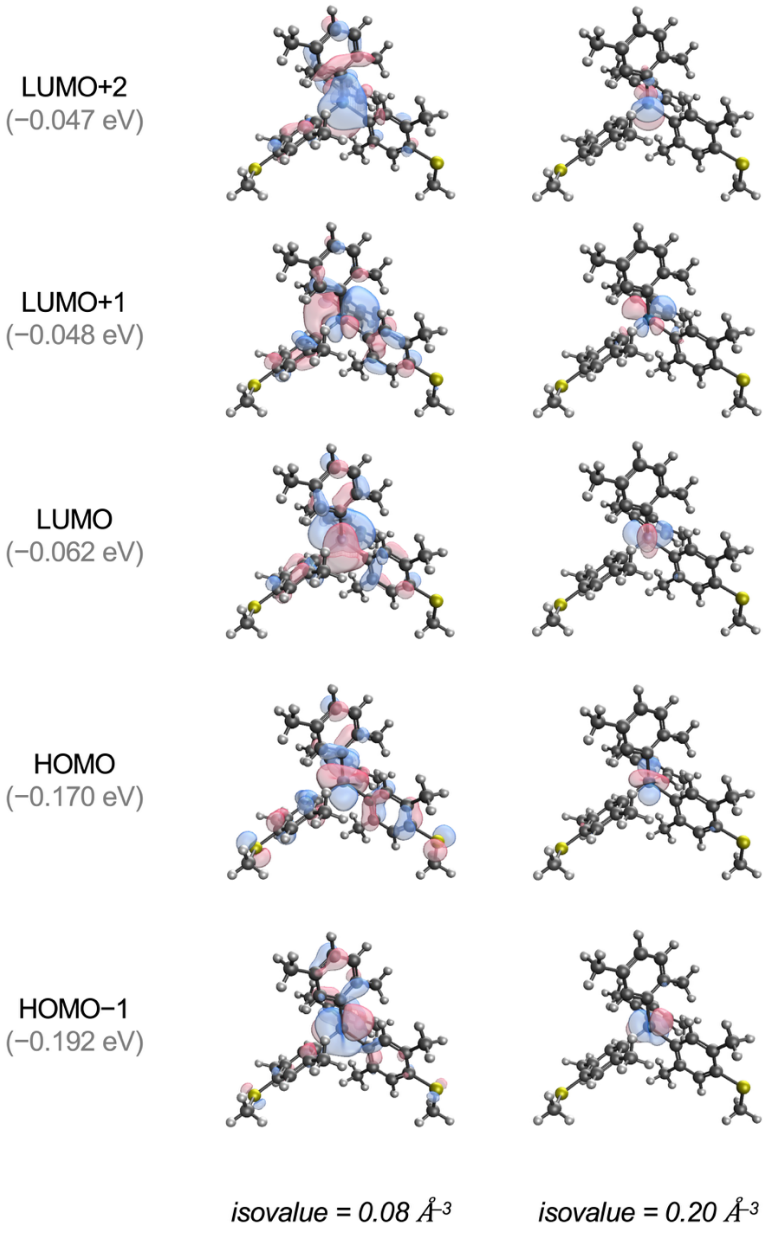

Figure S22. *Left:* Isosurface plots of an extended set of gas phase frontier orbitals for **Os1h** obtained from DFT calculations using B3LYP (isovalue = 0.08 Å^{-3}; geometries correspond to those having similar dihedral angles for the selected pair of aryls functionalized with −SMe groups). HOMO and LUMO are reproduced from **Figure S21** for convenience. *Right:* The same isosurface plots calculated using isovalue = 0.20 Å^{-3} to help assign the *d*-orbital component of each molecular orbital. These results agree well with the expected electronic structure of such low spin d^4 tetrahedral complexes, comprising frontier orbital sets of *e* (HOMO−1, HOMO) and t_2 (LUMO, LUMO+1, LUMO+2) symmetry.[58] Here, however, HOMO−1 (d_{x2-y2} character) and HOMO (d_{z2}) are non-degenerate, and the LUMO (d_{xy}) lies at a lower energy than LUMO+1 and LUMO+2 (d_{xz}, d_{yz}). We attribute the broken degeneracy of each set to the distorted coordination environment,[5] and the asymmetric ligand field of this heteroleptic model complex.

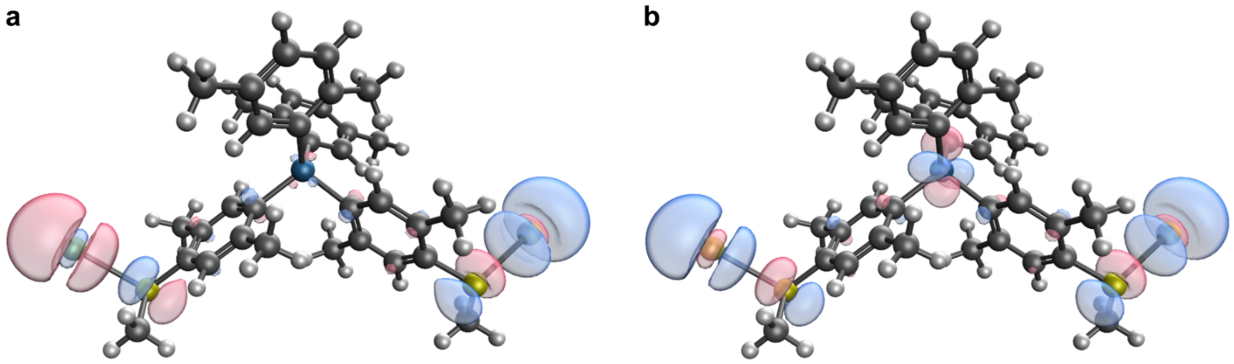

Figure S23. Isosurface plots of the **(a)** HOMO (antisymmetric) and **(b)** LUMO (symmetric) frontier orbitals obtained from DFT calculations using B3LYP for a **Os1** model (**Os1h**) bound to Au_1 clusters (isovalue = 0.08 Å^{-3}; geometries correspond to those having similar dihedral angles for the selected pair of aryls functionalized with −SMe groups). These orbital plots are consistent with those observed in previous reports,[10,57] and illustrate how the Au s orbitals are tunnel coupled through the tetrahedral bridge.

Additional Quantum Transport Calculations Data (FHI-aims)

Table S9. HOMO-LUMO gaps (in eV) for the **Os-*n***, **Si-*n***, and **C-*n*** molecular series, calculated using the PBE and B3LYP functionals. We employed the same DFT computational parameters as described in *Section: General Information* of the **SI**. These computational parameters converge the HOMO-LUMO gaps within a window of 20 meV.

compound	PBE (eV)	B3LYP (eV)
Os1	1.560	2.862
Os2	1.660	2.963
Os3	1.723	3.044
Si1	3.400	4.808
Si2	2.948	4.269
Si3	2.740	4.021
C1	3.246	4.660
C2	2.985	4.301
C3	2.761	4.038

Table S10. Kohn-Sham energies of the HOMO and LUMO states (in eV) for the **Os-*n***, **Si-*n***, and **C-*n*** molecular series, calculated using the PBE and B3LYP functionals. We employed the same DFT computational parameters as described in *Section: General Information* of the SI.

compound	PBE (eV)		B3LYP (eV)	
	HOMO	LUMO	HOMO	LUMO
Os1	-4.074	-2.513	-4.869	-2.006
Os2	-4.250	-2.590	-5.027	-2.067
Os3	-4.341	-2.617	-5.118	-2.073
Si1	-5.042	-1.642	-5.858	-1.049
Si2	-4.979	-2.031	-5.734	-1.465
Si3	-4.974	-2.235	-5.699	-1.679
C1	-4.899	-1.653	5.702	-1.042
C2	-4.918	-1.933	-5.659	-1.358
C3	-4.948	-2.187	-5.665	-1.627

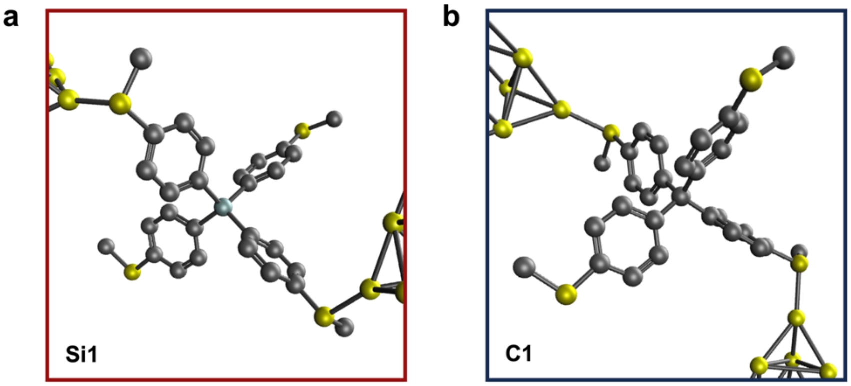

Figure S24. Additional representative junction geometries for **(a) Si1** and **(b) C1**. Hydrogen atoms excluded for clarity.

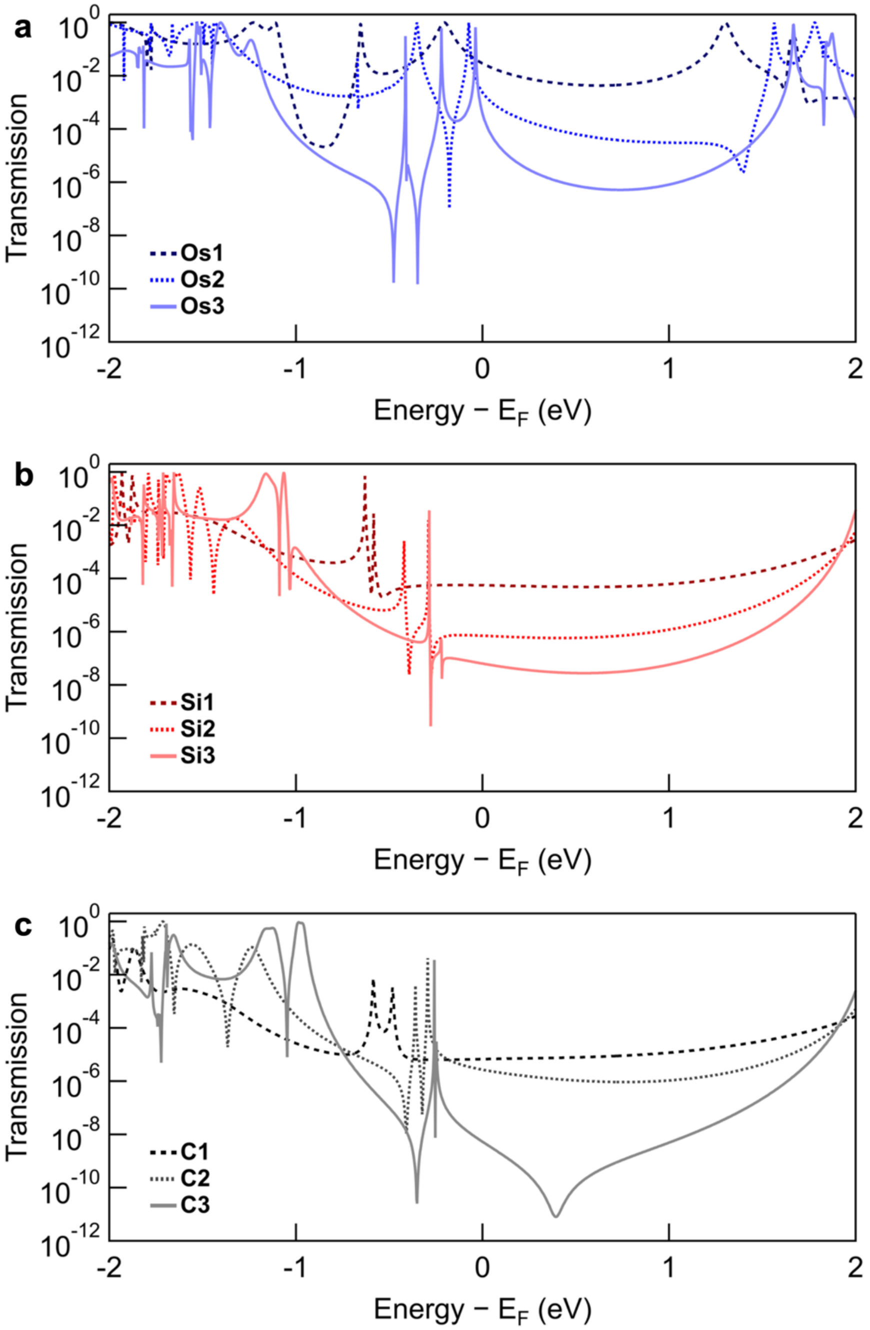

Figure S25. Overlaid calculated transmission functions for **(a) Os-*n***, **(b) Si-*n***, and **(c) C-*n***. Data for **Os-*n***, **Si2**, and **C2** are reproduced here from **Figure 5**, shown in an expanded format for clarity.

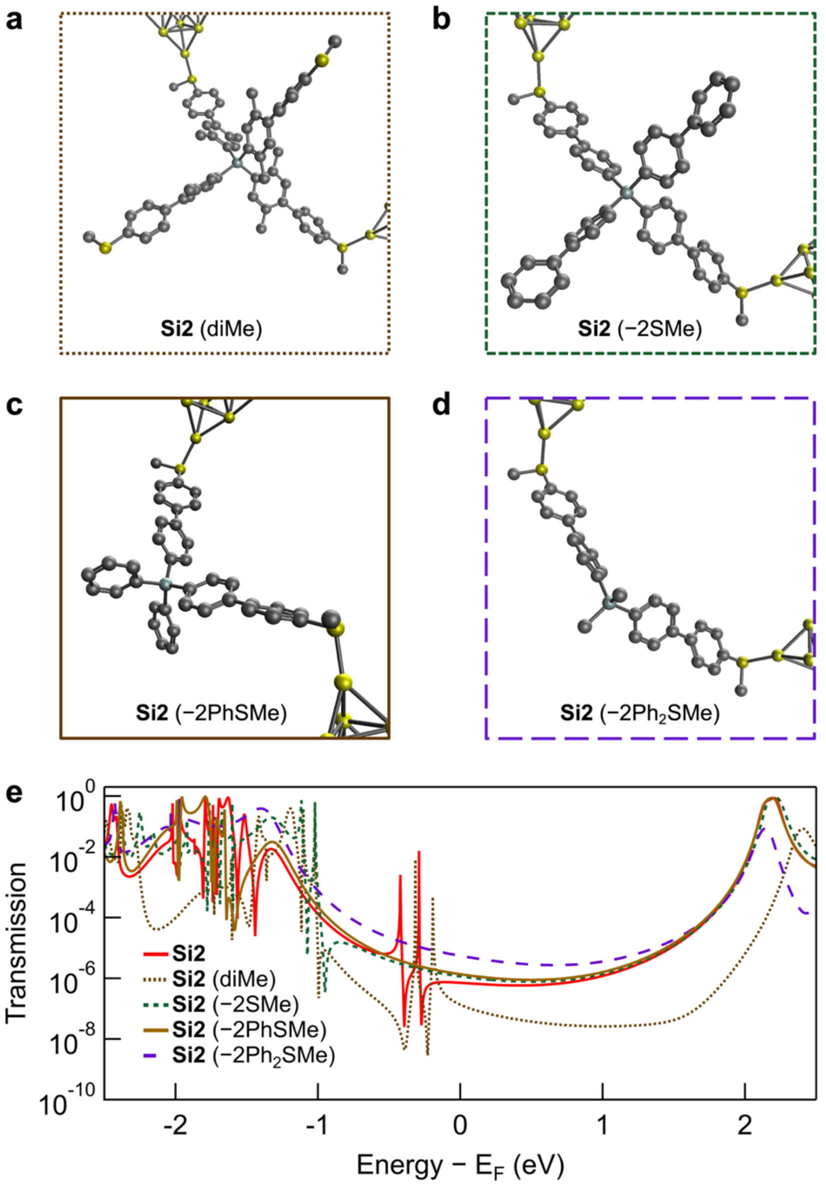

Figure S26. Junction geometries for: **(a) Si2** (diMe), formed by adding −CH_3 groups in the 2- and 5-positions of each aryl connected to the silicon center of **Si2**; **(b) Si2** (−2SMe), **(c) Si2** (−2PhSMe), and **(d) Si2** (−$2Ph_2SMe$), formed by removing thioether groups from unbound linker arms, replacing the unbound arms of **Si2** with −Ph (−C_6H_5) groups, or replacing the unbound arms of **Si2** with −CH_3 groups, respectively. Hydrogen atoms excluded for clarity. Input structures from geometry optimization were constructed from the **Si2** junction shown in **Figure 5d**, to ensure the gold electrodes were connected to the same thioether linkers in each case. **(e)** Overlaid transmission functions for the junctions shown in panels a-d, and **Si2** (shown in **Figure 5d**). The data for **Si2** (−2SMe), **Si2** (−2PhSMe), and **Si2** (−$2Ph_2SMe$) junctions exhibit energetically shifted or completely absent Fano-type resonances, respectively. The transmission function for **diMe** junctions deviates most significantly from that of the parent **Si2** junction. Here, the electron-donating and bulky −CH_3 groups shift the LUMO resonance at ~2 eV to higher energy, also modulating the relative orientation/coupling between Si-connected aryl rings **(Table S6)**.

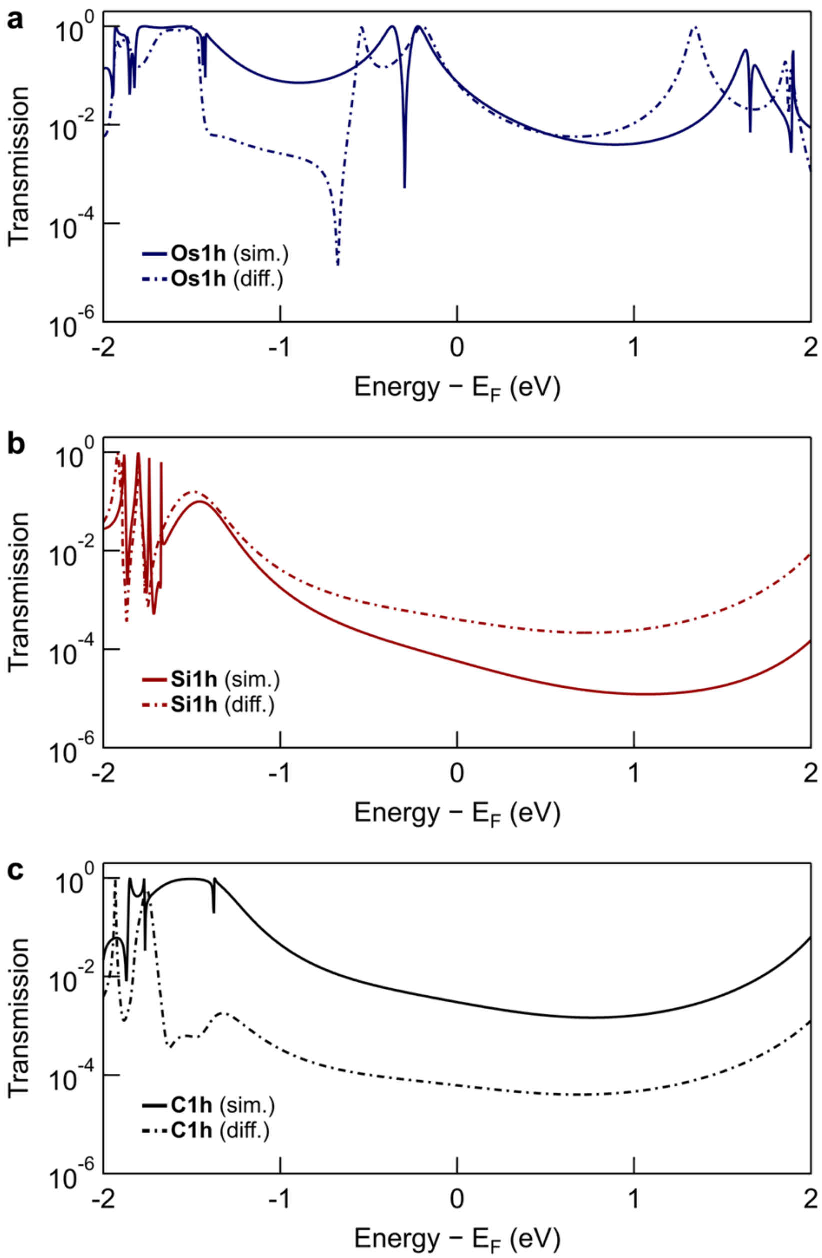

Figure S27. Transmission calculations for **(a) Os1h**, **(b) Si1h**, and **(b) C1h** junctions using the PBE functional, with electrodes connected at different −SMe groups. Here, the same molecular geometries, having similar or different dihedral angles, were used as for the above tunnel coupling calculations. The trends in calculated transmission at E_F using larger gold cluster electrodes follow those identified with Au_1 clusters. This highlights the impact of aryl-central atom-aryl geometries on transport through these wires and shows that the results of isolated calculations using specific geometries must be interpreted with care. We stress again here that these aryl groups are expected to freely rotate at room temperature in solution, such that the experimentally measured conductance for **Os-*n***, **Si-*n***, and **C-*n*** junctions corresponds to a time-averaged sample of all energetically accessible geometries.

8. NMR Spectra

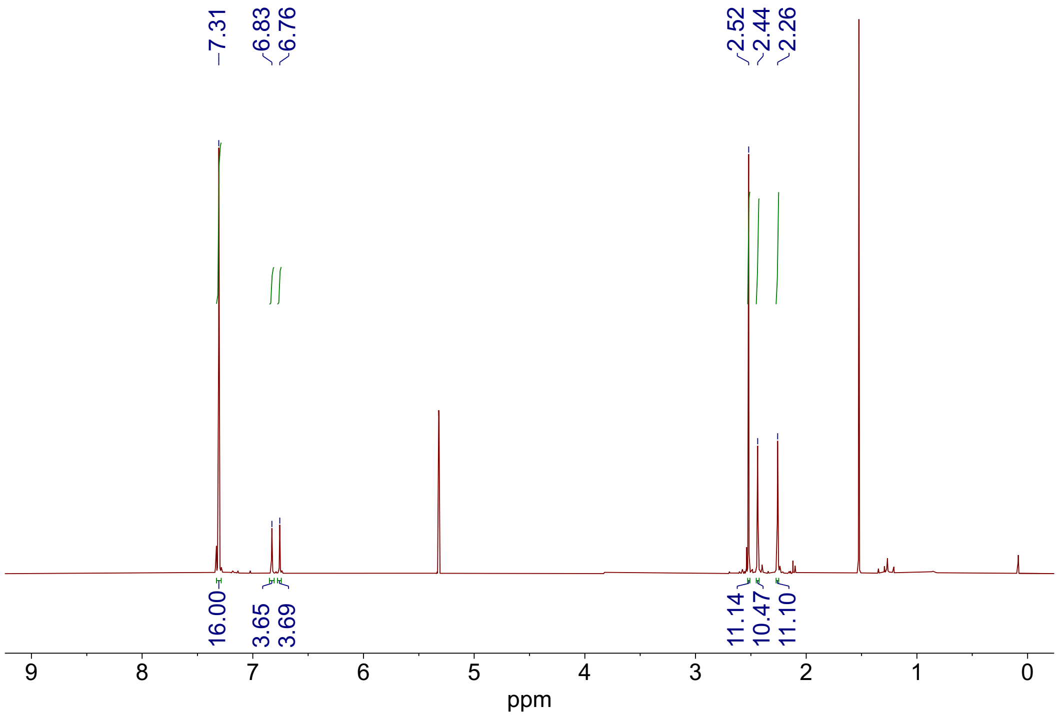

Figure S28. ^{1}H NMR (400 MHz) spectrum of **Os2** in CD_2Cl_2.

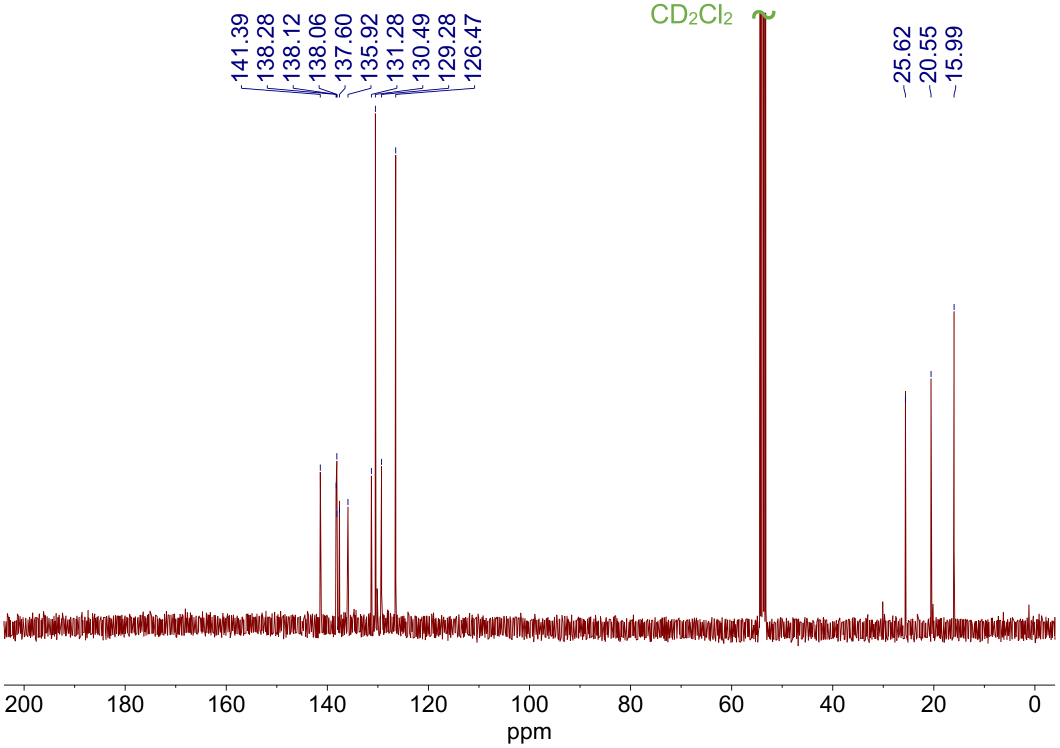

Figure S29. $^{13}C\{^{1}H\}$ NMR (100 MHz) spectrum of **Os2** in CD_2Cl_2.

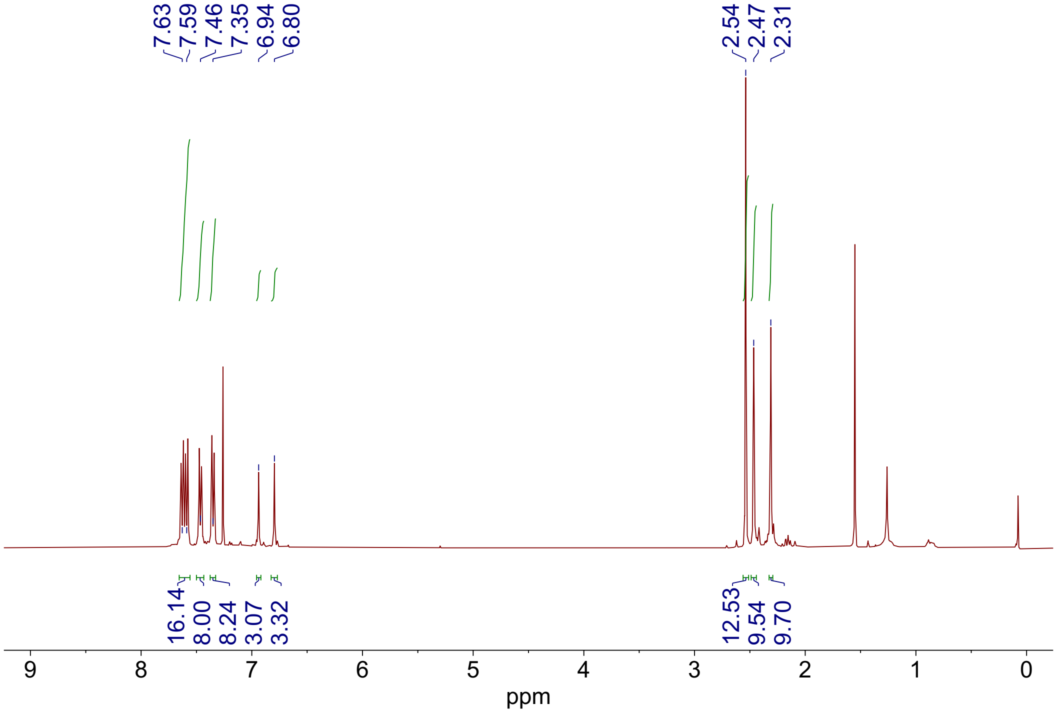

Figure S30. ^{1}H NMR (400 MHz) spectrum of **Os3** in $CDCl_3$.

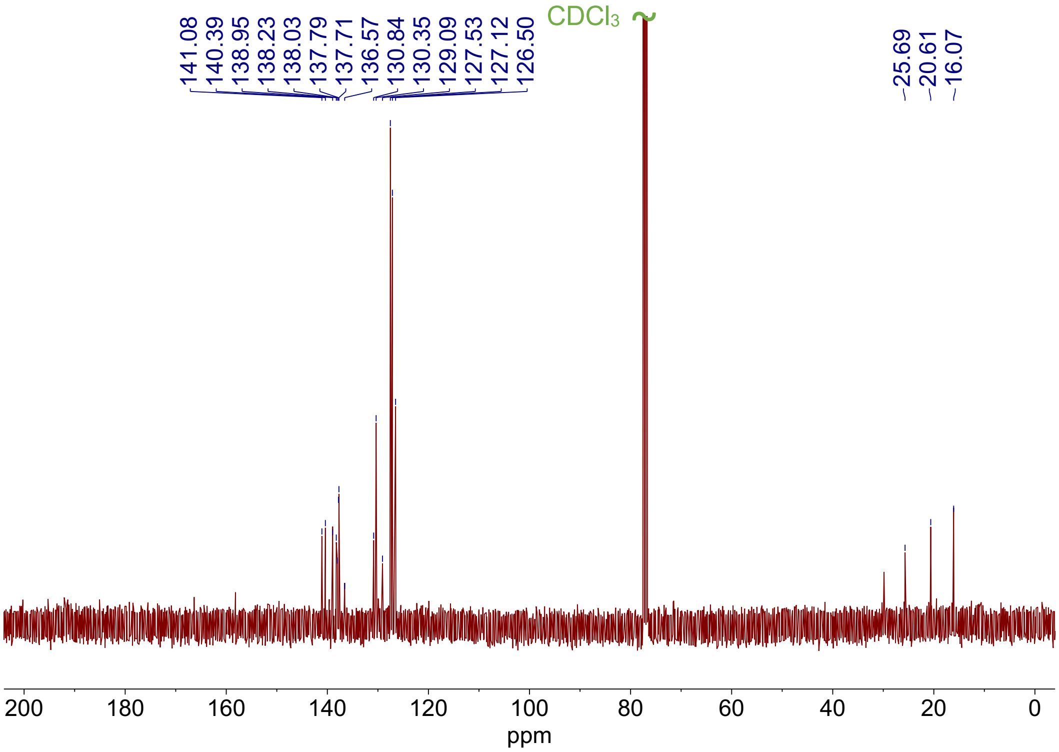

Figure S31. $^{13}C\{^1H\}$ NMR (101 MHz) spectrum of **Os3** in $CDCl_3$.

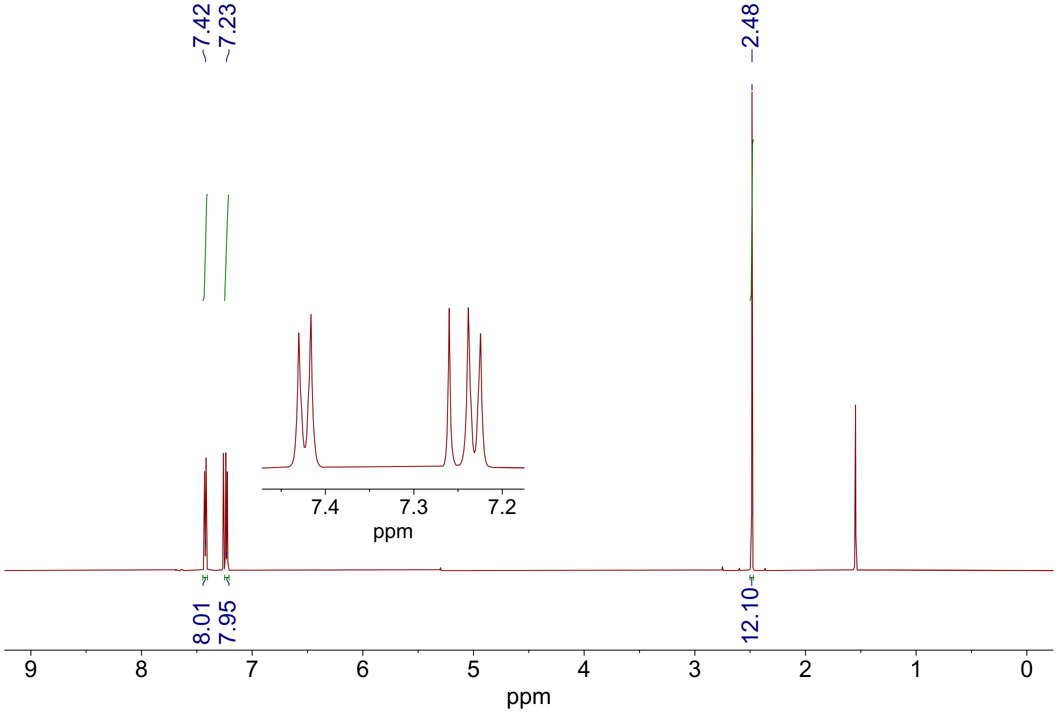

Figure S32. ^{1}H NMR (600 MHz) spectrum of **Si1** in CDCl$_3$.

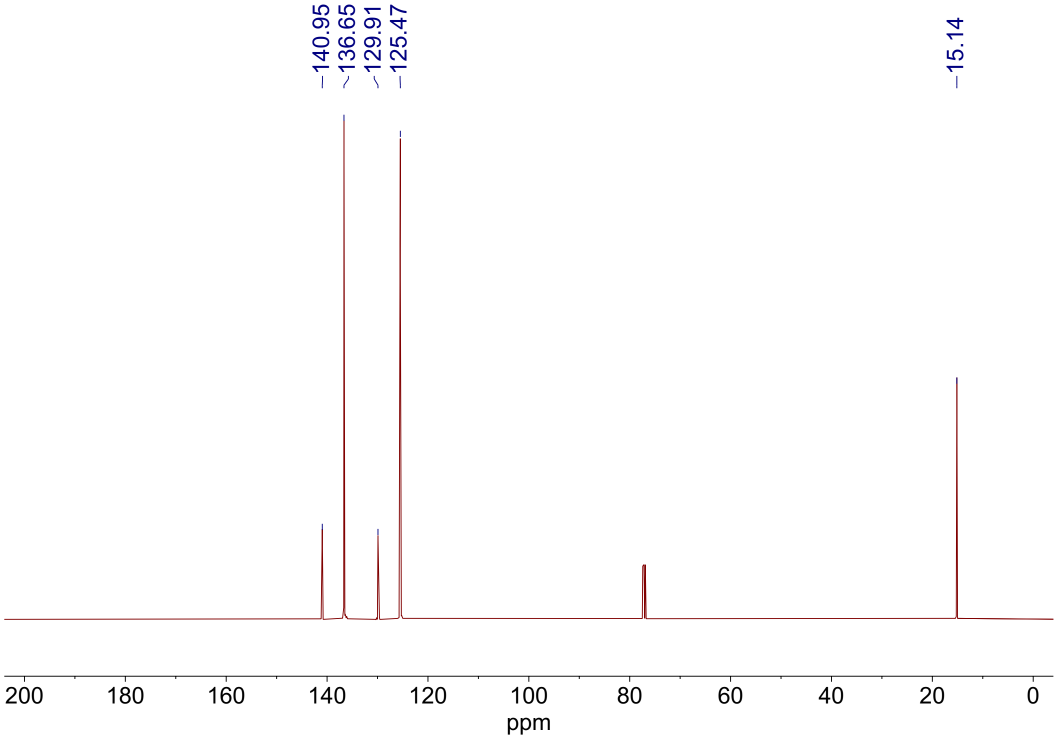

Figure S33. ^{13}C{^{1}H} NMR (126 MHz) spectrum of **Si1** in CDCl$_3$.

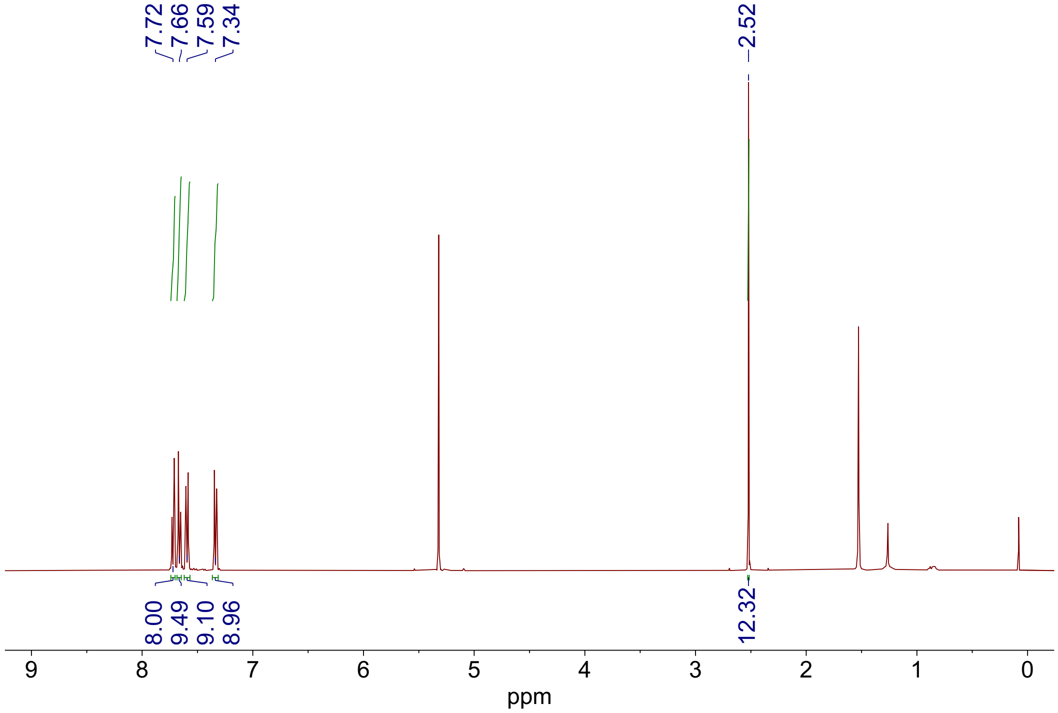

Figure S34. ^{1}H NMR (400 MHz) spectrum of **Si2** in CD_2Cl_2.

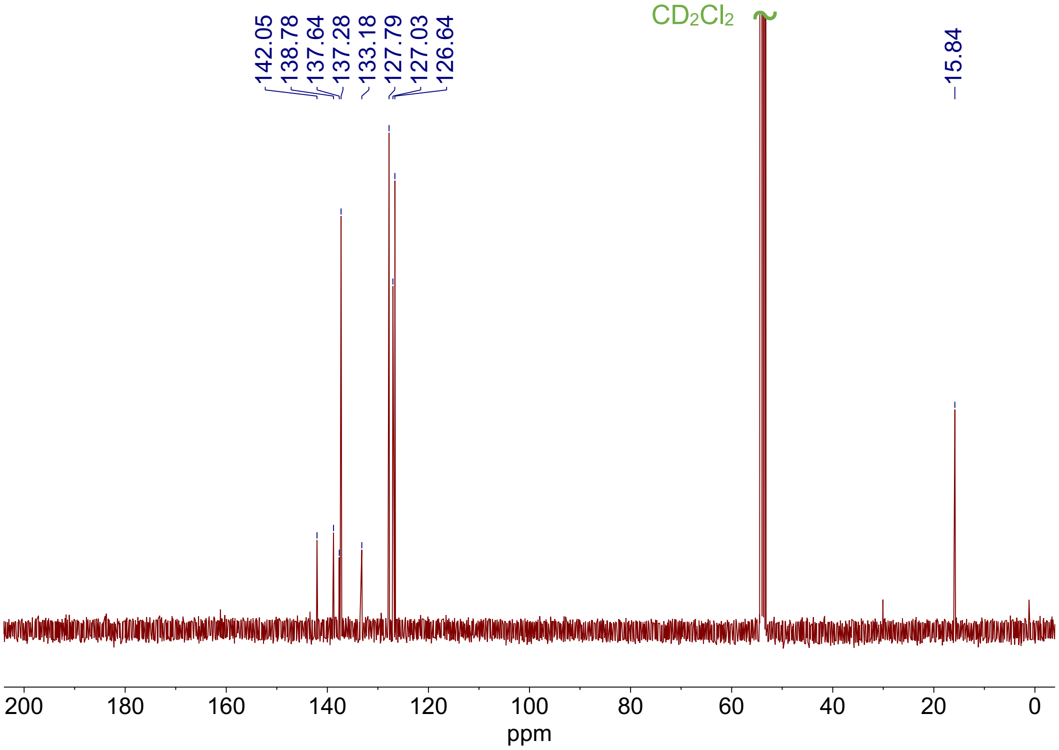

Figure S35. $^{13}C\{^{1}H\}$ NMR (101 MHz) spectrum of **Si2** in CD_2Cl_2.

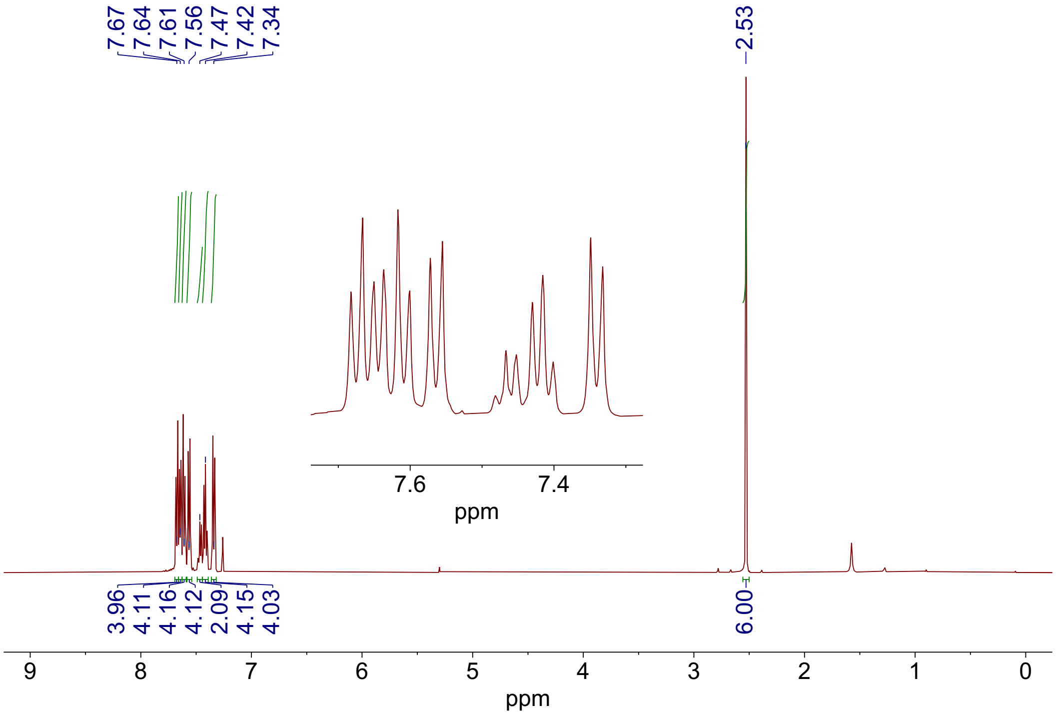

Figure S36. ^{1}H NMR (500 MHz) spectrum of **Si2 (−2PhSMe)** in CD_2Cl_2.

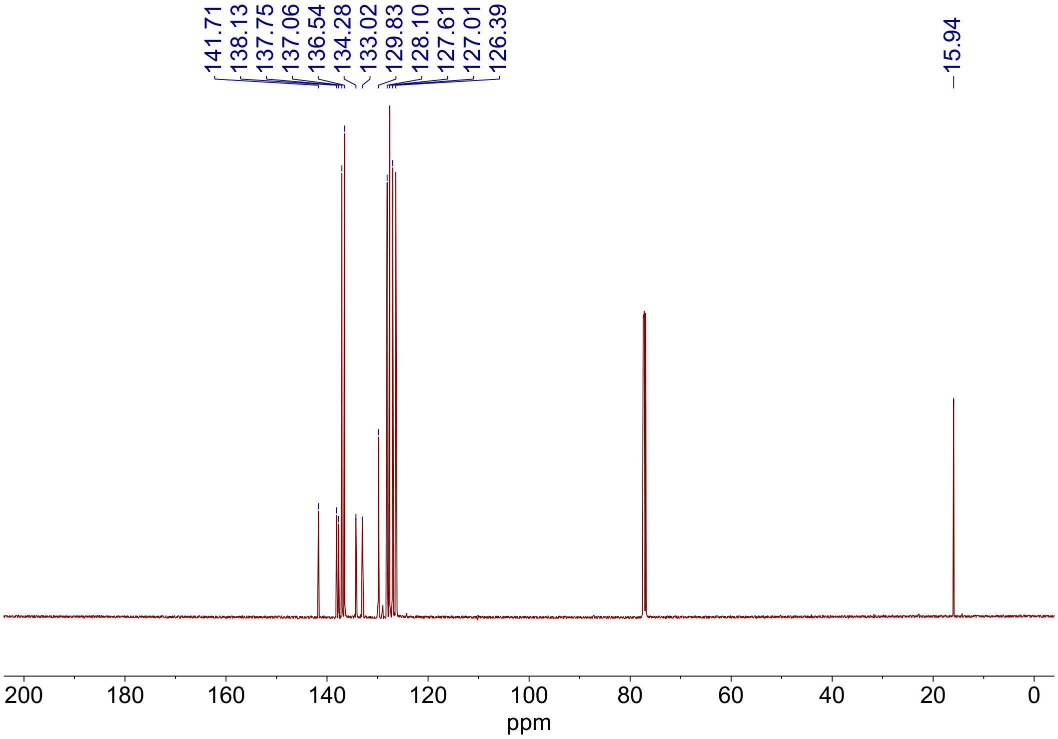

Figure S37. $^{13}C\{^1H\}$ NMR (126 MHz) spectrum of **Si2 (−2PhSMe)** in CD_2Cl_2.

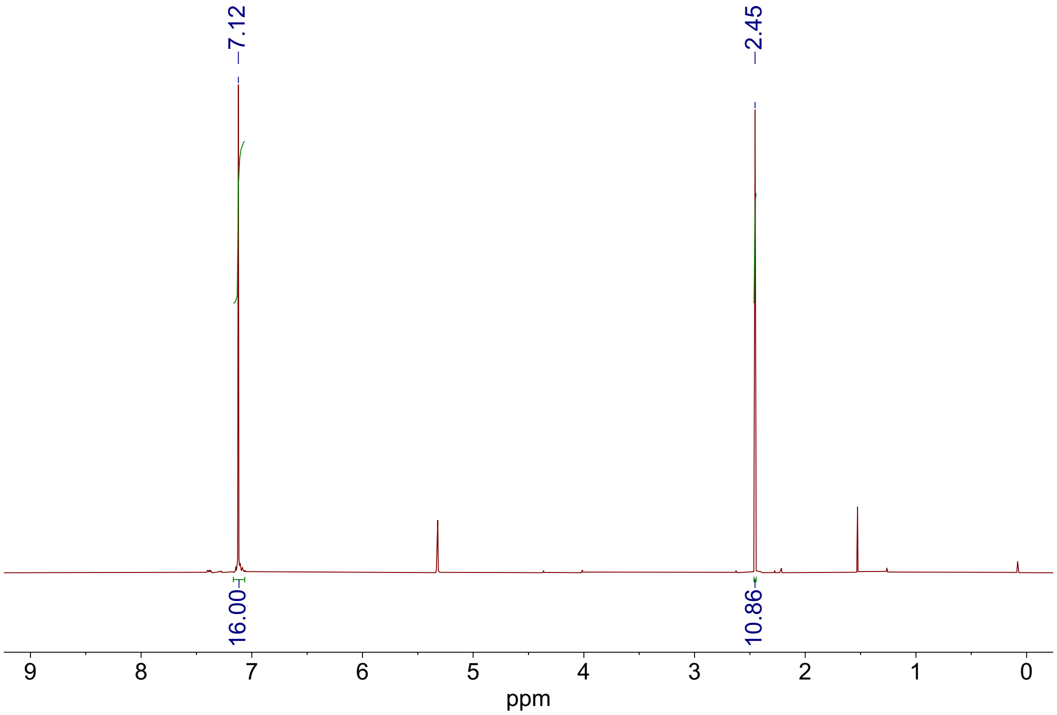

Figure S38. ^{1}H NMR (400 MHz) spectrum of **C1** in CD_2Cl_2.

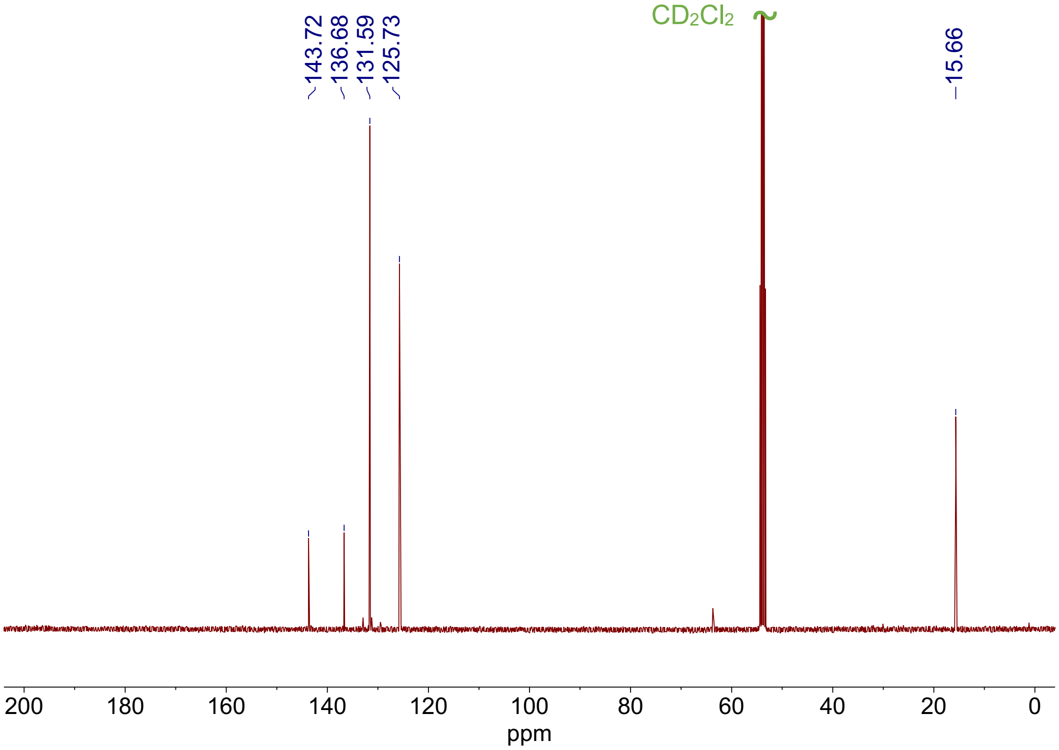

Figure S39. $^{13}C\{^{1}H\}$ NMR (150 MHz) spectrum of **C1** in CD_2Cl_2

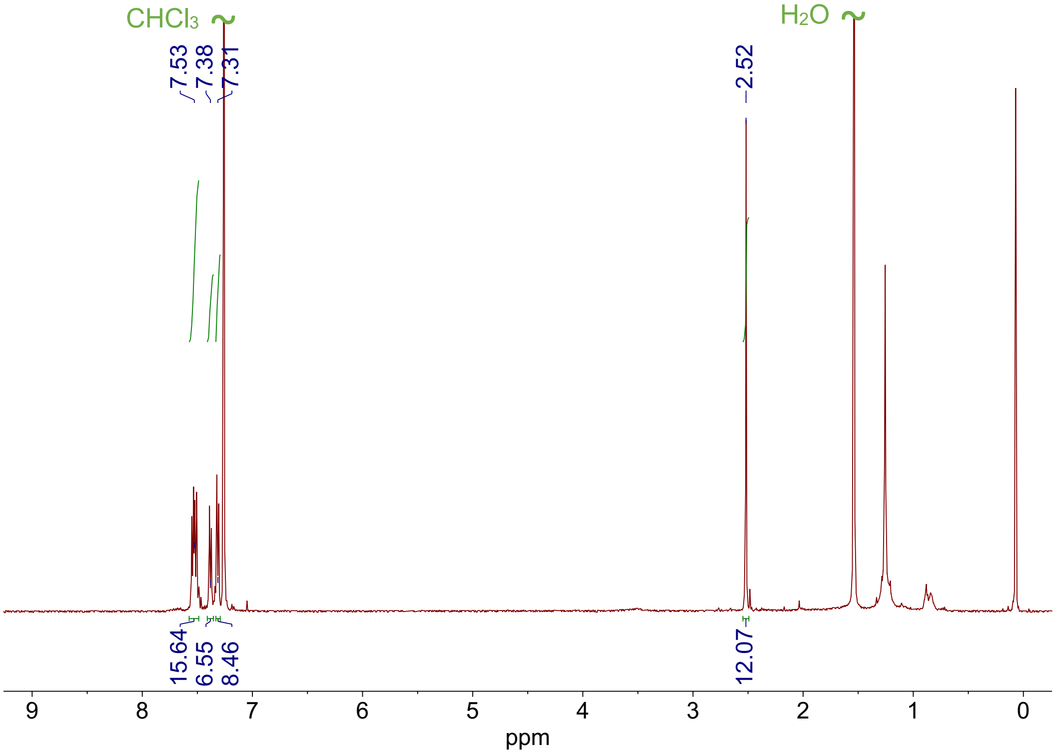

Figure S40. ^{1}H NMR (500 MHz) spectrum of **C2** in CDCl$_3$.

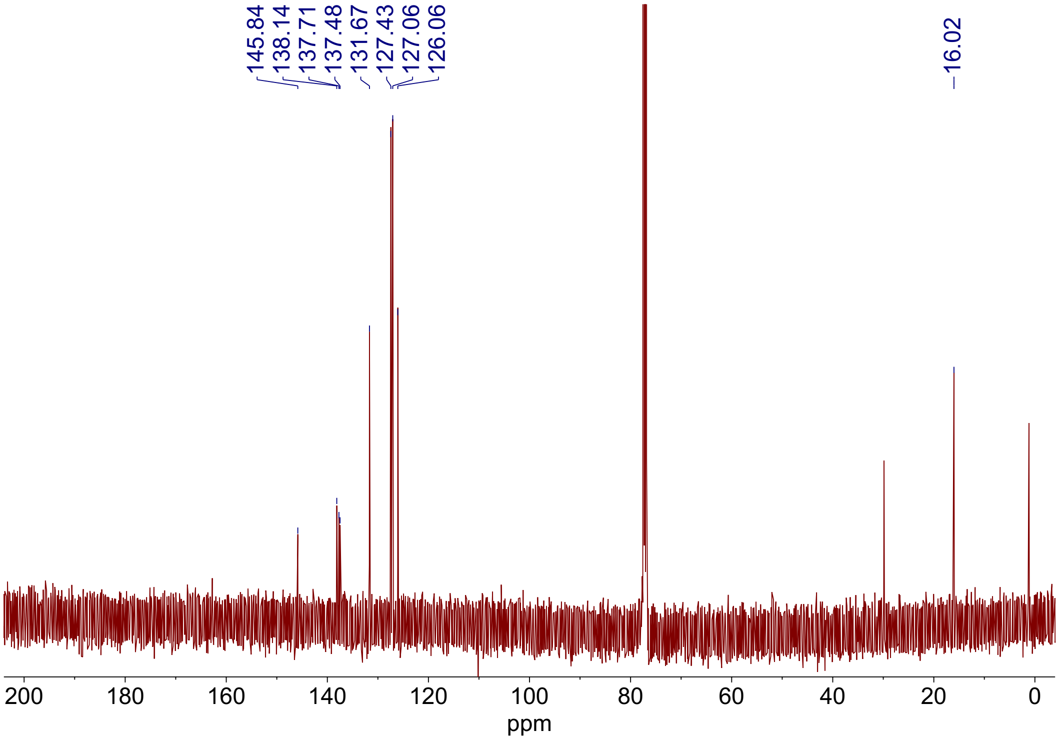

Figure S41. ^{13}C{^{1}H} NMR (126 MHz) spectrum of **C2** in CDCl$_3$.

9. References

(1) Williams, D. B. G.; Lawton, M. Drying of Organic Solvents: Quantitative Evaluation of the Efficiency of Several Desiccants. *J. Org. Chem.* **2010**, *75* (24), 8351–8354.
(2) Parr, J. M.; Olivar, C.; Saal, T.; Haiges, R.; Inkpen, M. S. Pushing Steric Limits in Osmium(Iv) Tetraaryl Complexes. *Dalton Trans.* **2022**, *51* (27), 10558–10570.
(3) Love, B. E.; Jones, E. G. The Use of Salicylaldehyde Phenylhydrazone as an Indicator for the Titration of Organometallic Reagents. *J. Org. Chem.* **1999**, *64* (10), 3755–3756.
(4) Zagami, L.; Saal, T.; Avedian, C.; Inkpen, M. S. Intervalence Charge Transfer in an Osmium(IV) Tetra(Ferrocenylaryl) Complex. *Inorg. Chem.* **2025**, *64* (5), 2312–2320.
(5) Olivar, C.; Parr, J. M.; Avedian, C.; Saal, T.; Zagami, L.; Haiges, R.; Sharma, M.; Inkpen, M. S. Osmium(IV) Tetraaryl Complexes Formed from Prefunctionalized Ligands. *Inorg. Chem.* **2025**, *64* (12), 6192–6204.
(6) Yang, J.; He, W.; Denman, K.; Jiang, Y. B.; Qin, Y. A Molecular Breakwater-like Tetrapod for Organic Solar Cells. *J. Mater. Chem. A* **2015**, *3* (5), 2108–2119.
(7) Starr, R. L.; Fu, T.; Doud, E. A.; Stone, I.; Roy, X.; Venkataraman, L. Gold–Carbon Contacts from Oxidative Addition of Aryl Iodides. *J. Am. Chem. Soc.* **2020**, *142* (15), 7128–7133.
(8) Lee, W.; Louie, S.; Evans, A. M.; Orchanian, N. M.; Stone, I. B.; Zhang, B.; Wei, Y.; Roy, X.; Nuckolls, C.; Venkataraman, L. Increased Molecular Conductance in Oligo[n]Phenylene Wires by Thermally Enhanced Dihedral Planarization. *Nano Lett.* **2022**, *22* (12), 4919–4924.
(9) Joseph, Y.; Peić, A.; Chen, X.; Michl, J.; Vossmeyer, T.; Yasuda, A. Vapor Sensitivity of Networked Gold Nanoparticle Chemiresistors: Importance of Flexibility and Resistivity of the Interlinkage. *J. Phys. Chem. C* **2007**, *111* (34), 12855–12859.
(10) Prana, J.; Kim, L.; Czyszczon-Burton, T.; Homann, G.; Chen, S.; Miao, Z.; Camarasa-Gomez, M.; Inkpen, M. Lewis-Acid Mediated Reactivity in Single-Molecule Junctions. *J. Am. Chem. Soc.* **2024**, *146* (48), 33265–33275.
(11) Fulmer, G. R.; Miller, A. J. M.; Sherden, N. H.; Gottlieb, H. E.; Nudelman, A.; Stoltz, B. M.; Bercaw, J. E.; Goldberg, K. I. NMR Chemical Shifts of Trace Impurities: Common Laboratory Solvents, Organics, and Gases in Deuterated Solvents Relevant to the Organometallic Chemist. *Organometallics* **2010**, *29* (9), 2176–2179.
(12) *CrysAlis*, Oxford Diffraction Ltd., Abingdon, England. **2006**.
(13) *SCALE3 ABSPACK* - An Oxford Diffraction Program (1.0.4,GUI:1.0.3); Oxford Diffraction Ltd.: Abingdon, England. **2005**.
(14) Sheldrick, G. M. Crystal Structure Refinement with SHELXL. *Acta Crystallogr. Sect. C* **2015**, *71* (1), 3–8.
(15) Sheldrick, G. M. *SHELXT* – Integrated Space-Group and Crystal-Structure Determination. *Acta Crystallogr. Sect. Found. Adv.* **2015**, *71* (1), 3–8.
(16) Dolomanov, O. V.; Bourhis, L. J.; Gildea, R. J.; Howard, J. A. K.; Puschmann, H. *OLEX2*: A Complete Structure Solution, Refinement and Analysis Program. *J. Appl. Crystallogr.* **2009**, *42* (2), 339–341.
(17) Kim, L.; Czyszczon-Burton, T. M.; Nguyen, K. M.; Stukey, S.; Lazar, S.; Prana, J.; Miao, Z.; Park, S.; Chen, S. F.; Inkpen, M. S. Low Vapor Pressure Solvents for Single-Molecule Junction Measurements. *Nano Lett.* **2024**, *24* (32), 9998–10005.

(18) Venkataraman, L.; Klare, J. E.; Tam, I. W.; Nuckolls, C.; Hybertsen, M. S.; Steigerwald, M. L. Single-Molecule Circuits with Well-Defined Molecular Conductance. *Nano Lett.* **2006**, *6* (3), 458–462.

(19) Inkpen, M. S.; Liu, Z.; Li, H.; Campos, L. M.; Neaton, J. B.; Venkataraman, L. Non-Chemisorbed Gold–Sulfur Binding Prevails in Self-Assembled Monolayers. *Nature Chem.* **2019**, *11*, 351–358.

(20) Miao, Z.; Quainoo, T.; Czyszczon-Burton, T. M.; Rotthowe, N.; Parr, J. M.; Liu, Z.; Inkpen, M. S. Charge Transport across Dynamic Covalent Chemical Bridges. *Nano Lett.* **2022**, *22* (20), 8331–8338.

(21) Wawrzyniak, M.; Martinek, J.; Susła, B.; Ilnicki, G. Correlation Histograms in Conductance Measurements of Nanowires Formed at Semiconductor Interfaces. *Acta Phys. Pol. A* **2009**, *115* (10), 384–386.

(22) Halbritter, A.; Makk, P.; Mackowiak, Sz.; Csonka, Sz.; Wawrzyniak, M.; Martinek, J. Regular Atomic Narrowing of Ni, Fe, and V Nanowires Resolved by Two-Dimensional Correlation Analysis. *Phys. Rev. Lett.* **2010**, *105* (26), 266805.

(23) Makk, P.; Tomaszewski, D.; Martinek, J.; Balogh, Z.; Csonka, S.; Wawrzyniak, M.; Frei, M.; Venkataraman, L.; Halbritter, A. Correlation Analysis of Atomic and Single-Molecule Junction Conductance. *ACS Nano* **2012**, *6* (4), 3411–3423.

(24) Epifanovsky, E.; Gilbert, A. T. B.; Feng, X.; Lee, J.; Mao, Y.; Mardirossian, N.; Pokhilko, P.; White, A. F.; Coons, M. P.; Dempwolff, A. L.; Gan, Z.; Hait, D.; Horn, P. R.; Jacobson, L. D.; Kaliman, I.; Kussmann, J.; Lange, A. W.; Lao, K. U.; Levine, D. S.; Liu, J.; McKenzie, S. C.; Morrison, A. F.; Nanda, K. D.; Plasser, F.; Rehn, D. R.; Vidal, M. L.; You, Z. Q.; Zhu, Y.; Alam, B.; Albrecht, B. J.; Aldossary, A.; Alguire, E.; Andersen, J. H.; Athavale, V.; Barton, D.; Begam, K.; Behn, A.; Bellonzi, N.; Bernard, Y. A.; Berquist, E. J.; Burton, H. G. A.; Carreras, A.; Carter-Fenk, K.; Chakraborty, R.; Chien, A. D.; Closser, K. D.; Cofer-Shabica, V.; Dasgupta, S.; De Wergifosse, M.; Deng, J.; Diedenhofen, M.; Do, H.; Ehlert, S.; Fang, P. T.; Fatehi, S.; Feng, Q.; Friedhoff, T.; Gayvert, J.; Ge, Q.; Gidofalvi, G.; Goldey, M.; Gomes, J.; González-Espinoza, C. E.; Gulania, S.; Gunina, A. O.; Hanson-Heine, M. W. D.; Harbach, P. H. P.; Hauser, A.; Herbst, M. F.; Hernández Vera, M.; Hodecker, M.; Holden, Z. C.; Houck, S.; Huang, X.; Hui, K.; Huynh, B. C.; Ivanov, M.; Jász, Á.; Ji, H.; Jiang, H.; Kaduk, B.; Kähler, S.; Khistyaev, K.; Kim, J.; Kis, G.; Klunzinger, P.; Koczor-Benda, Z.; Koh, J. H.; Kosenkov, D.; Koulias, L.; Kowalczyk, T.; Krauter, C. M.; Kue, K.; Kunitsa, A.; Kus, T.; Ladjánszki, I.; Landau, A.; Lawler, K. V.; Lefrancois, D.; Lehtola, S.; Li, R. R.; Li, Y. P.; Liang, J.; Liebenthal, M.; Lin, H. H.; Lin, Y. S.; Liu, F.; Liu, K. Y.; Loipersberger, M.; Luenser, A.; Manjanath, A.; Manohar, P.; Mansoor, E.; Manzer, S. F.; Mao, S. P.; Marenich, A. V.; Markovich, T.; Mason, S.; Maurer, S. A.; McLaughlin, P. F.; Menger, M. F. S. J.; Mewes, J. M.; Mewes, S. A.; Morgante, P.; Mullinax, J. W.; Oosterbaan, K. J.; Paran, G.; Paul, A. C.; Paul, S. K.; Pavošević, F.; Pei, Z.; Prager, S.; Proynov, E. I.; Rák, Á.; Ramos-Cordoba, E.; Rana, B.; Rask, A. E.; Rettig, A.; Richard, R. M.; Rob, F.; Rossomme, E.; Scheele, T.; Scheurer, M.; Schneider, M.; Sergueev, N.; Sharada, S. M.; Skomorowski, W.; Small, D. W.; Stein, C. J.; Su, Y. C.; Sundstrom, E. J.; Tao, Z.; Thirman, J.; Tornai, G. J.; Tsuchimochi, T.; Tubman, N. M.; Veccham, S. P.; Vydrov, O.; Wenzel, J.; Witte, J.; Yamada, A.; Yao, K.; Yeganeh, S.; Yost, S. R.; Zech, A.; Zhang, I. Y.; Zhang, X.; Zhang, Y.; Zuev, D.; Aspuru-Guzik, A.; Bell, A. T.; Besley, N. A.; Bravaya, K. B.; Brooks, B. R.; Casanova, D.; Chai, J. D.; Coriani, S.; Cramer, C. J.; Cserey, G.; Deprince, A. E.; Distasio, R. A.; Dreuw, A.; Dunietz, B. D.;

Furlani, T. R.; Goddard, W. A.; Hammes-Schiffer, S.; Head-Gordon, T.; Hehre, W. J.; Hsu, C. P.; Jagau, T. C.; Jung, Y.; Klamt, A.; Kong, J.; Lambrecht, D. S.; Liang, W.; Mayhall, N. J.; McCurdy, C. W.; Neaton, J. B.; Ochsenfeld, C.; Parkhill, J. A.; Peverati, R.; Rassolov, V. A.; Shao, Y.; Slipchenko, L. V.; Stauch, T.; Steele, R. P.; Subotnik, J. E.; Thom, A. J. W.; Tkatchenko, A.; Truhlar, D. G.; Van Voorhis, T.; Wesolowski, T. A.; Whaley, K. B.; Woodcock, H. L.; Zimmerman, P. M.; Faraji, S.; Gill, P. M. W.; Head-Gordon, M.; Herbert, J. M.; Krylov, A. I. Software for the Frontiers of Quantum Chemistry: An Overview of Developments in the Q-Chem 5 Package. *J. Chem. Phys.* **2021**, *155*, 084801.

(25) Robbins, A.; Jeffrey, G. A.; Chesick, J. P.; Donohue, J.; Cotton, F. A.; Frenz, B. A.; Murillo, C. A. A Refinement of the Crystal Structure of Tetraphenylmethane: Three Independent Redeterminations. *Acta Crystallogr. B* **1975**, *31* (10), 2395–2399.

(26) Gruhnert, V.; Kirfel, A.; Will, G.; Wallrafen, F.; Recker, K. The Crystal Structure and Electron Density of Tetraphenyl-Silicon, $(C_6H_5)_4Si$. *Z. Krist.* **1983**, *163*, 53–60.

(27) Perdew, J. P.; Burke, K.; Ernzerhof, M. Generalized Gradient Approximation Made Simple. *Phys. Rev. Lett.* **1996**, *77* (18), 3865–3868.

(28) Woitellier, S.; Launay, J. P.; Joachim. The Possibility of Molecular Switching: Theoretical Study of $[(NH_3)_5Ru\text{-}4,4'\text{-}Bipy\text{-}Ru(NH_3)_5]^{5+}$. *Chem. Phys.* **1989**, *131*, 481–488.

(29) Venkataraman, L.; Klare, J. E.; Nuckolls, C.; Hybertsen, M. S.; Steigerwald, M. L. Dependence of Single-Molecule Junction Conductance on Molecular Conformation. *Nature* **2006**, *442* (7105), 904–907.

(30) Blum, V.; Gehrke, R.; Hanke, F.; Havu, P.; Havu, V.; Ren, X.; Reuter, K.; Scheffler, M. Ab Initio Molecular Simulations with Numeric Atom-Centered Orbitals. *Comput. Phys. Commun.* **2009**, *180* (11), 2175–2196.

(31) Lenthe, E. V.; Baerends, E. J.; Snijders, J. G. Relativistic Regular Two-Component Hamiltonians. *J. Chem. Phys.* **1993**, *99* (6), 4597–4610.

(32) Camarasa-Gómez, M.; Hernangómez-Pérez, D.; Evers, F. Spin–Orbit Torque in Single-Molecule Junctions from Ab Initio. *J. Phys. Chem. Lett.* **2024**, *15* (21), 5747–5753.

(33) Arnold, A.; Weigend, F.; Evers, F. Quantum Chemistry Calculations for Molecules Coupled to Reservoirs: Formalism, Implementation, and Application to Benzenedithiol. *J. Chem. Phys.* **2007**, *126* (17), 174101.

(34) Bagrets, A. Spin-Polarized Electron Transport Across Metal–Organic Molecules: A Density Functional Theory Approach. *J. Chem. Theory Comput.* **2013**, *9* (6), 2801–2815.

(35) Lau, M.-K.; Zhang, Q.-F.; Chim, J. L. C.; Wong, W.-T.; Leung, W.-H. Direct Functionalisation of σ-Aryl Ligands: Preparation of Homoleptic Functionalised Aryls of Osmium(Iv). *Chem. Commun.* **2001**, *79* (16), 1478–1479.

(36) Akiyama, T.; Suzuki, T.; Mori, K. Enantioselective Aza-Darzens Reaction Catalyzed by A Chiral Phosphoric Acid. *Org. Lett.* **2009**, *11* (11), 2445–2447.

(37) Doud, E. A.; Inkpen, M. S.; Lovat, G.; Montes, E.; Paley, D. W.; Steigerwald, M. L.; Vázquez, H.; Venkataraman, L.; Roy, X. In Situ Formation of N-Heterocyclic Carbene-Bound Single-Molecule Junctions. *J. Am. Chem. Soc.* **2018**, *140* (28), 8944–8949.

(38) Lau, M.-K. Transition Metal Complexes with Functionalized Aryl Ligands, Hong Kong University of Science and Technology, 1999.

(39) Liu, X.-M.; He, C.; Xu, J.-W. Synthesis and Optical Properties of Tetraphenylmethane-Based Tetrahedral Fluorescent Compounds and Their Water-Soluble PEG-Linked Polymers. *Tetrahedron Lett.* **2004**, *45* (8), 1593–1597.

(40) Liu, X.-M.; He, C.; Huang, J.; Xu, J. Highly Efficient Blue-Light-Emitting Glass-Forming Molecules Based on Tetraarylmethane/Silane and Fluorene: Synthesis and Thermal, Optical, and Electrochemical Properties. *Chem. Mater.* **2005**, *17* (2), 434–441.

(41) Ghasemi, S.; Ornago, L.; Liasi, Z.; Johansen, M. B.; Von Buchwald, T. J.; Hillers-Bendtsen, A. E.; Van Der Poel, S.; Hölzel, H.; Wang, Z.; Amombo Noa, F. M.; Öhrström, L.; Mikkelsen, K. V.; Van Der Zant, H. S. J.; Lara-Avila, S.; Moth-Poulsen, K. Exploring the Impact of Select Anchor Groups for Norbornadiene/Quadricyclane Single-Molecule Switches. *J. Mater. Chem. C* **2023**, *11* (44), 15412–15418.

(42) Prana, J.; Zagami, L.; Yan, K.; Hernangómez-Pérez, D.; Camarasa-Gómez, M.; Inkpen, M. S. Forming Chemisorbed Single-Molecule Junctions through Loss of Stable Carbocations. *Nano Lett.* **2025**, *25* (26), 10427–10434.

(43) Rashid, U.; Bro-Jørgensen, W.; Harilal, K.; Sreelakshmi, P.; Mondal, R. R.; Chittari Pisharam, V.; Parida, K. N.; Geetharani, K.; Hamill, J. M.; Kaliginedi, V. Chemistry of the Au–Thiol Interface through the Lens of Single-Molecule Flicker Noise Measurements. *J. Am. Chem. Soc.* **2024**, *146* (13), 9063–9073.

(44) Prindle, C. R.; Shi, W.; Li, L.; Jensen, J. D.; Laursen, B. W.; Steigerwald, M. L.; Nuckolls, C.; Venkataraman, L. Effective Gating in Single-Molecule Junctions through Fano Resonances. *J. Am. Chem. Soc.* **2024**, *146* (3646–3650).

(45) Cheng, Z. L.; Skouta, R.; Vazquez, H.; Widawsky, J. R.; Schneebeli, S.; Chen, W.; Hybertsen, M. S.; Breslow, R.; Venkataraman, L. In Situ Formation of Highly Conducting Covalent Au-C Contacts for Single-Molecule Junctions. *Nature Nanotechnol.* **2011**, *6* (6), 353–357.

(46) Li, Y.; Zhao, C.; Wang, R.; Tang, A.; Hong, W.; Qu, D.; Tian, H.; Li, H. In Situ Monitoring of Transmetallation in Electric Potential-Promoted Oxidative Coupling in a Single-Molecule Junction. *CCS Chem.* **2022**, *5*, 191–199.

(47) Kotiuga, M.; Darancet, P.; Arroyo, C. R.; Venkataraman, L.; Neaton, J. B. Adsorption-Induced Solvent-Based Electrostatic Gating of Charge Transport through Molecular Junctions. *Nano Lett.* **2015**, *15* (7), 4498–4503.

(48) Fatemi, V.; Kamenetska, M.; Neaton, J. B.; Venkataraman, L. Environmental Control of Single-Molecule Junction Transport. *Nano Lett.* **2011**, *11* (5), 1988–1992.

(49) Dalmieda, J.; Shi, W.; Li, L.; Venkataraman, L. Solvent-Mediated Modulation of the Au–S Bond in Dithiol Molecular Junctions. *Nano Lett.* **2024**, *24* (2), 703–707.

(50) Zang, Y.; Zou, Q.; Fu, T.; Ng, F.; Fowler, B.; Yang, J.; Li, H.; Steigerwald, M. L.; Nuckolls, C.; Venkataraman, L. Directing Isomerization Reactions of Cumulenes with Electric Fields. *Nature Commun.* **2019**, *10* (1), 4482.

(51) Meisner, J. S.; Ahn, S.; Aradhya, S. V.; Krikorian, M.; Parameswaran, R.; Steigerwald, M.; Venkataraman, L.; Nuckolls, C. Importance of Direct Metal−π Coupling in Electronic Transport Through Conjugated Single-Molecule Junctions. *J. Am. Chem. Soc.* **2012**, *134* (50), 20440–20445.

(52) Quek, S. Y.; Kamenetska, M.; Steigerwald, M. L.; Choi, H. J.; Louie, S. G.; Hybertsen, M. S.; Neaton, J. B.; Venkataraman, L. Mechanically Controlled Binary Conductance Switching of a Single-Molecule Junction. *Nature Nanotechnol.* **2009**, *4* (4), 230–234.

(53) Schneebeli, S. T.; Kamenetska, M.; Cheng, Z.; Skouta, R.; Friesner, R. A.; Venkataraman, L.; Breslow, R. Single-Molecule Conductance through Multiple π-π-Stacked Benzene Rings Determined with Direct Electrode-to-Benzene Ring Connections. *J. Am. Chem. Soc.* **2011**, *133* (7), 2136–2139.

(54) Chen, H.; Brasiliense, V.; Mo, J.; Zhang, L.; Jiao, Y.; Chen, Z.; Jones, L. O.; He, G.; Guo, Q.-H.; Chen, X.-Y.; Song, B.; Schatz, G. C.; Stoddart, J. F. Single-Molecule Charge Transport through Positively Charged Electrostatic Anchors. *J. Am. Chem. Soc.* **2021**, *143* (7), 2886–2895.
(55) Wu, S.; Gonzalez, M. T.; Huber, R.; Grunder, S.; Mayor, M.; Schonenberger, C.; Calame, M. Molecular Junctions Based on Aromatic Coupling. *Nature Nanotechnol.* **2008**, *3* (9), 569–574.
(56) Bard, A. J.; Faulkner, L. Y. *Electrochemical Methods*; Wiley, 2004.
(57) Venkataraman, L.; Park, Y. S.; Whalley, A. C.; Nuckolls, C.; Hybertsen, M. S.; Steigerwald, M. L. Electronics and Chemistry: Varying Single-Molecule Junction Conductance Using Chemical Substituents. *Nano Lett.* **2007**, *7* (2), 502–506.
(58) Gray, H. B. Molecular Orbital Theory for Transition Metal Complexes. *J. Chem. Educ.* **1964**, *41* (1), 2.